



UNIVERSITAT POLITÈCNICA  
DE CATALUNYA  
BARCELONATECH

# *TiO<sub>2</sub>-based heterostructure photocatalysts for enhanced hydrogen production*

**Congcong Xing**

**ADVERTIMENT** La consulta d'aquesta tesi queda condicionada a l'acceptació de les següents condicions d'ús: La difusió d'aquesta tesi per mitjà del repositori institucional UPCommons (<http://upcommons.upc.edu/tesis>) i el repositori cooperatiu TDX (<http://www.tdx.cat/>) ha estat autoritzada pels titulars dels drets de propietat intel·lectual **únicament per a usos privats** emmarcats en activitats d'investigació i docència. No s'autoritza la seva reproducció amb finalitats de lucre ni la seva difusió i posada a disposició des d'un lloc aliè al servei UPCommons o TDX. No s'autoritza la presentació del seu contingut en una finestra o marc aliè a UPCommons (*framing*). Aquesta reserva de drets afecta tant al resum de presentació de la tesi com als seus continguts. En la utilització o cita de parts de la tesi és obligat indicar el nom de la persona autora.

**ADVERTENCIA** La consulta de esta tesis queda condicionada a la aceptación de las siguientes condiciones de uso: La difusión de esta tesis por medio del repositorio institucional UPCommons (<http://upcommons.upc.edu/tesis>) y el repositorio cooperativo TDR (<http://www.tdx.cat/?locale-attribute=es>) ha sido autorizada por los titulares de los derechos de propiedad intelectual **únicamente para usos privados enmarcados** en actividades de investigación y docencia. No se autoriza su reproducción con finalidades de lucro ni su difusión y puesta a disposición desde un sitio ajeno al servicio UPCommons No se autoriza la presentación de su contenido en una ventana o marco ajeno a UPCommons (*framing*). Esta reserva de derechos afecta tanto al resumen de presentación de la tesis como a sus contenidos. En la utilización o cita de partes de la tesis es obligado indicar el nombre de la persona autora.

**WARNING** On having consulted this thesis you're accepting the following use conditions: Spreading this thesis by the institutional repository UPCommons (<http://upcommons.upc.edu/tesis>) and the cooperative repository TDX (<http://www.tdx.cat/?locale-attribute=en>) has been authorized by the titular of the intellectual property rights **only for private uses** placed in investigation and teaching activities. Reproduction with lucrative aims is not authorized neither its spreading nor availability from a site foreign to the UPCommons service. Introducing its content in a window or frame foreign to the UPCommons service is not authorized (*framing*). These rights affect to the presentation summary of the thesis as well as to its contents. In the using or citation of parts of the thesis it's obliged to indicate the name of the author.

# TiO<sub>2</sub>-based heterostructure photocatalysts for enhanced hydrogen production

This dissertation is submitted for the degree of *Doctor of Chemistry* by

Congcong Xing

Directed by

Prof. Dr. Andreu Cabot

Prof. Dr. Jordi Llorca



Universitat Politècnica de Catalunya

PhD Program in Chemical Process Engineering

June 2021



## Preface

The four chapters of this PhD thesis cover the work performed by the PhD candidate Congcong Xing at the Universitat Politècnica de Catalunya (UPC) and the Institut de Recerca en Energia de Catalunya (IREC) in the period 2017-2021, supported by China Scholarship Council (No. 201707040052). The thesis focuses on the design and development of TiO<sub>2</sub>-based heterostructure photocatalysts for hydrogen production from ethanol dehydrogenation.

In the first chapter, a fundamental introduction to the basic concepts of the photocatalysis field, its state of the art, the remaining challenges and the thesis objectives are presented. Chapters two to five provide the experimental work. In chapter two, the synthesis and performance of porous NiTiO<sub>3</sub>/TiO<sub>2</sub> nanostructures are presented. The presence of NiTiO<sub>3</sub>, with a lower band gap energy, provides a higher light absorption. Meanwhile the porous nanostructures improve the surface area. In chapter three, the synthesis of CoTiO<sub>3</sub>/TiO<sub>2</sub> heterostructures is presented. These heterostructures have a significant influence on visible light absorption and thus on the hydrogen production. UV-vis spectroscopy and UPS analysis showed the alignment of the energy levels pointed at a Z-scheme mechanism, with the CBM of CoTiO<sub>3</sub> below the H<sub>2</sub>/H<sup>+</sup> energy level. In chapter four, Cu<sub>2</sub>O/TiO<sub>2</sub> heterostructures are synthesized and characterized. These materials are also tested for the photocatalytic dehydrogenation of ethanol in water:ethanol vapor mixture. In these materials we discern the influence of temperature and photogenerated electron-hole pairs in the generation of hydrogen using visible light irradiation.

## Acknowledgements

First and foremost, I am grateful for the scholarship provided by China Scholarship Council (CSC), which provided a four-year scholarship and ensured my livelihood during my four-years of doctorate.

I would like to thank my thesis advisors, Prof. Andreu Cabot (Institut de Recerca en Energia de Catalunya, IREC) and Prof. Jordi Llorca (Universitat Politècnica de Catalunya, UPC), for creating an extremely superior scientific research environment, for providing me with the best platform and resources, and for allowing me to devote myself to scientific research during my PhD study.

Many thanks to NEMEN members in UPC with whom I shared joy and successes. Thanks to all the members of the research groups for welcoming me and making me feel at home. A special thanks to Yufen, Ilaria, Xènia, Shiva, Alejandro, Ander and Serafin for their support and great contribution during my stay at UPC. Special thanks to the laboratory technicians and postdocs, Isa, Xavier and Lluís, for their constant and indispensable help.

I would like to thank the IREC-FN members Yu Zhang, Junfeng Liu, Yong Zhuo, Xiang Wang, Junshan Li and Ruifeng Du for their help during the experiment at IREC. Their assistance allowed me to successfully complete many experiments. Yu Zhang and Xiang Wang gave me countless guidance and concern in schlenk line system, Junfeng Liu in the same hood, Yong Zhuo and Ruifeng Du in the mechanisms of photocatalysis. Without the precepts and deeds of a few helps, I will certainly not be able to successfully complete my Ph.D. studies. I also thank Mengyao Li and Xiaoting Yu, we talk about some interesting things to eliminate exhaustion at work. And also, thanks to Ke Xiao, Dawei Yang, Chaoqi Zhang, Heren Chao, Linlin Yang, Pablo Guardia, Binfei Nan, Xuan Lu and Juses. I am so happy work with you.

I would like to thank the lunch group, Alberto, Yu Zhang, Xiang Wang and levgenii, share some new things in life and new technology to enrich the lunch time.

I would like to thank Maria Chiara Spadaro, Ting Zhang, Xu Han and Jordi Arbiol to provide support in HRTEM measurement.

Thanks to all the friends I met during my Ph.D. It was their appearance that made my PhD life more colorful and made me have wonderful memories of the past few years in the days to come. Thanks to Xiangwei Yu and Liang Jing, for being so understanding and for your continued encouragement, I am happy to have you as my friends. Thanks to Chaoren and Liang Jing for the original cover and the patience and for the interesting talks. I thank all the Chinese friends who have supported me regardless the distance.

Finally and most importantly, I would also like to thank all my families in China. Thanks to my family, for being always and in any case present, a reassuring certainty in my life. I am sorry that I cannot accompany you quit often specially during my Ph.D., and you often worried about me. Thank you for your company, trust, understanding and support all the time. In addition, my little sister and brother have always supported my studies in particular.

Thanks again to all those who believe in me. Your encouragement to me gave me the motivation to persevere; thanks to all those who doubt me, your disdain for me is a great spur to me.

I would also like to thank all the teachers and friends who reviewed this paper. Thank you for your time.

## List of publications

My PhD research work has been disseminated in three manuscripts, which have been published in first quartile peer-reviewed journals. A full copy of each of the publications can be found in the Annex part. The following is the list of publications included in this thesis:

1. **Xing, C.**; Liu, Y.; Zhang, Y.; Liu, J.; Zhang, T.; Tang, P.; Arbiol, J.; Soler, L.; Sivula, K.; Guijarro, N.; Wang, X.; Li, J.; Du, R.; Zuo, Y.; Cabot, A.; Llorca, J. Porous NiTiO<sub>3</sub>/TiO<sub>2</sub> Nanostructures for Photocatalytic Hydrogen Evolution. *J. Mater. Chem. A* **2019**, 7 (28), 17053–17059.
2. **Xing, C.**; Liu, Y.; Zhang, Y.; Wang, X.; Guardia, P.; Yao, L.; Han, X.; Zhang, T.; Arbiol, J.; Soler, L.; Chen, Y.; Sivula, K.; Guijarro, N.; Cabot, A.; Llorca, J. A Direct Z-Scheme for the Photocatalytic Hydrogen Production from a Water Ethanol Mixture on CoTiO<sub>3</sub>/TiO<sub>2</sub> Heterostructures. *ACS Appl. Mater. Interfaces* **2021**, 13 (1), 449–457.
3. **Xing, C.**; Zhang, Y.; Liu, Y.; Wang, X.; Li, J.; Martínez-Alanis, P. R.; Spadaro, M. C.; Guardia, P.; Arbiol, J.; Llorca, J.; Cabot, A. Photodehydrogenation of ethanol over Cu<sub>2</sub>O/TiO<sub>2</sub> heterostructures. *Nanomaterials*. **2021**, 11, 1399.

## Authors' contributions

The work presented in this thesis was performed at the Universitat Politècnica de Catalunya (UPC) and the Catalonia Institute for Energy Research (IREC). The PhD student, **Congcong Xing**, has primary contribution in all experimental work, data processing and manuscript writing for each of the publications included in this thesis. The contributions of co-authors for each paper are specifically mentioned in the paragraphs below. The impact factor in 2019 of the journals where the manuscripts were published is provided. All of the publications belong to the 1st quartile according to the Science Citation Index. None of these papers has been previously presented in any other PhD thesis.

In all the publications, Andreu Cabot and Jordi Llorca conceived and guided the projects, participated in the experiment design and manuscript writing.

### Chapter 2

**Xing, C.**; Liu, Y.; Zhang, Y.; Liu, J.; Zhang, T.; Tang, P.; Arbiol, J.; Soler, L.; Sivula, K.; Guijarro, N.; Wang, X.; Li, J.; Du, R.; Zuo, Y.; Cabot, A.; Llorca, J. Porous NiTiO<sub>3</sub>/TiO<sub>2</sub> Nanostructures for Photocatalytic Hydrogen Evolution. *J. Mater. Chem. A* **2019**, *7* (28), 17053–17059.

Impact factor 2019: **11.3**

In this work, Xing, C.; Liu, Y.; Zhang, Y.; Cabot, A. and Llorca, J. conceived and prepared the manuscript. Cabot, A. and Llorca, J. guided the project and supervised the work. Soler, L. and Llorca, J. designed the hydrogen production experiments. Xing, C., Zhang, Y., and Liu, J. produced the samples. Liu, Y.; Sivula, K.; Guijarro, N. and Zuo, Y. performed the electrochemical measurements and analyzed the results. Li, J. and Du, R. performed XRD measurements and discussed. Zhang, T.; Tang, P. and Arbiol, J. performed HRTEM measurements and discussed.

### Chapter 3

**Xing, C.;** Liu, Y.; Zhang, Y.; Wang, X.; Guardia, P.; Yao, L.; Han, X.; Zhang, T.; Arbiol, J.; Soler, L.; Chen, Y.; Sivula, K.; Guijarro, N.; Cabot, A.; Llorca, J. A Direct Z-Scheme for the Photocatalytic Hydrogen Production from a Water Ethanol Mixture on CoTiO<sub>3</sub>/TiO<sub>2</sub> Heterostructures. *ACS Appl. Mater. Interfaces* **2021**, *13* (1), 449–457.

Impact factor 2019: **8.758**

In this work, Xing, C.; Liu, Y.; Zhang, Y.; Wang, X.; Cabot, A. and Llorca, J. conceived and prepared the manuscript. Cabot, A. and Llorca, J. guided the project and supervised the work. Soler, L.; Chen, Y. and Llorca, J. designed the hydrogen production experiments. Xing, C. and Zhang, Y. produced the samples. Liu, Y.; Yao, L.; Sivula, K. and Guijarro, N. performed the electrochemical measurements and analyzed the results. Yao, L. performed PL and TRPL experiments and analyzed the results. Han, X.; Zhang, T. and Arbiol, J. performed HRTEM and STEM-EELS and discussed these results. Soler, L. and Llorca, J. performed the XPS measurements and discussed these results.

### Chapter 4:

**Xing, C.;** Zhang, Y.; Liu, Y.; Wang, X.; Li, J.; Martínez-Alanis, P. R.; Spadaro, M. C.; Guardia, P.; Arbiol, J.; Llorca, J.; Cabot, A. Photodehydrogenation of ethanol over Cu<sub>2</sub>O/TiO<sub>2</sub> heterostructures. *Nanomaterials* **2021**, *11* (6), 1399.

Impact factor 2019: **4.034**

Cabot, A. and Llorca, J. guided the project and supervised the work. Xing, C.; Zhang, Y.; Wang, X.; Martínez-Alanis, P.R. and Cabot, A. conceived and prepared the manuscript. Llorca, J. designed the hydrogen production experiments. Xing, C. and Zhang, Y. produced the samples. Zhang, Y. and Llorca, J. performed the electrochemical measurements and analyzed the results. Liu, Y. performed PL and TRPL experiments and analyzed the results. Guardia, P.; Spadaro, M.C. and Arbiol, J. performed TEM, HRTEM and STEM-EELS and discussed these results. Llorca, J. performed XPS

measurements and discussed these results. The manuscript was corrected and improved by all authors.

Prof. Andreu Cabot and Prof. Jordi Llorca certify the information provided above is true.

Barcelona, 24<sup>th</sup> of May 2021

# Content

Preface .....	I
Acknowledgements .....	II
List of publications.....	IV
Authors' contributions.....	V
Abstract .....	1
Resumen.....	3
Resum.....	5
Chapter 1 General Introduction .....	7
1.1 Background of photocatalysis.....	7
1.2 TiO <sub>2</sub> -based photocatalysts.....	8
1.3 Mechanism of photocatalysis .....	9
1.4 Semiconductor heterojunction photocatalysts .....	12
1.4.1 Type-I heterojunction.....	12
1.4.2 Type-II heterojunction .....	12
1.4.3 Type-III heterojunction .....	16
1.5 Methods and main strategies to produce TiO <sub>2</sub> .....	16
1.5.1 <i>Solvothermal method</i> .....	16
1.5.2 Sol-Gel Method .....	17
1.5.3 Colloidal method .....	17
1.6 Objectives .....	18
1.7 References .....	19
Chapter 2 Porous NiTiO <sub>3</sub> /TiO <sub>2</sub> nanostructures for photocatalytic hydrogen evolution ...	25
2.1 Abstract .....	25
2.2 Introduction .....	26
2.3 Experimental Section .....	27
2.4 Results and discussion .....	30
2.5 Conclusions .....	44
2.6 References.....	45
Chapter 3 A Direct Z-Scheme for the Photocatalytic Hydrogen Production from a Water Ethanol Mixture on CoTiO <sub>3</sub> /TiO <sub>2</sub> Heterostructures .....	50

<b>3.1 Abstract</b> .....	50
<b>3.2 Introduction</b> .....	51
<b>3.3 Experimental Section</b> .....	54
<b>3.4 Result and discussion</b> .....	57
<b>3.5 Conclusions</b> .....	76
<b>Chapter 4 Photodehydrogenation of ethanol over Cu<sub>2</sub>O/TiO<sub>2</sub> heterostructures</b> .....	82
<b>4.1 Abstract</b> .....	82
<b>4.2 Introduction</b> .....	83
<b>4.3 Materials and Methods</b> .....	86
<b>4.4 Results and discussion</b> .....	89
<b>4.5 Conclusions</b> .....	103
<b>4.6 References</b> .....	104
<b>Result and Discussions</b> .....	109
<b>Conclusions</b> .....	113
<b>Curriculum Vitae</b> .....	116
<b>Annex</b> .....	119

## Abstract

The photocatalytic production of hydrogen from water and biomass derivatives such as ethanol, glycerol and sugars is a highly attractive strategy to generate environmentally benign hydrogen. Ethanol is more easily oxidized than water by holes in the valence band (VB) of photoexcited semiconductors, which also helps to suppress the recombination of electron-hole pairs, thus increasing the usage of electrons in the conduction band (CB) of photoexcited semiconductors to yield hydrogen. Furthermore, ethanol is a renewable resource that is readily produced by conventional fermentation of sugars and starch.

Titanium dioxide (TiO<sub>2</sub>) has been widely investigated in the field of photocatalysis due to its photosensitivity, low cost, natural abundance, non-toxicity, and good chemical and thermal stability. However, the solar energy conversion efficiency of TiO<sub>2</sub> is hindered by its large bandgap (3.2 eV). Here, we demonstrate that the combination of TiO<sub>2</sub> with Ni, Co and Cu can substantially promote local spatial charge separation and proton activation in TiO<sub>2</sub>, achieving high-efficiency for H<sub>2</sub> photoproduction.

In chapter 2, we present a strategy to produce porous NiTiO<sub>3</sub>/TiO<sub>2</sub> nanostructures with excellent photocatalytic activity toward hydrogen generation. Nickel-doped TiO<sub>2</sub> needle bundles were synthesized by a hydrothermal procedure. Through the sintering in air of these nanostructures, porous NiTiO<sub>3</sub>/TiO<sub>2</sub> heterostructured rods were obtained. Alternatively, the annealing in argon of the nickel-doped TiO<sub>2</sub> needle bundles resulted in NiO<sub>x</sub>/TiO<sub>2</sub> elongated nanostructures. Porous NiTiO<sub>3</sub>/TiO<sub>2</sub> structures were tested for hydrogen evolution in the presence of ethanol. Such porous heterostructures exhibited superior photocatalytic activity toward hydrogen generation, with hydrogen production rates up to 11.5 mmol h<sup>-1</sup> g<sup>-1</sup> at room temperature. This excellent performance is related here to the optoelectronic properties and geometric parameters of the material. The results were published in *Journal of Materials Chemistry A* in 2019.

In chapter 3, CoTiO<sub>3</sub>/TiO<sub>2</sub> composite catalysts with controlled amounts of highly distributed CoTiO<sub>3</sub> nanodomains for photocatalytic ethanol dehydrogenation are developed and studied. To take advantage of solar light, the CoTiO<sub>3</sub> nanoparticles with a band gap around 2.3 eV were synthesized by a hydrothermal procedure. We demonstrate these materials to provide outstanding hydrogen evolution rates under UV and visible illumination. The origin of this

enhanced activity is extensively analysed. In contrast to previous assumptions, UV-vis absorption spectra and ultraviolet photoelectron spectroscopy (UPS) prove CoTiO<sub>3</sub>/TiO<sub>2</sub> heterostructures to have a type II band alignment, with the CB minimum of CoTiO<sub>3</sub> below the H<sup>+</sup>/H<sub>2</sub> energy level. Additional steady-state photoluminescence (PL) spectra, time-resolved PL spectra (TRPLS), and electrochemical characterization prove such heterostructures to result in enlarged lifetimes of the photogenerated charge carriers. These experimental evidences point toward a direct Z-scheme as the mechanism enabling the high photocatalytic activity of CoTiO<sub>3</sub>/TiO<sub>2</sub> composites toward ethanol dehydrogenation. In addition, we probe small changes of temperature to strongly modify the photocatalytic activity of the materials tested, which could be used to further promote performance in a solar thermo-photocatalytic reactor. The results were published in *ACS Applied Materials & Interfaces* in 2021.

The optimization of photodehydrogenation of ethanol requires the use of highly active, stable and selective photocatalytic materials based on abundant elements, and the proper adjustment of the reaction conditions, including temperature. In chapter 3, Cu<sub>2</sub>O-TiO<sub>2</sub> type-II heterojunctions with different Cu<sub>2</sub>O amounts are obtained by a one-pot hydrothermal method. The structural and chemical properties of the produced materials and their activity toward ethanol photodehydrogenation under UV and visible light illumination are evaluated. The Cu<sub>2</sub>O-TiO<sub>2</sub> photocatalysts exhibit high selectivity toward acetaldehyde production and up to tenfold higher hydrogen evolution rates compared to bare TiO<sub>2</sub>. We further discern here the influence of temperature and visible light absorption on photocatalytic performance. Our results point toward the combination of energy sources in thermo-photocatalytic reactors as an efficient strategy for solar energy conversion. The results were published in *Nanomaterials* in 2021.

# Resumen

La producción fotocatalítica de hidrógeno a partir de agua y derivados de biomasa como etanol, glicerol y azúcares es una reacción atractiva para proporcionar hidrógeno sin apenas impacto ambiental. El etanol se oxida más fácilmente que el agua por los huecos en la banda de valencia de los semiconductores fotoexcitados, suprimiendo la recombinación de pares electrón-hueco y, por lo tanto, aumentando la reactividad de los electrones en la banda de conducción de los semiconductores fotoexcitados para producir hidrógeno. Además, el etanol es un recurso renovable que se produce fácilmente mediante la fermentación convencional de azúcares y almidón.

El dióxido de titanio ( $\text{TiO}_2$ ) ha sido ampliamente investigado en el campo de la fotocatalisis debido a su fotosensibilidad, bajo costo, abundancia natural, no toxicidad y buena estabilidad química y térmica. Sin embargo, la eficiencia de conversión de energía solar del  $\text{TiO}_2$  se ve obstaculizada por su gran banda prohibida (3,2 eV). Aquí, demostramos que la incorporación de Ni, Co y Cu puede promover sustancialmente la separación de cargas locales y la activación de protones por el  $\text{TiO}_2$ , logrando una alta eficiencia en la fotoproducción de  $\text{H}_2$ .

En el capítulo 2, presentamos una estrategia para producir nanoestructuras porosas de  $\text{NiTiO}_3/\text{TiO}_2$  con excelente actividad fotocatalítica hacia la generación de hidrógeno. En el capítulo 2, se sintetizaron agujas de  $\text{TiO}_2$  dopado con níquel mediante un procedimiento hidrotermal. Mediante la sinterización al aire de estas nanoestructuras se obtuvieron heteroestructuras en forma de varillas de  $\text{NiTiO}_3/\text{TiO}_2$  porosas. Alternativamente, el tratamiento térmico bajo argón de las varillas de  $\text{TiO}_2$  dopado con níquel dió como resultado nanoestructuras alargadas de  $\text{NiO}_x/\text{TiO}_2$ . Las estructuras porosas de  $\text{NiTiO}_3/\text{TiO}_2$  se ensayaron para determinar la producción de hidrógeno en presencia de etanol. Tales heteroestructuras porosas exhibieron una actividad fotocatalítica superior hacia la generación de hidrógeno, con tasas de producción de hasta  $11,5 \text{ mmol h}^{-1} \text{ g}^{-1}$  de hidrógeno a temperatura ambiente. Este excelente rendimiento se relaciona con las propiedades optoelectrónicas y los parámetros geométricos del material. Los resultados se publicaron en *Journal of Materials Chemistry A* en 2019.

Para aprovechar la luz solar, se sintetizaron nanopartículas de  $\text{CoTiO}_3$  con un intervalo de banda de alrededor de 2.3 eV mediante un procedimiento de sinterización hidrotermal. En el capítulo 3, se prepararon catalizadores compuestos  $\text{CoTiO}_3/\text{TiO}_2$  con cantidades controladas

de nanodominios  $\text{CoTiO}_3$  altamente distribuidos para la deshidrogenación fotocatalítica de etanol. Demostramos que estos materiales presentan una actividad fotocatalítica de generación de hidrógeno excepcionales bajo iluminación UV y visible. El origen de esta actividad se analiza ampliamente. En contraste con las suposiciones anteriores, los espectros de absorción UV-vis y la espectroscopia de fotoelectrones ultravioleta (UPS) demuestran que las heteroestructuras de  $\text{CoTiO}_3/\text{TiO}_2$  tienen una alineación de banda de tipo II, con la banda de conducción del  $\text{CoTiO}_3$  por debajo del nivel de energía  $\text{H}^+/\text{H}_2$ . Los espectros de fotoluminiscencia (PL), los espectros de PL resueltos en el tiempo (TRPLS) y la caracterización electroquímica demuestran que tales heteroestructuras dan como resultado una mayor vida útil de los portadores de carga fotogenerados. Estas evidencias experimentales apuntan hacia un esquema Z directo como el mecanismo que permite la alta actividad fotocatalítica de los compuestos  $\text{CoTiO}_3/\text{TiO}_2$  hacia la deshidrogenación del etanol. Además, se analizó el efecto de la temperatura en la actividad fotocatalítica de los materiales probados, lo que podría usarse para promover aún más el rendimiento en un reactor solar termo-fotocatalítico. Los resultados se publicaron en *ACS Applied Materials & Interfaces* en 2021.

La optimización de la fotodeshidrogenación del etanol requiere el uso de materiales fotocatalíticos altamente activos, estables y selectivos basados en elementos abundantes y el adecuado ajuste de las condiciones de reacción, incluida la temperatura. En el capítulo 3, se obtuvieron heterouniones  $\text{Cu}_2\text{O}-\text{TiO}_2$  tipo II con diferentes cantidades de  $\text{Cu}_2\text{O}$  mediante un método hidrotermal en un solo paso. Se evalúan las propiedades estructurales y químicas de los materiales producidos y su actividad hacia la fotodeshidrogenación de etanol bajo iluminación UV y con luz visible. Los fotocatalizadores  $\text{Cu}_2\text{O}-\text{TiO}_2$  muestran una alta selectividad hacia la producción de acetaldehído e hidrógeno hasta diez veces más altas en comparación con el  $\text{TiO}_2$ . También discernimos aquí la influencia de la temperatura y la absorción de luz visible en el rendimiento fotocatalítico. Nuestros resultados apuntan a la combinación de fuentes de energía en reactores termo-fotocatalíticos como una estrategia eficiente para la conversión de energía solar. Los resultados se publicaron en *nanomateriales* en 2021.

## Resum

La producció fotocatalítica d'hidrogen a partir de derivats de l'aigua i de la biomassa com l'etanol, el glicerol i els sucres és una reacció atractiva per proporcionar hidrogen benigne per al medi ambient. L'etanol s'oxida més fàcilment que l'aigua mitjançant forats de la banda de valència dels semiconductors fotoexcitats, suprimint la recombinació de parells electró-forat i, per tant, augmentant la reactivitat dels electrons en la banda de conducció dels semiconductors fotoexcitats per produir hidrogen. A més, l'etanol és un recurs renovable que es produeix fàcilment mitjançant la fermentació convencional de sucres i midó. El diòxid de titani ( $\text{TiO}_2$ ) ha estat àmpliament investigat en el camp de la fotocatalisi a causa de la seva fotosensibilitat, baix cost, abundància natural, no toxicitat i bona estabilitat química i tèrmica. No obstant això, l'eficiència de conversió d'energia solar de  $\text{TiO}_2$  es veu obstaculitzada per la seva gran amplada de banda (3,2 eV) i la alta taxa de recombinació dels portadors fotogenerats. Aquí demostrem que el Ni, Co i Cu poden promoure substancialment la separació de càrregues i l'activació de protons en el  $\text{TiO}_2$ , aconseguint una alta eficiència per a la fotoproducció d' $\text{H}_2$ .

En el capítol 2, presentem una estratègia per produir nanoestructures poroses de  $\text{NiTiO}_3/\text{TiO}_2$  amb una excel·lent activitat fotocatalítica cap a la generació d'hidrogen. Al capítol 2, es van sintetitzar agulles de  $\text{TiO}_2$  dopades amb níquel itjançant un procediment hidrotermal. Mitjançant la sinterització a l'aire d'aquestes nanoestructures es van obtenir agulles heteroestructurades poroses de  $\text{NiTiO}_3/\text{TiO}_2$ . Com a alternativa, el tractament tèrmic en argó de les agulles de  $\text{TiO}_2$  dopades amb níquel va donar lloc a nanoestructures allargades de  $\text{NiOx}/\text{TiO}_2$ . Es van provar les estructures poroses de  $\text{NiTiO}_3/\text{TiO}_2$  per a la producció d'hidrogen en presència d'etanol. Aquestes heteroestructures poroses presentaven una activitat fotocatalítica superior cap a la generació d'hidrogen, amb taxes de producció de fins a  $11.5 \text{ mmol h}^{-1} \text{ g}^{-1}$  d'hidrogen a temperatura ambient. Aquest excel·lent rendiment està relacionat amb les propietats optoelectròniques i els paràmetres geomètrics del material. Els resultats es van publicar a *Journal of Materials Chemistry A* el 2019.

Per aprofitar la il·luminació solar, es van sintetitzar nanopartícules de  $\text{CoTiO}_3$  amb una banda adequada al voltant de 2,3 eV mitjançant un procediment de sinterització hidrotermal. Al capítol 3, els catalitzadors compostos  $\text{CoTiO}_3/\text{TiO}_2$  amb quantitats controlades de nanodominis distribuïts de  $\text{CoTiO}_3$  es van provar per a la deshidrogenació fotocatalítica d'etanol. Demostrem que aquests materials proporcionen velocitats d'evolució d'hidrogen

excepcionals sota il·luminació UV i visible. S'analitza a fons l'origen d'aquesta activitat millorada. En contrast amb els supòsits anteriors, els espectres d'absorció UV-vis i l'espectroscòpia de fotoelectrons ultraviolats (UPS) demostren que les heteroestructures  $\text{CoTiO}_3/\text{TiO}_2$  tenen una alineació de banda de tipus II, amb la banda de conducció mínima de  $\text{CoTiO}_3$  per sota del nivell d'energia  $\text{H}^+/\text{H}_2$ . Els espectres addicionals de fotoluminescència en estat estacionari (PL), espectres PL resolts en el temps (TRPLS) i caracterització electroquímica demostren que aquestes heteroestructures donen lloc a una vida més gran dels portadors de càrrega fotogenerats. Aquestes evidències experimentals apunten cap a un esquema Z directe com el mecanisme que permet l'alta activitat fotocatalítica dels compostos  $\text{CoTiO}_3/\text{TiO}_2$  cap a la deshidrogenació de l'etanol. A més, explorem els efectes derivats de petits canvis de temperatura sobre l'activitat fotocatalítica dels materials provats, que es podria utilitzar per afavorir encara més el rendiment en un reactor solar termofotocatalític. Els resultats es van publicar a *ACS Applied Materials & Interfaces* el 2021.

L'optimització de la fotodehidrogenació de l'etanol requereix l'ús de materials fotocatalítics altament actius, estables i selectius basats en elements abundants i l'adequat ajust de les condicions de reacció, inclosa la temperatura. Al capítol 3, s'obtenen heterojuncions de tipus  $\text{Cu}_2\text{O}-\text{TiO}_2$  tipus II amb diferents quantitats de  $\text{Cu}_2\text{O}$  mitjançant un mètode hidrotermal en una etapa. S'avaluen les propietats estructurals i químiques dels materials produïts i la seva activitat cap a la fotodehidrogenació d'etanol sota la il·luminació UV i llum visible. Els fotocatalitzadors  $\text{Cu}_2\text{O}-\text{TiO}_2$  presenten una alta selectivitat cap a la producció d'acetaldehid i hidrogen fins a deu vegades més altes que el  $\text{TiO}_2$ . Aquí també discernim la influència de la temperatura i l'absorció de llum visible en el rendiment fotocatalític. Els nostres resultats apunten a la combinació de fonts d'energia en reactors termofotocatalítics com una estratègia eficient per a la conversió d'energia solar. Els resultats es van publicar en *Nanomaterials* el 2021.

# Chapter 1 General Introduction

## 1.1 Background of photocatalysis

In the past decades, with the rapid population expansion and the rampant industrialization, wastewater discharge, air pollution and the disposal of solid waste have caused serious environmental pollution.<sup>1,2</sup> Environmental pollution and energy shortages are a serious threat to the sustainable development of human society, and are two major challenges facing the world today.<sup>3,4</sup> Renewable energy technologies are clean sources of energy that have a much lower environmental impact than conventional energy technologies.<sup>5,6</sup> Besides, renewable energy can help to reduce dependence on traditional fossil fuels given its inexhaustible character, making them the cleanest, most viable solution to prevent environmental degradation.<sup>7,8</sup>

Among renewable energies, solar energy is the most abundant. 173,000 terawatts of solar energy strike the Earth continuously, which is 10,000 times more than the world's total energy use.<sup>9,10</sup> Solar energy has enormous advantages over many other sources of energy, which include low cost, pollution free and can reduce our reliance on fossil fuels, what makes it one of the most promising energy sources in moving to a clean and sustainable future.<sup>11,12</sup> In this direction, photocatalysis, which can directly convert and store solar energy into chemical energy, is one of the most viable processes to alleviate and even solve both the global energy crisis and environmental pollution.<sup>13,14</sup>

The commonly used photocatalysts belong to three main groups: 1) oxide-based photocatalyst, such as  $\text{TiO}_2$ <sup>15</sup>,  $\text{ZnO}$ <sup>16</sup>,  $\text{RuO}_2$ <sup>17</sup>,  $\text{CuO}$ <sup>18</sup>,  $\text{Fe}_2\text{O}_3$ <sup>19</sup>,  $\text{Ta}_2\text{O}_5$ <sup>20</sup>,  $\text{NiO}$ <sup>21</sup>,  $\text{Cr}_2\text{O}_3$ <sup>22</sup>, exhibit excellent photocatalytic activities along with well-controlled structure, surface and crystalline features, and a high stability which makes them widely used in a variety of applications; 2) Chalcogenide-based binary photocatalysts (CBBPs)  $\text{CdS}$ <sup>23</sup>,  $\text{ZnS}$ <sup>24</sup>,  $\text{MoS}_2$ <sup>25</sup>,  $\text{SnS}_2$ <sup>26</sup>, etc. CBBPs have a suitable band gap. However, due to the photo-corrosion effect, even with the presence of sacrificial agents, CBBPs are not stable in long-term photocatalytic reactions. 3) Nitride-based binary photocatalysts  $\text{C}_3\text{N}_4$ .  $\text{C}_3\text{N}_4$

has a layered structure similar to graphite, C and N atoms form a highly delocalized  $\pi$ -conjugated electron band structure through  $sp^2$  hybridization. The band gap is 2.7 eV, and the CB is above the redox potential of hydrogen. The VB is below the oxidation-reduction potential. However,  $C_3N_4$  exhibits small specific surface area, high exciton binding energy of photo-generated carriers, and high recombination rates, which hamper its application in photocatalytic water splitting. This thesis focuses on  $TiO_2$ , which is the most common and well recognized as cost-effective, efficient, stable, and most importantly, environmentally friendly photocatalyst for a sustainable approach for environmental protection.

## **1.2 $TiO_2$ -based photocatalysts**

Among the many semiconductors that have been developed for photocatalysis,  $TiO_2$  is the most investigated because of its high photocatalytic activity, low price, high availability, non-toxicity and excellent photostability.<sup>27</sup>  $TiO_2$  photocatalysts show high potential application in a number of fields, including water splitting, self-cleaning surfaces, water, air and wastewater treatment, and photoelectrochemical conversion.<sup>28</sup> The photocatalytic activity of  $TiO_2$  closely depends on the crystallographic phase. There exist three main crystal structures of  $TiO_2$ : anatase, brookite and rutile.<sup>29</sup> Both anatase and brookite phases are metastable, while anatase exhibit higher photocatalytic activity. The rutile is the most stable phase but with less activity. Catalysis takes place at the material and different surface facets can display different properties.<sup>30</sup> Down to nanoscale size, the chemical and physical properties of a material are fundamentally related to surface features. Considering this effect, researchers have paid tremendous attention to adjust material properties by precisely engineering the material surface, especially on the specific facets.<sup>31</sup> During the synthesis of nanomaterials, the main challenge is how to expose/maximize a certain facet on the surface of nanocrystals, which has a positive effect on the semiconductor photocatalytic activity.<sup>32</sup>

The detailed reaction kinetics and mechanisms of photocatalytic reaction on  $TiO_2$  have been investigated by using a number of molecular spectroscopies, that accelerate the development of various types of  $TiO_2$  based photocatalytic materials.<sup>33-41</sup> In 1972,

Fujishima and Honda first reported UV-light assisted photoelectrolysis of H<sub>2</sub>O into H<sub>2</sub> and O<sub>2</sub> by using a TiO<sub>2</sub> photoanode in a photoelectrochemical cell.<sup>42</sup> After this pioneering work, a significant amount of interest followed in the field of photocatalysis for H<sub>2</sub> production, CO<sub>2</sub> reduction and pollutant degradation.<sup>43-46</sup> Compared with thermal catalysis and electrocatalysis, photocatalysis possesses several advantages, including: 1) mild reaction condition, the photocatalytic reduction or oxidation reaction can be carried out at room temperature and pressure, and does not require high temperature and high pressure conditions;<sup>47</sup> 2) effective and complete reaction, photocatalytic oxidation can directly oxidize pollutants in the air or water into non-toxic and harmless H<sub>2</sub>O and CO<sub>2</sub> without any secondary pollution;<sup>48</sup> 3) green energy, photocatalytic technology can convert solar energy into high-densified chemical energy, realizing photocatalytic decomposition of water to produce hydrogen, reducing CO<sub>2</sub> into valuable fuels (hydrocarbons, alcohols, etc.);<sup>49</sup> 4) powerful oxidizing performance, photocatalytic reaction is capable to generate strong oxidizing hydroxyl radicals and superoxide radicals, whose oxidizing ability is higher than common oxidants such as ozone and hydrogen peroxide, and it is of special significance in decomposing organics that are difficult to degrade;<sup>50</sup> 5) long lifetime: photocatalysts are not consumed in the catalyzed reaction but can act repeatedly.<sup>51-</sup>

54

In summary, photocatalysis is a promising technology to convert clean and inexhaustible solar energy into storable chemical energy. It has the advantages of low cost, environmentally friendly, safety, and renewable, and the development of highly efficient photocatalytic systems is highly desirable in dealing with energy crisis and environmental governance.

### **1.3 Mechanism of photocatalysis**

The photocatalyst utilizes the energy delivered by light and modifies the rate of a chemical reaction without itself being involved in the chemical transformation.<sup>55,56</sup> The principle of photocatalysis is based on the activation of a semiconductor material by photonic radiation with energy equal to or higher than the bandgap energy, which leads to the creation of photo-activated electron/hole (e<sup>-</sup>/h<sup>+</sup>) pairs.<sup>57</sup> A large portion

of the photogenerated  $e^-$  and  $h^+$  will recouple, while the rest carriers will migrate to the surface and trigger a series of chemical reactions with the adsorbed substances on the surface of the photocatalyst.<sup>58</sup> The electrons in the CB can be utilized to reduce a substrate, whereas the holes in the VB can be used to oxidize compounds.<sup>59,60</sup> When the oxidation and reduction potentials of a reaction lie between the VB and CB potentials of the photocatalyst, the surface oxidation and reduction can be initiated by photoexcited carriers ( $e^-/h^+$ ).<sup>61,62</sup> The band positions for some frequently used semiconductor photocatalysts are listed in Figure 1. In particular, photocatalytic water splitting is a typical and promising hydrogen production reaction which requires the CB of photocatalyst to be at a potential less than 0 V.<sup>63</sup> NHE ( $H^+/H_2$ ) while the VB needs to be at a potential more than 1.23 V.<sup>64</sup> It includes three steps: 1) light irradiation on semiconductor with photons' energy above the bandgap, to generate electrons and holes in the conduction and the VB;<sup>65</sup> 2) the excited electrons and holes are separated followed by migrating to the surface of the semiconductor particles;<sup>66</sup> 3) chemical reactions occur on the surface, the electrons reduce water to form hydrogen while the holes oxidize water to form oxygen, respectively, as shown in Figure 1. Meanwhile, it should be noted that recombination of holes and electrons can happen on a fast rate without participating the water splitting reaction.<sup>67</sup>

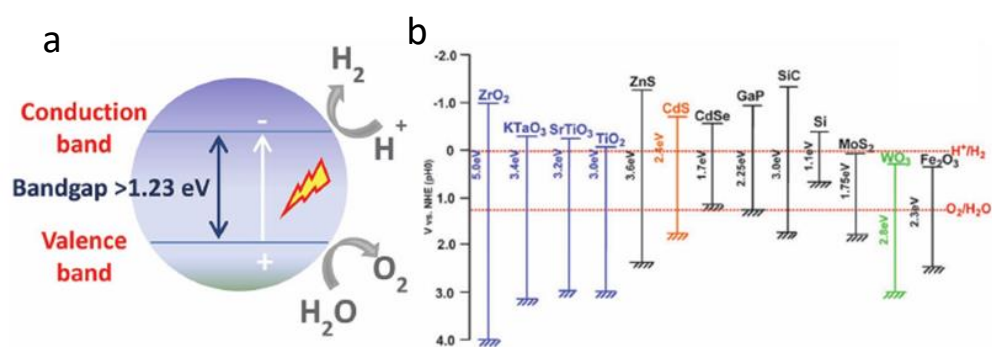


**Figure 1.** Photocatalytic H<sub>2</sub>O splitting. (a) Schematic of H<sub>2</sub>O splitting applying semiconductor photocatalyst. (b) Band structure of various semiconductors and redox potentials of H<sub>2</sub>O splitting.<sup>68</sup>

The main limitation of photocatalytic water splitting is using pure water as reagent which is quite inefficient or even not applicable at all.<sup>69</sup> This is because the

simultaneous oxidation and reduction of water is rather complex, involving four electrons transfer.<sup>70</sup> One effective way to solve this problem is to introduce a sacrificial reagent as electron donor that can significantly improve the H<sub>2</sub> production.<sup>71</sup> In this direction, charge carrier recombination would be greatly reduced as holes are removed by the sacrificial reagent.<sup>72</sup> In addition, when O<sub>2</sub> production is suppressed, the recombination of H<sub>2</sub> and O<sub>2</sub> to produce water is restrained, increasing the H<sub>2</sub> yield.

Ethanol is one of the most common sacrificial agents. The photodehydrogenation of ethanol to produce molecular hydrogen and acetaldehyde using solar light as the only energy input is especially appealing.<sup>73,74</sup> As a liquid, ethanol can be easily stored and transported. Besides, ethanol can be easily produced from several biomass-derived feedstocks and organic residues such as sewage sludge.<sup>75-77</sup> Additionally, bioethanol aqueous solutions can be directly used, without the need for purification. Compared with water splitting, the production of hydrogen from ethanol is thermodynamically advantageous ( $\Delta G^0 = +237 \text{ kJ}\cdot\text{mol}^{-1}$  for water oxidation vs.  $\Delta G^0 = +41.5 \text{ kJ}\cdot\text{mol}^{-1}$  for ethanol oxidation to acetaldehyde), which decreases the energy input required to drive hydrogen production.<sup>78,79</sup> Compared with water splitting, ethanol dehydrogenation also enables a much simpler product purification, preventing the H<sub>2</sub> and O<sub>2</sub> back reaction. Besides, compared with ethanol photo-reforming, ethanol photodehydrogenation to H<sub>2</sub> and acetaldehyde could have a threefold higher economical profitability associated with the high economic value of the side product.<sup>80</sup>

In the simplest scenario, ethanol can be photo-catalytically dehydrogenated at ambient pressure and temperature, yielding molecular hydrogen and acetaldehyde and releasing no CO<sub>2</sub>



Acetaldehyde is a particularly versatile chemical precursor extensively used by the chemical industry because the aldehyde moiety provides a functional handle that, through different reaction pathways, can be used to yield a range of products, including upgraded fuels as well as large volume commodity chemicals such as acetic acid or butadiene, among others.<sup>81-84</sup>

## 1.4 Semiconductor heterojunction photocatalysts

One critical factor that determines the efficiency of photocatalysis is the separation and distribution of photoactivated electron/hole pairs. To achieve high photocatalytic performance, it is required to separate the generated electron/hole pairs efficiently, and at the same time to transport them to active sites rapidly for the desired reactions to be activated.<sup>85</sup> In addition, charge recombination either at the surfaces or in the space charge region should be minimized. Construction of semiconductor heterostructures is an effective approach to improve charge separation for enhanced photocatalytic activity. According to band alignment characteristics, the semiconductor heterostructures can be generally classified into three main groups: type-I straddling heterojunction, type-II staggered heterojunction, and type III broken-gap heterojunction, as illustrated in Figure 2.<sup>86</sup>

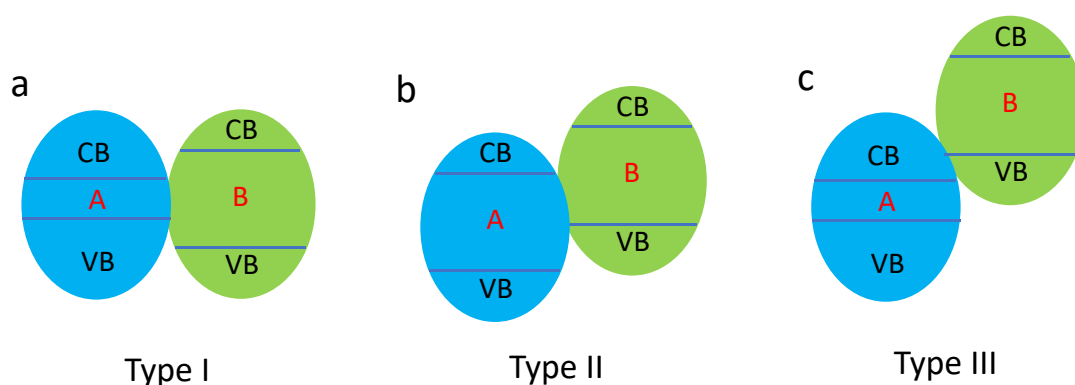


**Figure 2.** Scheme of the three typical types of heterojunctions. (a) type I, (b) type II, (c) type III, where A and B represent two different semiconductors.

### 1.4.1 Type-I heterojunction

In a type I heterojunction, both VB and CB edges of semiconductor B are localized within the energy gap of semiconductor A, forming straddling band alignment (Figure 2a). Since electrons and holes gain energy by moving down and up respectively, photoexcited electrons can transfer from CB(B) to CB(A), while the holes can be transferred from VB(B) to VB(A) when the contact between both materials is sufficient.

### 1.4.2 Type-II heterojunction

In a type-II heterojunction, the CB minimum (CBM) of semiconductor A is at a lower energy position **than that of semiconductor B**. Besides the valence band maximum

(VBM) of semiconductor A is at a higher energy than the VBM of semiconductor B. **Therefore**, a driving force exist for photogenerated electrons in the CB(b) to move to CB(A) and photogenteated holes from VB(A) to move to VB(B). **Thus holes** concentrate **in the VB(B)** and **electrons concentrated in the CB(A)**.

#### 1.4.2.1 Conventional type-II heterojunction photocatalytic mechanism

In a type-II heterojunction usually photogenerated electrons are driven from part B to part A because of the higher negative potential of B, while the photoexcited holes transfer from A to B at the same time. This kind of band alignment is specifically beneficial for charge separation, which makes the type-II heterojunction more suitable for photocatalytic application than the type-I heterojunction. The suitable metal oxides contacted with TiO<sub>2</sub> to form the type II heterostructures has been studied extensively. We reported a hydrothermal synthetic method to fabricate a type-II structure Cu<sub>2</sub>O/TiO<sub>2</sub>, and investigated the photocatalytic activity of different molar ratios of TiO<sub>2</sub> and Cu<sub>2</sub>O in photocatalysis under UV irradiation. Compared with pure TiO<sub>2</sub>, Cu<sub>2</sub>O/TiO<sub>2</sub> heterostructure exhibits enhanced photocatalytic activity due to significantly accelerated surface charge carrier separation and potential barrier at the interface of heterojunction to prevent recombination of electron-hole pairs (Figure 3).<sup>87</sup> In the resulting heterostructure, photogenerated electrons in the CB of Cu<sub>2</sub>O tend to move toward TiO<sub>2</sub>, where hydrogen generation takes place, and photogenerated holes in TiO<sub>2</sub> tend to move toward the Cu<sub>2</sub>O, where ethanol is oxidized to acetaldehyde (Figure 3b).

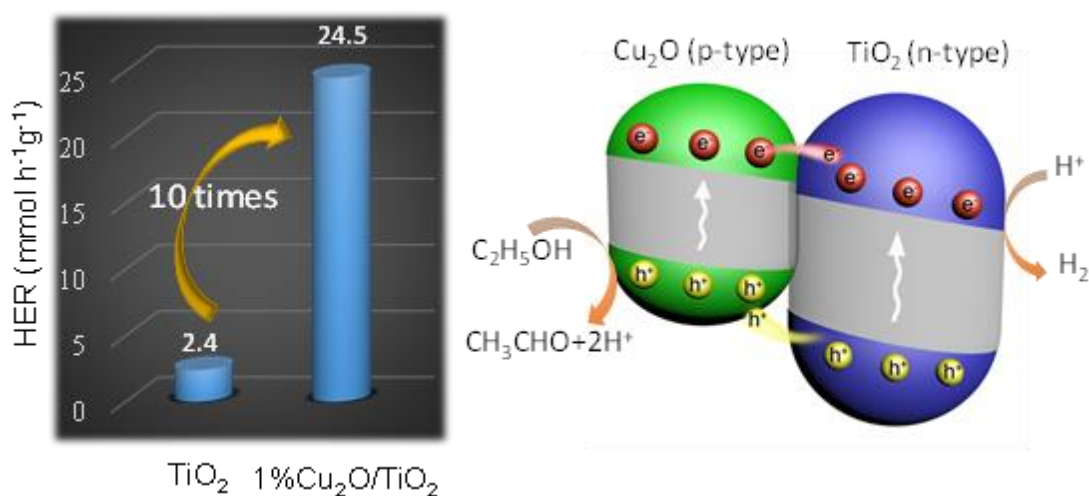


**Figure 3.** (a) HER on TiO<sub>2</sub> and 1% Cu<sub>2</sub>O/TiO<sub>2</sub> nanocomposites under UV light irradiation; (b) Schematic illustration of proposed type-II photocatalytic mechanism of Cu<sub>2</sub>O/TiO<sub>2</sub> heterojunction. <sup>87</sup>

#### 1.4.2.2 Type II heterojunction with Z-scheme mechanism

Although usually the photogenerated electrons and holes in type-II heterojunctions are isolated to greatly reduce their recombination within the framework of the above detailed mechanism, the major drawback of this design is that the redox ability of electrons and holes is weakened, due to electrons transferring to more positive CB and holes transferring to more negative VB. For this concern, it is difficult for a heterostructured photocatalyst to simultaneously achieve effective charge separation and strong redox activity. In a direct Z-Scheme, the CB electrons and VB holes of each semiconductors with lower energy are recombined, thereby retaining the relatively higher energy level of the VB holes and CB electrons. This leads to higher oxidation and reduction capabilities. A Z-scheme photocatalytic process is actually used in photosynthesis, which is a natural reaction processed by green plants that converts water and carbon dioxide into chemical energy under irradiation of sunlight.<sup>88</sup> As show in Figure 4, in a Z-scheme system, the electrons with lower energy in the CB of B recombine with the holes in the VB of A, leaving strongly oxidative holes in the VB of A and strongly reductive electrons in the CB of B, which hold the maximum redox ability from individual semiconductor for catalytic reactions. A Z-scheme mechanism can provide superior photocatalytic performance than that a conventional type II heterojunction mechanism.

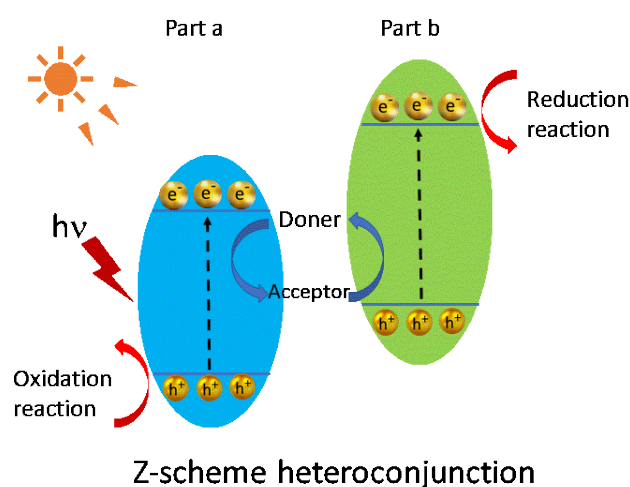


**Figure 4.** Schematic illustration of Z-scheme photocatalytic system.

The direct Z-type mechanism was first proposed by Yu, JG et al.<sup>89</sup> They used commercial TiO<sub>2</sub> P25 and urea as raw materials to prepare a direct Z-scheme g-C<sub>3</sub>N<sub>4</sub>/TiO<sub>2</sub> photocatalyst by a facile calcination route (Figure 5). The photocatalytic activity was evaluated by photocatalytic oxidation and decomposition of formaldehyde in the air. The results showed that the photocatalytic activity of the prepared direct Z photocatalyst was closely related to the loading amount of g-C<sub>3</sub>N<sub>4</sub>. When the g-C<sub>3</sub>N<sub>4</sub> content was optimal, the apparent reaction rate constant of HCHO decomposition was  $7.36 \times 10^{-2} \text{ min}^{-1}$ , which is 2.1 times higher than that of pure P25. The increase in photocatalytic activity was attributed to a direct Z-type photocatalytic mechanism between g-C<sub>3</sub>N<sub>4</sub> and TiO<sub>2</sub>. Under UV irradiation, the holes tend to keep in the VB of TiO<sub>2</sub>, while the electrons transfer to the VB of g-C<sub>3</sub>N<sub>4</sub> from the CB of TiO<sub>2</sub>. The electrons in the VB of g-C<sub>3</sub>N<sub>4</sub> are further excited to its CB. Then, the electrons stored in the CB of g-C<sub>3</sub>N<sub>4</sub> are trapped by O<sub>2</sub> to form  $\cdot\text{O}_2^-$ , meanwhile the holes in the VB of TiO<sub>2</sub> react with adsorbed water molecules to form  $\cdot\text{OH}$ . This direct Z-type photocatalytic mechanism effectively realizes the spatial separation of photo-induced charge carriers and improves the photocatalytic activity of the composite photocatalytic material.

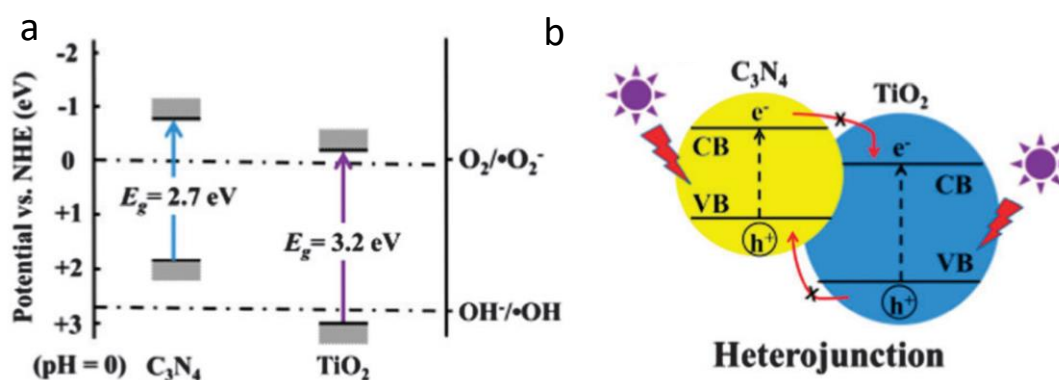


**Figure 5.** (a) Scheme illustrating band positions of g-C<sub>3</sub>N<sub>4</sub> and TiO<sub>2</sub> together with OH/ $\cdot$ OH and O<sub>2</sub>/O<sub>2</sub><sup>-</sup> redox potentials. (b) Conventional g-C<sub>3</sub>N<sub>4</sub>-TiO<sub>2</sub> heterojunctions cannot form.<sup>89</sup>

### 1.4.3 Type-III heterojunction

The type-III heterojunction is similar to the type II, but the VB of B overlaps with the CB of A, which brings a higher force for charge migration and separation. The same mechanisms and concepts discussed for type-II heterojunctions apply for type-II heterojunctions.

## 1.5 Methods and main strategies to produce TiO<sub>2</sub>

Among the different synthetic methods to produce TiO<sub>2</sub> nanostructures, the most common ones are: solvothermal<sup>90</sup> sol-gel,<sup>91</sup> and colloidal methods.<sup>92</sup>

### 1.5.1 Solvothermal method

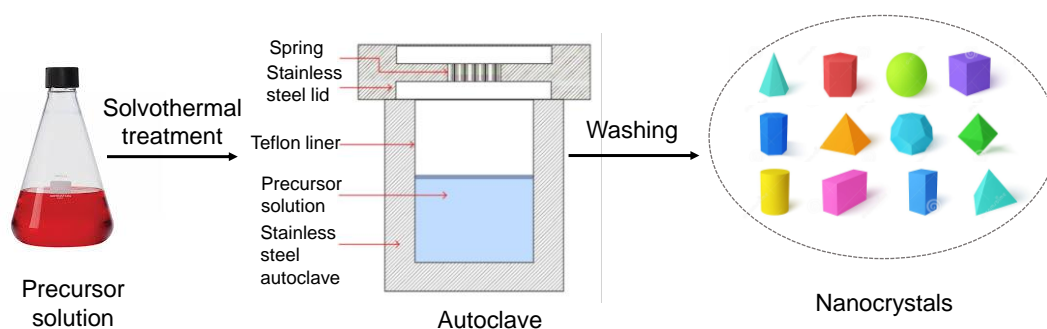


**Figure 6.** Schematic steps involved in solvothermal synthesis.

Solvothermal synthesis is generally defined as a process where the chemical reaction take place in a closed system where a high temperature and pressure can be applied to form desired products in solution (Figure 6). The medium preferred in a solvothermal synthesis can be water, methanol, ethanol, ammonia and any other aqueous or non-aqueous solvent. In the case of water solution as solvent, the term solvothermal reaction changes to hydrothermal reaction. The procedure involves the mixing of the precursors in the solvent and its transfer into a sealed autoclave that will be subsequently heated to temperatures above the boiling point of the solvent. With precise adjusted precursors and reaction conditions, this method allows to produce high quality and homogeneously dispersed TiO<sub>2</sub> nanocrystals with a narrow size distribution. Advantages of this strategy include its ability to synthesize crystal phases that are not stable at boiling temperature, well controlled quality of nanocrystals (size,

morphology and phase) and high-pressure reaction conditions. The major disadvantages of the method lie in the need of autoclaves, and the difficulty to observe the crystal as it grows inside a steel outer shell.<sup>93</sup>

### **1.5.2 Sol-Gel Method**

The sol-gel (S-G) method is a wet-chemical technique that generally involves three main steps: 1) uniformly dissolving high chemically active precursors as raw materials in a liquid solution; 2) hydrolysis of precursors in either acidic or alkali conditions; 3) poly-condensation of the hydrolyzed product forming a three-dimensional polymeric network surrounded with solvent molecules. The network structure is filled with a high-volume percentage of solvent that loses fluidity to form a gel. The physical and chemical properties of final material will be determined by the experimental conditions and parameters. It has been proved that the structure-property of TiO<sub>2</sub> can be well modified through S-G process that provides an easy and simple way to synthesize nanoparticles at ambient temperature and pressure. In addition, this procedure does not involve complicated set-up. It has numerous advantages over other solution-process techniques in term of homogeneity, easy to process, stoichiometry and composition control, high purity and in introducing various dopants in high concentration. Through S-G processing, the growth of TiO<sub>2</sub> colloidal crystals can be effectively controlled in a micrometer/sub-micrometer range by hydrolysis–condensation of titanium alkoxides in aqueous medium.<sup>94</sup>

### **1.5.3 Colloidal method**

Colloidal synthesis methods consist in reacting precursors within a solvent and stabilizing the formed particles as a colloidal suspension typically through the use of surfactants. To prepare uniform-sized nanoparticles, the stages of nucleation and growth are generally separated. For this reason, it is necessary to reduce the energy required for nucleation, make nucleation relatively fast, increase the number of nucleation sites, and quickly consume the reactants after the nucleation of nanoparticles or change the external conditions to terminate the nucleation. To achieve nucleation, the saturation of the reaction solution can be increased by changing the temperature.<sup>95,96</sup>

Surfactants can inhibit the growth of certain surfaces to favor the growth of other surfaces, thereby affecting the growth stage.

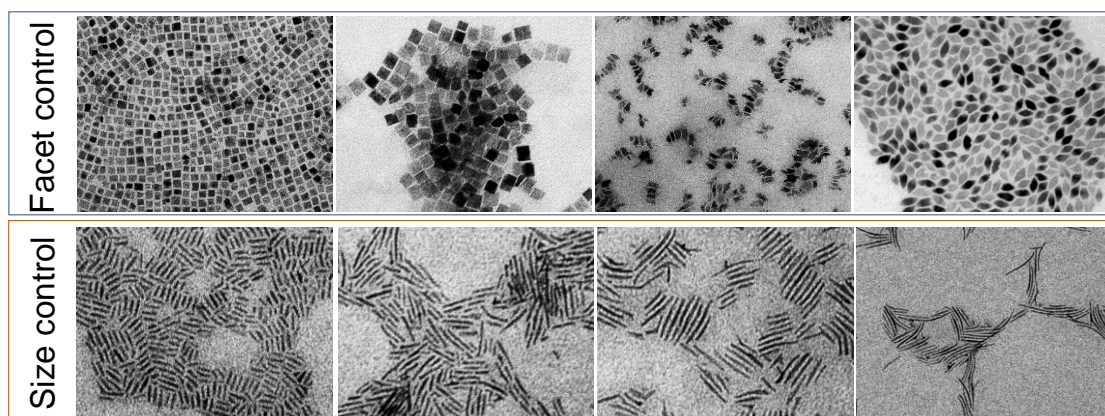


Figure 7. Electron microscopy micrographs of a selection of solution-processed TiO<sub>2</sub> NPs with sizes in the range from 10 nm to around 100 nm produced during my PhD studies at IREC/UPC.

### 1.6 Objectives

Considering all the aspects mentioned above, the goal of this thesis is to develop TiO<sub>2</sub> heterostructured, non-toxic catalysts for photocatalytic hydrogen production. The selected transition metals should be low-cost and non-toxic, and highly efficient in light conversion after using hydrothermal synthesis methods. Keeping these aims in mind, the following objectives have been defined in this thesis:

1. To develop high surface area photocatalysts based on TiO<sub>2</sub>
2. To promote light absorption of TiO<sub>2</sub> photocatalysts.
3. To promote charge separation in TiO<sub>2</sub> photocatalysts.
4. To demonstrate an efficient photocatalytic H<sub>2</sub> evolution from ethanol dehydrogenation.
5. To discern here the influence of temperature and visible light absorption on photocatalytic performance.
6. To determine the photocatalytic mechanism in Cu, Ni and Co-doped TiO<sub>2</sub> photocatalysts.

## 1.7 References

1. Rao, C. S. Environmental Pollution Control Engineering, 2007.
2. Adams, W. W.; Baughman, R. H. Retrospective: Richard E. Smalley (1943–2005). *Science*. **2005**, *310*, 1916.
3. Hopwood, B.; Mellor, M.; O'Brien, G. Sustainable Development: Mapping Different Approaches. *Sustain. Dev.* **2005**, *13*, 38–52.
4. Lélé, S. M. "Sustainable Development" A Critical Review; *World Dev.* **1991**, *19*, 607–621.
5. Panwar, N. L.; Kaushik, S. C.; Kothari, S. Role of Renewable Energy Sources in Environmental Protection: A Review. *Renew. Sustain. Energy Rev.* **2011**, *15*, 1513–1524.
6. Dresselhaus, M. S.; Thomas, I. L. Alternative Energy Technologies. *Nature*. **2001**, *15*, 332–337.
7. Ellabban, O.; Abu-Rub, H.; Blaabjerg, F. Renewable Energy Resources: Current Status, Future Prospects and Their Enabling Technology. *Renew. Sust. Energy Rev.* **2014**, *39*, 748–764.
8. Lund, H. Renewable Energy Strategies for Sustainable Development. *Energy* **2007**, *32*, 912–919.
9. Soteris A. K. Solar Energy Engineering: Processes and Systems. Academic Press, **2013**.
10. Balzani, V.; Credi, A.; Venturi, M. Photochemical Conversion of Solar Energy. *ChemSusChem*. **2008**, *1*, 26–58.
11. Olah, G. A.; Prakash, G. K. S.; Goepfert, A. Anthropogenic Chemical Carbon Cycle for a Sustainable Future. *J. Am. Chem. Soc.* **2011**, *133*, 12881–12898.
12. Chu, S.; Cui, Y.; Liu, N. The Path towards Sustainable Energy. *Nature Materials*. **2017**, *16*, 16–22.
13. Schultz, D. M.; Yoon, T. P. Solar Synthesis: Prospects in Visible Light Photocatalysis. *Science*. **2014**, *343*, 1239176–1239176.
14. Qu, Y.; Duan, X. Progress, Challenge and Perspective of Heterogeneous Photocatalysts. *Chem. Soc. Rev* **2568**, *42*, 2568.
15. Lee, S.-Y.; Park, S.-J. TiO<sub>2</sub> Photocatalyst for Water Treatment Applications. *J. Ind. Eng. Chem.* **2013**, *19*, 1761–1769.
16. Tian, C.; Zhang, Q.; Wu, A.; Jiang, M.; Jiang, B.; Fu, H. Cost-Effective Large-Scale Synthesis of ZnO Photocatalyst with Excellent Performance for Dye Photodegradation. *Chem. Commun.* **2012**, *48*, 2858–2860.
17. Sato, J.; Saito, N.; Nishiyama, H.; Inoue, Y. New Photocatalyst Group for Water Decomposition of RuO<sub>2</sub>-Loaded p-Block Metal (In, Sn, and Sb) Oxides with D10 Configuration. *J. Phys. Chem. B* **2001**, *105*, 6061–6063.
18. Saravanan, R.; Karthikeyan, S.; Gupta, V. K.; Sekaran, G.; Narayanan, V.; Stephen, A. Enhanced Photocatalytic Activity of ZnO/CuO Nanocomposite for the Degradation of Textile Dye on Visible Light Illumination. *Mater. Sci. Eng. C*, **2013**, *33*, 91–98.
19. Mishra, M.; Chun, D.-M. Review-Fe<sub>2</sub>O<sub>3</sub> as a Photocatalytic Material: A Review. *Appl. Catal. A Gen.* **2015**, *498*, 126–141.
20. Momeni, M. M.; Mirhosseini, M; Chavoshi, M; Hakimizade, A. The Effect of Anodizing Voltage on Morphology and Photocatalytic Activity of Tantalum Oxide

- Nanostructure. *J. Mater. Sci. Mater. Electron.* **2016**, *27*, 3941–3947.
21. Lin, Z.; Du, C.; Yan, B.; Wang, C.; Yang, G. Two-Dimensional Amorphous NiO as a Plasmonic Photocatalyst for Solar H<sub>2</sub> Evolution. *Nat. Commun.* **2018**, *9*, 1–11.
  22. Maeda, K.; Teramura, K.; Lu, D.; Saito, N.; Inoue, Y.; Domen, K. Noble-Metal/Cr<sub>2</sub>O<sub>3</sub> Core/Shell Nanoparticles as a Cocatalyst for Photocatalytic Overall Water Splitting. *Angew. Chemie* **2006**, *11*, 7970–7973.
  23. Jing, D.; Guo, L. A Novel Method for the Preparation of a Highly Stable and Active CdS Photocatalyst with a Special Surface Nanostructure. *J. Phys. Chem. B* **2006**, *110*, 11139–11145.
  24. Ye, Z.; Kong, L.; Chen, F.; Chen, Z.; Lin, Y.; Liu, C. A Comparative Study of Photocatalytic Activity of ZnS Photocatalyst for Degradation of Various Dyes. *Optik (Stuttg.)* **2018**, *164*, 345–354.
  25. Parzinger, E.; Miller, B.; Blaschke, B.; Garrido, J. A.; Ager, J. W.; Holleitner, A.; Wurstbauer, U. Photocatalytic Stability of Single- and Few-Layer MoS<sub>2</sub>. *ACS Nano* **2015**, *9*, 11302–11309.
  26. Yu, J.; Xu, C. Y.; Ma, F. X.; Hu, S. P.; Zhang, Y. W.; Zhen, L. Monodisperse SnS<sub>2</sub> Nanosheets for High-Performance Photocatalytic Hydrogen Generation. *ACS Appl. Mater. Interfaces* **2014**, *6*, 22370–22377.
  27. Meng, A.; Zhang, L.; Cheng, B.; Yu, J. Dual Cocatalysts in TiO<sub>2</sub> Photocatalysis. *Adv. Mater.* **2019**, *31*, 1807660.
  28. Guo, Q.; Zhou, C.; Ma, Z.; Yang, X. Fundamentals of TiO<sub>2</sub> Photocatalysis: Concepts, Mechanisms, and Challenges. *Adv. Mater.* **2019**, *31*, 1901997.
  29. Mutuma, B. K.; Shao, N.; Kim, W. D.; Kim, H. T. Sol-Gel Synthesis of Mesoporous Anatase-Brookite and Anatase-Brookite-Rutile TiO<sub>2</sub> Nanoparticles and Their Photocatalytic Properties. *J. Colloid Interface Sci.* **2015**, *442*, 1–7.
  30. Roy, N.; Sohn, Y.; Pradhan, D. Synergy of Low-Energy {101} and High-Energy {001} TiO<sub>2</sub> Crystal Facets for Enhanced Photocatalysis. *ACS Nano* **2013**, *7*, 2532–2540.
  31. Fang, W. Q.; Gong, X.-Q.; Yang, H. G. On the Unusual Properties of Anatase TiO<sub>2</sub> Exposed by Highly Reactive Facets. *J. Phys. Chem. Lett.*, **2011**, *2*, 725–734.
  32. Ma, S.; Song, W.; Liu, B.; Zhong, W.; Deng, J.; Zheng, H.; Liu, J.; Gong, X.-Q.; Zhao, Z. Facet-Dependent Photocatalytic Performance of TiO<sub>2</sub>: A DFT Study. *Appl. Catal. B Environ.* **2016**, *198*, 1–8.
  33. Hashimoto, K.; Irie, H.; Fujishima, A. TiO<sub>2</sub> Photocatalysis: A Historical Overview and Future Prospects. *Jpn J Appl Phys (2008)*. **2005**, *44*, 8269–8285.
  34. Kanan, S.; Moyet, M. A.; Arthur, R. B.; Patterson, H. H. Recent Advances on TiO<sub>2</sub>-Based Photocatalysts toward the Degradation of Pesticides and Major Organic Pollutants from Water Bodies. *Catal Rev Sci Eng.* **2020**, *62*, 1–65.
  35. Linsebigler, A. L.; Lu, G.; Yates, J. T. Photocatalysis on TiO<sub>2</sub> Surfaces: Principles, Mechanisms, and Selected Results. *Chem. Rev.* **1995**, *95*, 735–758.
  36. Schneider, J.; Matsuoka, M.; Takeuchi, M.; Zhang, J.; Horiuchi, Y.; Anpo, M.; Bahnemann, D. W. Understanding TiO<sub>2</sub> Photocatalysis: Mechanisms and Materials. *Chem. Rev.* **2014**, *114*, 9919–9986.
  37. Fujishima, A.; Zhang, X.; Tryk, D. A. TiO<sub>2</sub> Photocatalysis and Related Surface Phenomena. *Surf. Sci. Rep.* **2008**, *63*, 515–582.
  38. Shoneye, A.; Sen Chang, J.; Chong, M. N.; Tang, J. Recent Progress in Photocatalytic Degradation of Chlorinated Phenols and Reduction of Heavy Metal

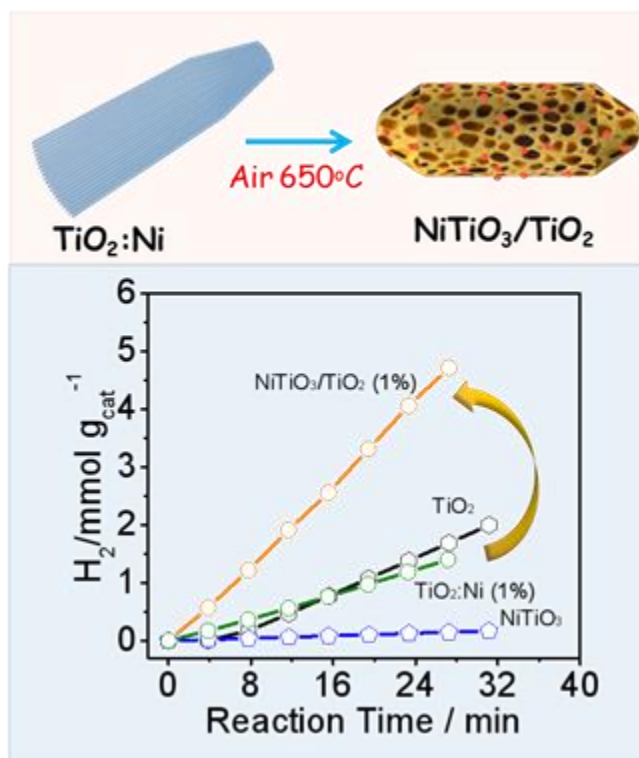
- Ions in Water by TiO<sub>2</sub>-Based Catalysts. *Int. Mater. Rev.* **2021**, 1–18.
39. Zhou, P.; Yu, J.; Jaroniec, M. All-Solid-State Z-Scheme Photocatalytic Systems. *Adv. Mater.* **2014**, *26*, 4920–4935.
  40. Nakata, K.; Ochiai, T.; Murakami, T.; Fujishima, A. Electrochimica Acta Photoenergy Conversion with TiO<sub>2</sub> Photocatalysis: New Materials and Recent Applications. *Electrochim. Acta* **2012**, *84*, 103–111.
  41. Etacheri, V.; Di Valentin, C.; Schneider, J.; Bahnemann, D.; Pillai, S. C. Visible-light activation of TiO<sub>2</sub> photocatalysts: Advances in theory and experiments. *J. Photochem. Photobiol. C* **2015**, *25*, 1–29.
  42. Fujishima, A.; Honda, K. Electrochemical Photolysis of Water at a Semiconductor Electrode. *Nature* **1972**, *238*, 37–38.
  43. Khan, J. A.; Sayed, M.; Shah, N. S.; Khan, S.; Zhang, Y.; Boczkaj, G.; Khan, H. M.; Dionysiou, D. D. Synthesis of Eosin Modified TiO<sub>2</sub> Film with Co-Exposed {001} and {101} Facets for Photocatalytic Degradation of Para-Aminobenzoic Acid and Solar H<sub>2</sub> Production. **2020**, *265*, 118557.
  44. Girish Kumar, S.; Gomathi Devi, L. Review on Modified TiO<sub>2</sub> Photocatalysis under UV/Visible Light: Selected Results and Related Mechanisms on Interfacial Charge Carrier Transfer Dynamics. *J. Phys. Chem. A* **2011**, *115*, 12.
  45. Ola, O.; Maroto-Valer, M. M. Review of Material Design and Reactor Engineering on TiO<sub>2</sub> Photocatalysis for CO<sub>2</sub> Reduction. *J. Photochem. Photobiol. C* **2015**, *24*, 16–42.
  46. Konstantinou, I. K.; Albanis, T. A. TiO<sub>2</sub>-Assisted Photocatalytic Degradation of Azo Dyes in Aqueous Solution: Kinetic and Mechanistic Investigations A Review. *Appl. Catal. B* **2004**, *49*, 1–14.
  47. Meng, X.; Cui, X.; Rajan, N. P.; Yu, L.; Deng, D.; Bao, X. Direct Methane Conversion under Mild Condition by Thermo-, Electro-, or Photocatalysis. *Chem.* **2019**, *5*, 2296–2325.
  48. Ahmed, S. N.; Haider, W. Heterogeneous Photocatalysis and Its Potential Applications in Water and Wastewater Treatment: A Review. *Nanotechnology. Nanotechnology*, **2018**, *29*, 342001.
  49. Bahnemann, D. Photocatalytic Water Treatment: Solar Energy Applications. *Sol Energy*, **2004**, *77*, 445–459.
  50. Wang, C.-C.; Zhang, Z.; Ying, J. Y. Photocatalytic Decomposition of Halogenated Organics over Nanocrystalline Titania. *Nanostructured Materials*, **1997**, *9*, 583–586.
  51. Wang, H.; Zhang, L.; Chen, Z.; Hu, J.; Li, S.; Wang, Z.; Liu, J.; Wang, X. Semiconductor Heterojunction Photocatalysts: Design, Construction, and Photocatalytic Performances. *Chem. Soc. Rev.* **2014**, *43*, 5234–5244.
  52. Khalid, N. R.; Majid, A.; Bilal Tahir, M.; Niaz, N. A.; Khalid, S. Carbonaceous-TiO<sub>2</sub> Nanomaterials for Photocatalytic Degradation of Pollutants: A Review. *Ceram. Int.* **2017**, *43*, 14552–14571.
  53. Ochiai, T.; Fujishima, A. Photoelectrochemical Properties of TiO<sub>2</sub> Photocatalyst and Its Applications for Environmental Purification. *J. Photochem. Photobiol. C Photochem. Rev.* **2012**, *13*, 247–262.
  54. Xu, Q.; Zhang, L.; Yu, J.; Wageh, S.; Al-Ghamdi, A. A.; Jaroniec, M. Direct Z-Scheme Photocatalysts: Principles, Synthesis, and Applications. *Mater. Today*. **2018**, *21*,

- 1042–1063.
55. Serpone, N. Photocatalysis. *Kirk-Othmer Encyclopedia of Chemical Technology*. **2000**.
  56. Wenderich, K.; Mul, G. Methods, Mechanism, and Applications of Photodeposition in Photocatalysis: A Review. *Chem. Rev.* **2016**, *116*, 14587–14619.
  57. Singh, R.; Dutta, S. A Review on H<sub>2</sub> Production through Photocatalytic Reactions Using TiO<sub>2</sub>/TiO<sub>2</sub>-Assisted Catalysts. *Fuel*, **2018**, *220*, 607–620.
  58. Meng, X.; Ouyang, S.; Kako, T.; Li, P.; Yu, Q.; Wang, T.; Ye, J. Photocatalytic CO<sub>2</sub> Conversion over Alkali Modified TiO<sub>2</sub> without Loading Noble Metal Cocatalyst. *Chem. Commun.* **2014**, *50*, 11517–11519.
  59. Yong, X.; Schoonen, M. A. A. The Absolute Energy Positions of Conduction and Valence Bands of Selected Semiconducting Minerals. *Am. Mineral.* **2000**, *85*, 543–556.
  60. Wang, J.; Tafen, D. N.; Lewis, J. P.; Hong, Z.; Manivannan, A.; Zhi, M.; Li, M.; Wu, N. Origin of Photocatalytic Activity of Nitrogen-Doped TiO<sub>2</sub> Nanobelts. *J. Am. Chem. Soc.* **2009**, *131*, 12290–12297.
  61. Xie, Y. P.; Liu, G.; Yin, L.; Cheng, H. M. Crystal Facet-Dependent Photocatalytic Oxidation and Reduction Reactivity of Monoclinic WO<sub>3</sub> for Solar Energy Conversion. *J. Mater. Chem.* **2012**, *22*, 6746–6751.
  62. Shang, J.; Hao, W.; Lv, X.; Wang, T.; Wang, X.; Du, Y.; Dou, S.; Xie, T.; Wang, D.; Wang, J. Bismuth Oxybromide with Reasonable Photocatalytic Reduction Activity under Visible Light. *ACS Catal.* **2014**, *4*, 954–961.
  63. Matsuoka, M.; Kitano, M.; Takeuchi, M.; Tsujimaru, K.; Anpo, M.; Thomas, J. M. Photocatalysis for New Energy Production Recent Advances in Photocatalytic Water Splitting Reactions for Hydrogen Production. *Catal. Today*, **2007**, *122*, 51–61.
  64. Sayama, K.; Arakawa, H. Photocatalytic Decomposition of Water and Photocatalytic Reduction of Carbon Dioxide over ZrO<sub>2</sub> Catalyst. *J. Phys. Chem.* **1993**, *97*, 531–533.
  65. Cushing, S. K.; Li, J.; Meng, F.; Senty, T. R.; Suri, S.; Zhi, M.; Li, M.; Bristow, A. D.; Wu, N. Photocatalytic Activity Enhanced by Plasmonic Resonant Energy Transfer from Metal to Semiconductor. *J. Am. Chem. Soc.* **2012**, *134*, 51.
  66. Marschall, R.; Marschall, R. Semiconductor Composites: Strategies for Enhancing Charge Carrier Separation to Improve Photocatalytic Activity. *Adv. Funct. Mater.* **2014**, *24*, 2421–2440.
  67. Maeda, K.; Xiong, A.; Yoshinaga, T.; Ikeda, T.; Sakamoto, N.; Hisatomi, T.; Takashima, M.; Lu, D.; Kanehara, M.; Setoyama, T.; Teranishi, T.; Domen, K. Photocatalytic Overall Water Splitting Promoted by Two Different Cocatalysts for Hydrogen and Oxygen Evolution under Visible Light. *Angew. Chemie* **2010**, *122*, 4190–4193.
  68. Yin Tee, S.; Yin Win, K.; Siang Teo, W.; Koh, L.-D.; Liu, S.; Peng Teng, C.; Han, M.-Y.; Tee, S. Y.; Win, K. Y.; Koh, L.; Liu, S.; Teng, C. P.; Han, M.; Teo, W. S. Recent Progress in Energy-Driven Water Splitting. *Adv. Sci.*, **2017**, *4*, 1600337.
  69. Tang, J.; Durrant, J. R.; Klug, D. R. Mechanism of Photocatalytic Water Splitting in TiO<sub>2</sub>. Reaction of Water with Photoholes, Importance of Charge Carrier Dynamics, and Evidence for Four-Hole Chemistry. *J. Am. Chem. Soc.* **2008**, *130*, 13885–13891.

70. Maeda, K.; Domen, K. Photocatalytic Water Splitting: Recent Progress and Future Challenges. *J. Phys. Chem. Lett.* **2010**, *1*, 2655–2661.
71. Haider, Z.; Kang, Y. S. Facile Preparation of Hierarchical TiO<sub>2</sub> Nano Structures: Growth Mechanism and Enhanced Photocatalytic H<sub>2</sub> Production from Water Splitting Using Methanol as a Sacrificial Reagent. *ACS Appl. Mater. Interfaces* **2014**, *6*, 10342–10352.
72. Zhang, P.; Wang, T.; Chang, X.; Gong, J. Effective Charge Carrier Utilization in Photocatalytic Conversions. *Acc. Chem. Res.* **2016**, *49*, 911–921.
73. Nakhate, G.G.; Nikam, V.S.; Kanade, K.G.; Arbuj, S.; Kale, B.B.; Baeg, J.O. Hydrothermally Derived Nanosized Ni-doped TiO<sub>2</sub>: A Visible Light Driven Photocatalyst for Methylene Blue Degradation. *Mater. Chem. Phys.* **2010**, *124*, 976–981.
74. Dong, Z.; Ding, D.; Li, T.; Ning, C. Ni-doped TiO<sub>2</sub> Nanotubes Photoanode for Enhanced Photoelectrochemical Water Splitting. *Appl. Surf. Sci.* **2018**, *443*, 321–328.
75. Sarkar, N.; Ghosh, S.K.; Bannerjee, S.; Aikat, K. Bioethanol Production from Agricultural Wastes: An Overview. *Renew. Energ.* **2012**, *37*, 19–27.
76. Zayed, H.; Sahu, J.N.; Suely, A.; Boyce, A.N.; Faruq, G. Bioethanol Production from Renewable Sources: Current Perspectives and Technological Progress. *Renew. Sustain. Energ. Rev.* **2017**, *71*, 475–501.
77. Rulkens, W. Sewage Sludge as a Biomass Resource for the Production of Energy: Overview and Assessment of the Various Options. *Energy Fuels* **2008**, *22*, 9–15.
78. Puga, A. V Photocatalytic Production of Hydrogen from Biomass-Derived Feedstocks. *Coord. Chem. Rev.* **2016**, *315*, 1–66.
79. Ying Toe, C.; Tsounis, C.; Zhang, J.; Masood, H.; Gunawan, D.; Scott, J.; Amal, R. Advancing Photoreforming of Organics: Highlights on Photocatalyst and System Designs for Selective Oxidation Reactions. *Energy Environ. Sci.* **2021**, *14*, 1140.
80. Ampelli, C.; Passalacqua, R.; Genovese, C.; Perathoner, S.; Centi, G.; Montini, T.; Gombac, V.; Delgado Jaen, J.J.; Fornasiero, P. H<sub>2</sub> Production by Selective Photo-Dehydrogenation of Ethanol in Gas and Liquid Phase on CuO<sub>x</sub>/TiO<sub>2</sub> Nanocomposites. *RSC Adv.* **2013**, *3*, 21776–21788.
81. Zhang, X.; Luo, L.; Yun, R.; Pu, M.; Zhang, B.; Xiang, X., Increasing the Activity and Selectivity of TiO<sub>2</sub>-Supported Au Catalysts for Renewable Hydrogen Generation from Ethanol Photoreforming by Engineering Ti<sup>3+</sup> Defects. *ACS Sustain. Chem. Eng.* **2019**, *7*, 13856–13864.
82. enieks, U.; Balodite, E.; Strähler, S.; Strazdina, I.; Rex, J.; Pentjuss, A.; Fuchino, K.; Bruheim, P.; Rutkis, R.; Pappas, K. M., Improvement of acetaldehyde production in *Zygomonas mobilis* by engineering of its aerobic metabolism. *Front. Microbiol.* **2019**, *10*, 2533.
83. Danner, H.; Braun, R., Biotechnology for the production of commodity chemicals from biomass. *Chem. Soc. Rev.* **1999**, *28*, 395–405.
84. Moore, C. M.; Staples, O.; Jenkins, R. W.; Brooks, T. J.; Semelsberger, T. A.; Sutton, A. D., Acetaldehyde as an ethanol derived bio-building block: an alternative to Guerbet chemistry. *Green Chem.* **2017**, *19*, 169–174.
85. Li, H.; Zhou, Y.; Tu, W.; Ye, J.; Zou, Z. State-of-the-Art Progress in Diverse Heterostructured Photocatalysts toward Promoting Photocatalytic Performance.

- Adv. Funct. Mater.* **2015**, *25*, 998–1013.
86. Zhang, L.; Jaroniec, M. Toward Designing Semiconductor-Semiconductor Heterojunctions for Photocatalytic Applications. *Appl. Surf. Sci.* **2018**, *430*, 2–17.
  87. Xing, C.; Zhang, Y.; Liu, Y.; Wang, X.; Li, J.; Martínez-Alanis, P. R.; Spadaro, M. C.; Guardia, P.; Arbiol, J.; Llorca, J.; Cabot, A. Photodehydrogenation of ethanol over Cu<sub>2</sub>O/TiO<sub>2</sub> heterostructures. *Nanomaterials* **2021**, *11*, 1399.
  88. Low, J.; Jiang, C.; Cheng, B.; Wageh, S.; Al-Ghamdi, A. A.; Yu, J. A Review of Direct Z-Scheme Photocatalysts. *Small Methods*. **2017**, *1*, 1700080.
  89. Yu, J.; Wang, S.; Low, J.; Xiao, W. Enhanced photocatalytic performance of direct Z-scheme gC<sub>3</sub>N<sub>4</sub>-TiO<sub>2</sub> photocatalysts for the decomposition of formaldehyde in air. *Phys. Chem. Chem. Phys* **2013**, *15*, 16883.
  90. Wahi, R. K.; Liu, Y.; Falkner, J. C.; Colvin, V. L. Solvothermal Synthesis and Characterization of Anatase TiO<sub>2</sub> Nanocrystals with Ultrahigh Surface Area. *J. Colloid Interface Sci.* **2006**, *302*, 530–536.
  91. Akpan, U. G.; Hameed, B. H. The Advancements in Sol-Gel Method of Doped-TiO<sub>2</sub> Photocatalysts. *Appl. Catal. A-gen*, **2010**, *375*, 1–11.
  92. T.R. Gordon, M. Cargnello, T. Paik, F. Mangolini, R.T. Weber, P. Fornasiero, C.B. Murray, Nonaqueous synthesis of TiO<sub>2</sub> nanocrystals using TiF<sub>4</sub> to engineer morphology, oxygen vacancy concentration, and photocatalytic activity, *J. Am. Chem. Soc.* **2012**, *134*, 6751–6761.
  93. Walton, R. I. Subcritical Solvothermal Synthesis of Condensed Inorganic Materials. *Chem. Soc. Rev.* **2002**, *31*, 230–238.
  94. Hench, L. L.; West, J. K. *The Sol-Gel Process. Chem. Rev.*, **1990**, *90*, 33–72.
  95. Biswas, A.; Chakraborty, A.; Jana, N. R. Nitrogen and Fluorine Codoped, Colloidal TiO<sub>2</sub> Nanoparticle: Tunable Doping, Large Red-Shifted Band Edge, Visible Light Induced Photocatalysis, and Cell Death. *ACS Appl. Mater. Interfaces* **2018**, *10*, 1976–1986.
  96. Zhang, Z.; Wu, Q.; Johnson, G.; Ye, Y.; Li, X.; Li, N.; Cui, M.; Lee, J. D.; Liu, C.; Zhao, S.; Li, S.; Orlov, A.; Murray, C. B.; Zhang, X.; Gunnoe, T. B.; Su, D.; Zhang, S. A Generalized Synthetic Strategy for Transition Metal Doped Brookite-Phase TiO<sub>2</sub> Nanorods. *J. Am. Chem. Soc.* **2019**, *141*, 16548–16552.

## Chapter 2 Porous NiTiO<sub>3</sub>/TiO<sub>2</sub> nanostructures for photocatalytic hydrogen evolution



### 2.1 Abstract

We present a strategy to produce porous NiTiO<sub>3</sub>/TiO<sub>2</sub> nanostructures with excellent photocatalytic activity toward hydrogen generation. In a first step, nickel-doped TiO<sub>2</sub> needle bundles were synthesized by a hydrothermal procedure. Through the sintering in air of these nanostructures, porous NiTiO<sub>3</sub>/TiO<sub>2</sub> heterostructured rods were obtained. Alternatively, the annealing in argon of the nickel-doped TiO<sub>2</sub> needle bundles resulted in NiO<sub>x</sub>/TiO<sub>2</sub> elongated nanostructures. Porous NiTiO<sub>3</sub>/TiO<sub>2</sub> structures were tested for hydrogen evolution in the presence of ethanol. Such porous heterostructures exhibited superior photocatalytic activity toward hydrogen generation, with hydrogen production rates up to 11.5 mmol h<sup>-1</sup> g<sup>-1</sup> at room temperature. This excellent performance is related here to the optoelectronic properties and geometric parameters of the material.

## 2.2 Introduction

Since first reports on photocatalytic water splitting, TiO<sub>2</sub> has been considered one of the most attractive photocatalysts.<sup>1-3</sup> Among others, its interest resides on its excellent optoelectronic properties, high resistance to photocorrosion, natural abundance, low-cost and safety.<sup>4-6</sup> However, TiO<sub>2</sub> optimization for solar photocatalysis requires maximizing its surface area.<sup>7</sup> It also requires the introduction of dopants, additional phases or structural defects that allow this wide band gap semiconductor to take advantage of a larger spectral range of the solar radiation.<sup>8-13</sup>

To maximize surface area, the production of hollow and porous TiO<sub>2</sub> nanostructures has recently drawn growing attention.<sup>14-16</sup> Besides, Ti-based mixed oxides and particularly perovskite titanates MTiO<sub>3</sub> (M=Ba, Sr, Ca and Ni) have been pointed out as a new exciting class of photoactive materials.<sup>17-19</sup> Additionally heterostructured oxides, such as SrTiO<sub>3</sub>/TiO<sub>2</sub> and NiTiO<sub>3</sub>/TiO<sub>2</sub> have been demonstrated to promote charge-separation, hole-transportation and visible-light-driven photocatalytic performance over TiO<sub>2</sub>.<sup>20-23</sup>

To cite some examples in this direction, Wu et al. demonstrated an enhancement of the charge separation and hole transportation in TiO<sub>2</sub>/SrTiO<sub>3</sub> nano-heterostructures to be at the origin of an improved photoelectrochemical performance<sup>20</sup>. When combined with TiO<sub>2</sub>, several other oxides and chalcogenides have demonstrated to be able to enhance its photocatalytic activities.<sup>23-26</sup> In particular, Ni-based materials have been proven especially effective to improve TiO<sub>2</sub> photocatalytic activity. Rawool et al. demonstrated *pn* heterojunctions in NiO/TiO<sub>2</sub> produced by sol gel to promote photocatalytic H<sub>2</sub> generation.<sup>27</sup> Wei et al. showed Ni(HCO<sub>3</sub>)<sub>2</sub> produced through a hydrothermal method to be an excellent co-catalyst to boost photocatalytic hydrogen evolution of mesoporous TiO<sub>2</sub>.<sup>28</sup> Enhanced photocatalytic H<sub>2</sub> production was also reported with the introduction of Ni(OH)<sub>2</sub> clusters to commercially available TiO<sub>2</sub><sup>29</sup> and in Ni/NiO/N-TiO<sub>2-x</sub> heterostructures produced from a NH<sub>3</sub> plasma treatment of sol-gel derived Ti-Ni precursors.<sup>30</sup> Besides, Qu et al. prepared porous NiTiO<sub>3</sub> nanorods with enhanced photocatalytic performance toward the degradation of nitrobenzene.<sup>21</sup>

While excellent results have been obtained to date, the synthesis of such mixed oxides

and oxide heterostructures in the form of high surface area materials is extremely challenging, what has limited further advances in this direction.<sup>31-33</sup>

To overcome this severe challenge, we present here a simple, high throughput and scalable hydrothermal-based strategy to produce porous NiTiO<sub>3</sub>/TiO<sub>2</sub> heterostructures. This strategy is based on the synthesis of needle bundles of Ni-doped TiO<sub>2</sub> (TiO<sub>2</sub>:Ni) and their posterior sintering in air to produce highly crystalline NiTiO<sub>3</sub>/TiO<sub>2</sub> heterostructures with a significant level of porosity reminiscent of the large density of interfaces within the needle bundles. We further demonstrate here that these preliminarily optimized materials are excellent photocatalysts for hydrogen generation. We choose hydrogen generation as test reaction owing to the excellent performances of Ni-based photocatalysts previously reported.<sup>27-30,34-36</sup>

## 2.3 Experimental Section

### Chemicals

Titanium(IV) isopropoxide (97%, Sigma-Aldrich), nickel(II) nitrate hexahydrate (98%, Fluka), ethanol (96%, PanReac AppliChem), hexadecylamine (HDA, 90%, Sigma-Aldrich), potassium chloride (Sigma-Aldrich), and ammonium hydroxide solution (28-30%, Sigma-Aldrich) were used without further purification.

### Synthesis of NiTiO<sub>3</sub>/TiO<sub>2</sub> Heterostructures

A solution of KCl (1.9 mg) in miliQ water (0.99 g) was added dropwise to a HDA (0.45 g) solution in ethanol (20 mL) under stirring at room temperature. To this solution, a proper amount of Ni(NO<sub>3</sub>)<sub>2</sub>·6H<sub>2</sub>O was added (0 mg, 22.5 mg, 45 mg, 90 mg, and 225 mg to reach 0, 0.5, 1, 2, and 5 mol% concentrations, respectively). Then, 4.7 mL of titanium(IV) isopropoxide was added. After stirring for 1 h at room temperature, we kept the solution 16 h without stirring, and afterward the solution was washed with ethanol three times using centrifugation to recover the product. This product was then dissolved in a solution containing 20 mL of MiliQ water, 40 mL of ethanol and 2.2 mL of ammonium hydroxide. This solution was stirred for 1 h and it was subsequently transferred to a 100mL Teflon-lined hydrothermal reactor. The reactor was heated at 170 °C and maintained at this temperature for 17 h. Afterward, it was cooled down to

room temperature and the product was washed three times with ethanol. Dried materials were finally annealed in a tube furnace under synthetic air flow at 650 °C for 8 h.

### **Characterization**

X-ray diffraction analyses (XRD,  $2\theta$ : 20°-80°; scanning rate: 5°/min) were carried out on a Bruker AXS D8 Advance X-ray diffractometer with Ni-filtered Cu-K $\alpha$  radiation ( $\lambda$ = 0.15406 Å), operating at 40 mA and 40 kV. The morphology and size of the particles were characterized by transmission electron microscopy (TEM, ZEISS LIBRA 120), working at 120 kV and field-emission scanning electron microscopy (SEM, Zeiss Auriga) operating at 5.0 kV. High resolution transmission electron microscopy (HRTEM) images and scanning transmission electron microscopy (STEM) studies were conducted on a FEI Tecnai F20 field emission gun microscope operated at 200 kV with a point-to-point resolution of 0.19 nm, which was equipped with high angle annular dark field (HAADF) and a Gatan Quantum electron energy loss spectroscopy (EELS)

detectors. Elemental analysis was carried out using an Oxford energy dispersive X-ray spectrometer (EDX) combined with the Zeiss Auriga SEM working at 20.0 kV. X-ray photoelectron spectroscopy (XPS) was examined on a SPECS system equipped with a Phoibos 150 MCD-9 detector, working at 150 mW with an Al anode XR50 source. Fourier transform infrared spectroscopy (FTIR, Alpha Bruker) was carried with a platinum attenuated total reflectance single reflection module. Nitrogen sorption measurements were collected on a MicroActive 3.00 at 77.3 K.

### **Photocatalytic Hydrogen Evolution Tests**

In a typical experiment, a cellulose paper impregnated with 2.0 mg of the photocatalyst was placed inside a photocatalytic reactor that was equipped with a UV LED (Figure 1). An Ar gas stream was saturated with a water:ethanol vapour mixture (90:10 ratio on a molar basis) by bubbling dry Ar gas at a flow rate of 20 mL·min<sup>-1</sup> through a saturator (Dreschel bottle) containing a liquid mixture of 87.5 g of H<sub>2</sub>O and 9.92 g of ethanol.<sup>37,38</sup> This Ar stream was introduced into the photoreactor and passed through the cellulose paper loaded with the photocatalyst. The photoreactor effluent

was monitored on-line every 4 min using gas chromatography (GC) (Agilent 3000A MicroGC) using three columns: MS 5 Å, Plot U and Stabilwax. The LED UV light source (from SACOPA, S.A.U.) consisted of four LEDs at  $365 \pm 5$  nm and a synthetic quartz glass cylindrical lens that transmitted the light to the photocatalyst. Light irradiation was measured directly with a UV-A radiation monitor from Solar Light Co. and was  $79.1 \pm 0.5$  mW·cm<sup>-2</sup> at the sample position. At the beginning of each experiment, the UV light was off, and the reaction system was purged by entering 20 mL·min<sup>-1</sup> of saturated Ar gas with the water-ethanol vapour mixture, to remove oxygen in the line. After 30 min, the UV light was turned on and we monitored all photoreaction products during ca. 20-40 min by GC. Control experiments were carried out with only the cellulose paper support and no photoactivity was measured.

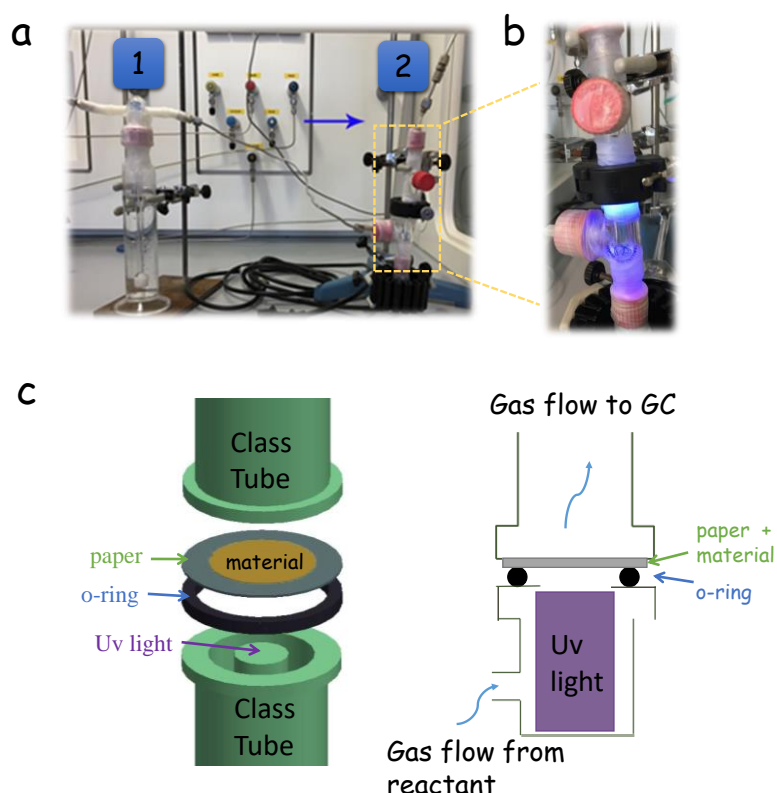


**Figure 1.** (a) Photograph of the system used to test the photocatalytic hydrogen generation: 1 displays the Dreschel bottle containing the ethanol-water solution (1:9 molar). 2 displays the actual photoreactor. (b) Scheme of the photoreactor.

### Electrochemical Impedance Spectroscopy (EIS)

EIS analyses were performed using a Bio-Logic SP-300 potentiostat in a 3-electrode configuration employing a Cappuccino-type PEC cell, wherein the photocatalyst was

deposited as a thin film in a conductive substrate (FTO) to be used as working electrode, whereas a Ag/AgCl electrode and a Pt wired were used as a reference and a counter electrode, respectively. The applied potential on the working electrode was sinusoidally modulated with an amplitude of 25 mV using frequencies ranging from 100 kHz to 50 mHz. The analysis of the impedance response was undertaken using ZView (Scribner Associates).

The apparent quantum yield (AQY) was estimated using the following equation:

$$AQY = \frac{2n_{H_2}}{n_p} \cdot 100 = \frac{nN_A}{E_T/E_p} \cdot 100$$

where  $n_{H_2}$  is the number of molecules of  $H_2$  generated and  $n_p$  is the number of incident photons reaching the catalyst. The number of incident photons can be calculated by  $n_p = E_T/E_p$ , where  $E_T$  is the total energy reaching the catalyst and  $E_p$  is the energy of a photon.  $E_T = PSt$ , where  $P$  ( $W \cdot m^{-2}$ ) is the power density of the incident monochromatic light,  $S$  ( $m^2$ ) is the irradiation area and  $t$  (s) is the duration of the incident light exposure.  $E_p = hc/\lambda$ , where  $h$  is the Planck's constant,  $c$  the speed of light and  $\lambda$  (m) is the wavelength of the incident monochromatic light. The number of hydrogen molecules can be calculated as  $n_{H_2} = nN_A$ , where  $n$  are  $H_2$  moles evolved during the time of light exposure ( $t$ ), and  $N_A$  is the Avogadro constant.<sup>39-41</sup> In our experimental conditions, the wavelength of the incident light was  $\lambda = 365$  nm, the power density of the incident light at the paper surface was  $P = 79.1 mW \cdot cm^{-2}$  and the irradiation area was  $S = 2.27$   $cm^2$ .

## 2.4 Results and discussion

### Characterization of the Photocatalysts

Ni-doped  $TiO_2$  ( $TiO_2:Ni$ ) nanostructures were produced from the hydrothermal decomposition of titanium(IV) isopropoxide in the presence of proper amounts of nickel(II) nitrate hexahydrate, HDA as a shape-directing agent and KCl to control the ionic strength of the solution (see experimental section for details and Figure 2 for SEM images).<sup>42</sup> As shown by TEM characterization, the size and shape of the

nanostructures obtained from this hydrothermal reaction strongly depended on the amount of Ni introduced (Figure 3). In the absence of Ni, nanoparticles with an average size around 50 nm and mostly irregular shapes, although some elongated, were obtained. When introducing increasingly higher amounts of Ni, more and more elongated nanostructures were obtained. In the presence of a nominal 5% of Ni, most structures resembled nanorods with a length in the range from 100 nm to 200 nm and thickness of 30-60 nm (Figures 4b, 4b and 3). A closer look to these nanorods allowed discerning that they consisted of needle-shaped nanostructures assembled in bundles (Figure 5b).

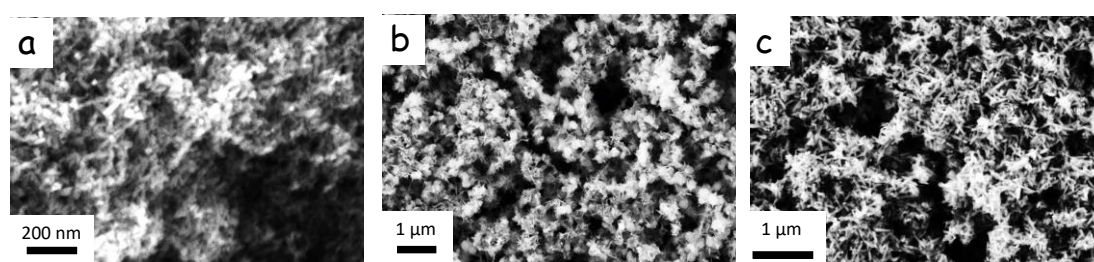


**Figure 2.** SEM images of TiO<sub>2</sub>:Ni (5%) produced in the following conditions: (a) without HDA, (b) without H<sub>2</sub>O, (c) in HDA-H<sub>2</sub>O-KCl.

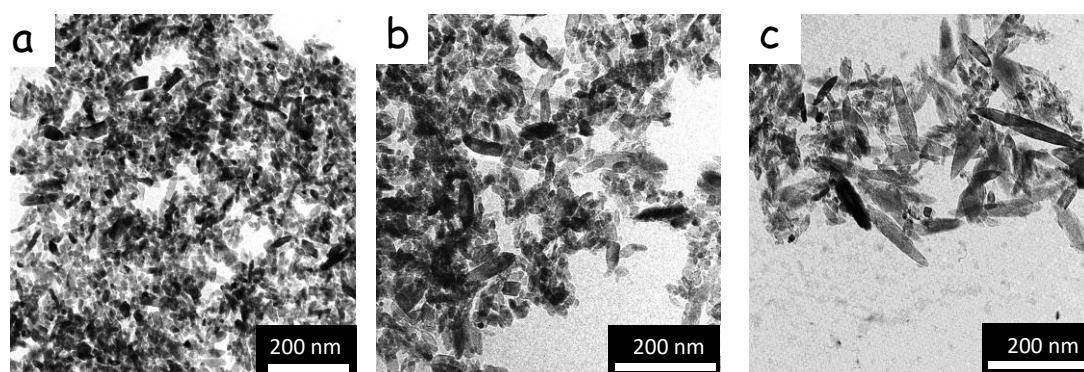


**Figure 3.** TEM images of (a) TiO<sub>2</sub>, (b) TiO<sub>2</sub>:Ni (1%), (c) TiO<sub>2</sub>:Ni (2%).

XRD analyses showed the crystal structure of these needle bundles to match that of anatase TiO<sub>2</sub>. Diffraction peaks shifted to lower angles with the introduction of increasing amounts of Ni (Figure 1a), which pointed at the presence of Ni ions within the TiO<sub>2</sub> anatase lattice. Besides anatase TiO<sub>2</sub>, no additional crystallographic phase

could be discerned from XRD patterns. EDX analysis showed the Ni atomic concentration to be systematically higher than the nominal amount introduced, pointing at a higher yield of reaction of the nickel(II) nitrate than the titanium(IV) isopropoxide under the hydrothermal conditions used for the synthesis (Table 1).

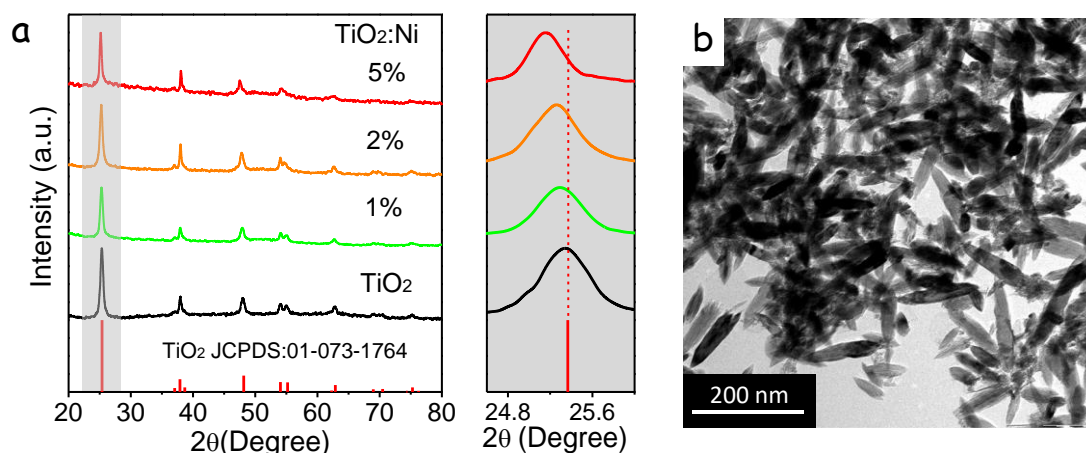


**Figure 4.** (a) XRD patterns of TiO<sub>2</sub> and TiO<sub>2</sub>:Ni (1%, 2%, 5%) nanopowders. (b) TEM image of TiO<sub>2</sub>:Ni (5%) nanopowder.

**Table 1.** Ti and Ni atomic concentrations of TiO<sub>2</sub>, TiO<sub>2</sub>:Ni (1%, 2%, 5%) and NiTiO<sub>3</sub>/TiO<sub>2</sub> (1%, 2%, 5%).

catalysts	EDX		XRD		XPS	
	Ti (atom%)	Ni (atom%)	Ti (atom%)	Ni (atom%)	Ti (atom%)	Ni (atom%)
TiO <sub>2</sub>	100					
TiO <sub>2</sub> :Ni (1%)	96.4	3.6			94.3	5.7
TiO <sub>2</sub> :Ni (2%)	93.6	6.4				
TiO <sub>2</sub> :Ni (5%)	83.2	16.8				
NiTiO <sub>3</sub> /TiO <sub>2</sub> (1%)	96.4	3.6	4.4	95.6	94.2	5.8
NiTiO <sub>3</sub> /TiO <sub>2</sub> (2%)	94.3	5.7	6.5	93.5		
NiTiO <sub>3</sub> /TiO <sub>2</sub> (5%)	86	14	13.3	86.7		
NiTiO <sub>3</sub>	61.9	39.1				

TiO<sub>2</sub>:Ni nanopowders were annealed under synthetic air flow at 650 °C during 8 h. Upon this thermal treatment, the color of the material changed from the original blueish, characterizing TiO<sub>2</sub>:Ni samples, to yellow (Figure 6). TEM micrographs of the

annealed powder showed it to still consist on elongated nanostructures. However, on the contrary to the starting nanoneedle bundles, the annealed nanostructures displayed a crystallographic continuity (Figure 5c). Additionally, the annealed nanostructures presented numerous holes all over them (Figure 5d). In contrast, the annealing of undoped TiO<sub>2</sub> nanopowders in the same conditions did not result in such porous structure (Figure 7).

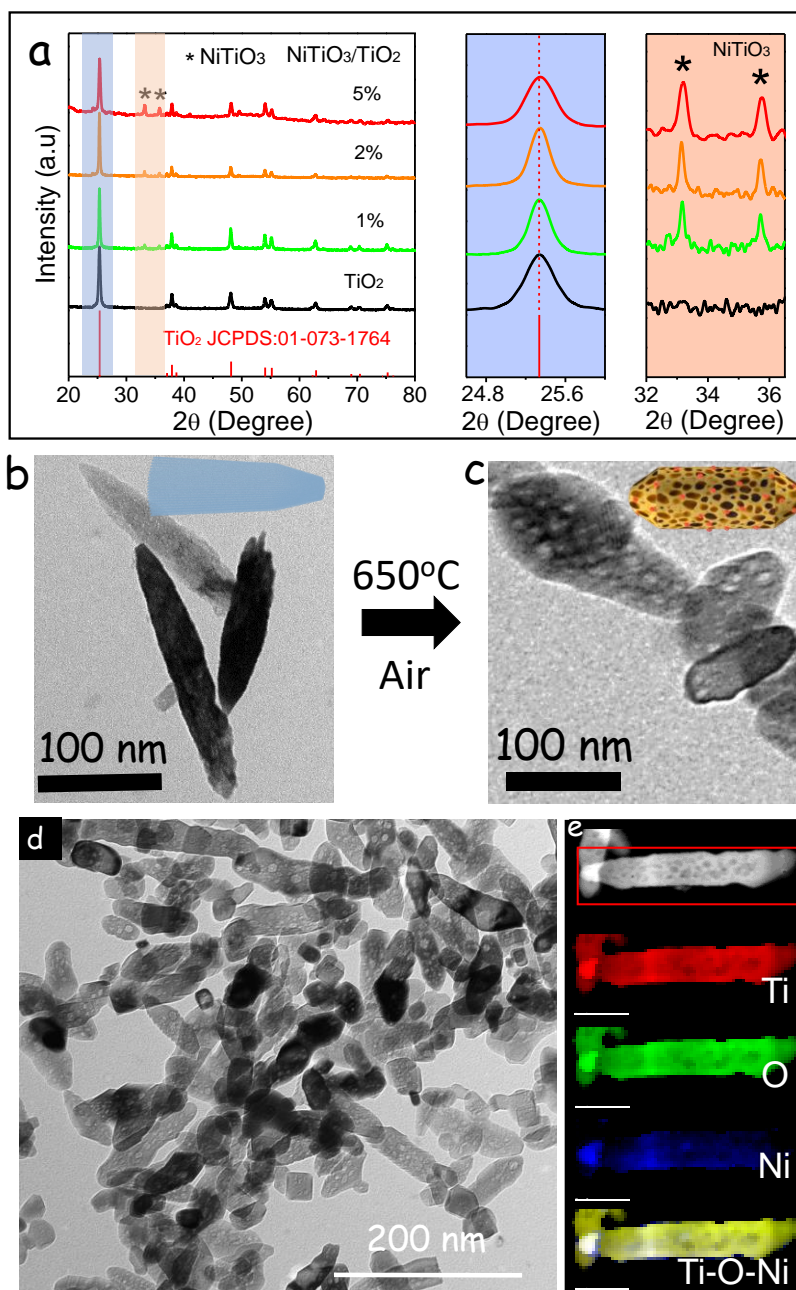


**Figure 5.** (a) XRD patterns of NiTiO<sub>3</sub>/TiO<sub>2</sub> (0, 1%, 2%, 5%) nanopowders obtained after annealing in air. (b) TEM micrograph of TiO<sub>2</sub>:Ni (5%) needle bundles. (c, d) TEM

micrographs of NiTiO<sub>3</sub>/TiO<sub>2</sub> (5%) porous structures obtained after annealing in air. (e) HAADF micrograph of a NiTiO<sub>3</sub>/TiO<sub>2</sub> (5%) rod and corresponding EELS elemental maps for Ti, O, Ni and Ti-O-Ni.

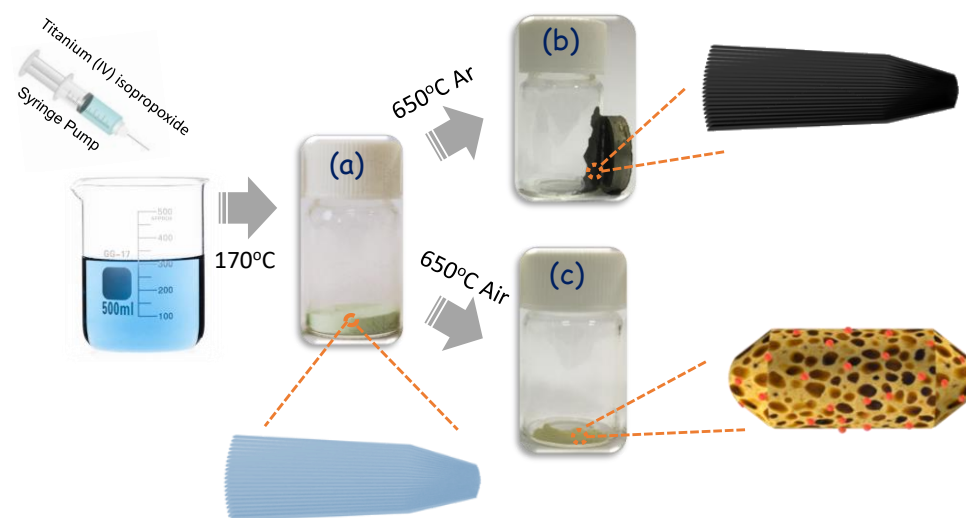


**Figure 6.** Scheme of the TiO<sub>2</sub>:Ni precursor preparation procedure: (a) TiO<sub>2</sub>:Ni, (b) NiO<sub>x</sub>/TiO<sub>2</sub>, (c) NiTiO<sub>3</sub>/TiO<sub>2</sub>.

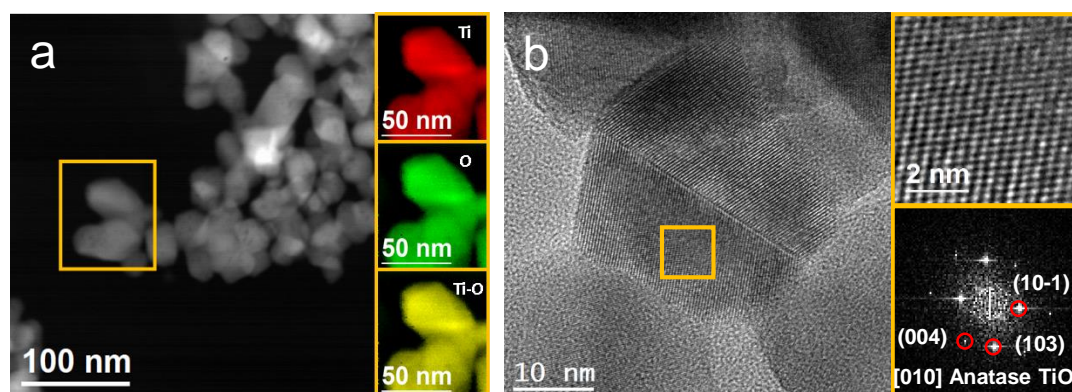


**Figure 7.** TiO<sub>2</sub> annealing at 650 °C in air: (a) STEM micrograph and EELS chemical composition maps obtained from the yellow squared area of the STEM micrograph. Individual Ti L<sub>2,3</sub>-edges at 456 eV (red) and O K-edge at 532 eV (green) as well as its composite. (b) HRTEM micrograph, detail of the yellow squared region and its corresponding power spectrum.

XRD analysis showed that the porous nanostructures obtained after the annealing of TiO<sub>2</sub>:Ni in air consisted mainly on anatase TiO<sub>2</sub> (Figure 5a, 8a). With the annealing process, the shift of the XRD peaks observed in the precursor TiO<sub>2</sub>:Ni material disappeared, pointing at the outward diffusion of the Ni ions from the TiO<sub>2</sub> lattice. Besides the anatase phase, XRD patterns displayed the presence of a second crystal

structure, which was identified as NiTiO<sub>3</sub>.<sup>43</sup> The relative intensity of the peaks associated to this NiTiO<sub>3</sub> phase clearly increased with the nominal amount of Ni (Figure 5a). Rietveld analysis showed the relative amount of the NiTiO<sub>3</sub> phase to correspond to a 4.6 mol%, 9.0 mol% and 15 mol%, for samples obtained from nominal Ni concentration of 1 mol%, 2 mol% and 5 mol%, respectively (Figure 8b).<sup>44</sup> Within its experimental error, EDX analysis showed the Ni molar concentrations to be maintained after the annealing process (Table 1).

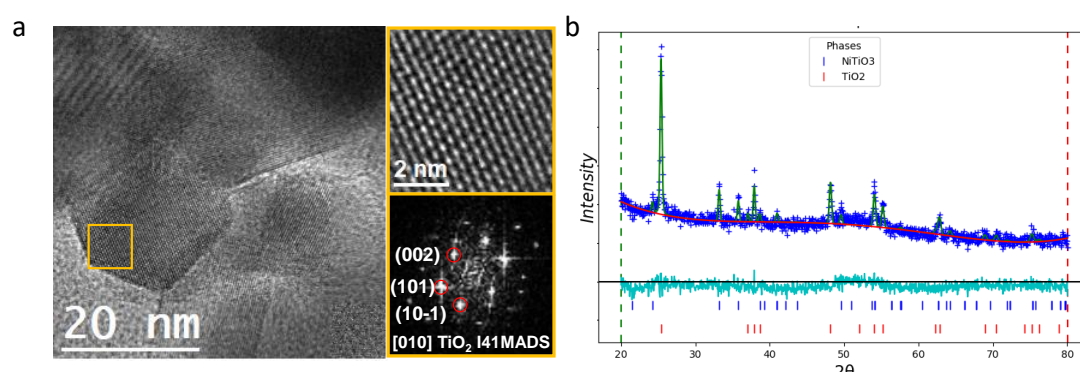


**Figure 8** (a) HRTEM micrographs of NiTiO<sub>3</sub>/TiO<sub>2</sub> (1%), detail of the yellow squared region and its corresponding power spectrum. (b) Refined fitting of the NiTiO<sub>3</sub>/TiO<sub>2</sub>(5%) x-ray diffraction data. Blue symbols: experimental data; continuous red line: modified background; continuous green line: calculated modelled structure; continuous light blue line beneath pattern: difference between observed and calculated parameters. Blue tickmarks correspond to reflections of NiTiO<sub>3</sub> (R-3) unit cell, lower red ones to TiO<sub>2</sub> (I41/amd) unit cell. GOF = 1.21. Rw = 6.99%.

HRTEM analysis confirmed the annealed material to contain mostly anatase TiO<sub>2</sub> (Figures 7 and 8a).<sup>45</sup> EELS elemental maps of the annealed materials showed Ni, Ti and O to be evenly distributed throughout the nanostructures (Figure 5e). The lack of evidences of the presence of large NiTiO<sub>3</sub> crystal domains and the homogeneous distribution of Ni throughout the material observed by EELS and EDX analyses pointed at the growth of small NiTiO<sub>3</sub> domains as a discontinuous shell on the surface of the porous TiO<sub>2</sub> nanostructures.<sup>46</sup> XPS analyses of the annealed samples displayed only one chemical state for Ti, assigned to Ti<sup>4+</sup>, and one for Ni, assigned to Ni<sup>2+</sup>, consistently with XRD, HRTEM, EELS and EDX characterization (Figures 9).<sup>47</sup> XPS analysis showed the amount of Ni to be almost a twofold of that measured by EDX, pointing at its

preferential surface location (Table 1).

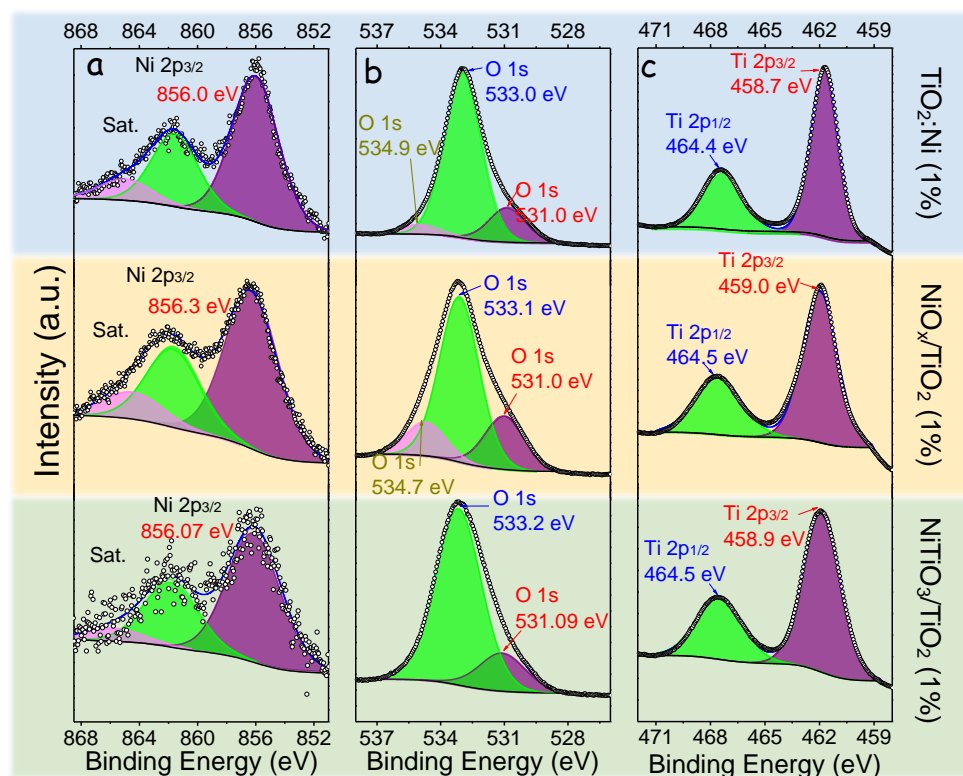


**Figure 9.** Ni 2p<sub>3/2</sub> region (a), O 1s region (b) and Ti 2p region (c) of the XPS spectra of (1) TiO<sub>2</sub>:Ni (1%) (2) NiO<sub>x</sub>/TiO<sub>2</sub> (1%) and (3) NiTiO<sub>3</sub>/TiO<sub>2</sub> (1%) samples.

When the Ni-doped material was annealed under Ar instead of air, the sample color changed from blue to black, instead of yellow (Figure 6), but the elongated geometry of the annealed structures was conserved. In contrast to the annealing in air, the nanostructuring of the original nanoneedle bundles partially persisted after annealing in argon. The particles annealed in argon did not show full crystallographic continuity and contained a lower density of holes compared with the material obtained from the annealing in air (Figure 10a). XRD patterns of materials annealed under argon showed anatase TiO<sub>2</sub> as the main phase, with no evidence of the presence of NiTiO<sub>3</sub>, but with a small XRD peak at  $2\theta=28.6^\circ$  that we associated to a NiO<sub>x</sub> phase (Figure 10a). The black nanopowder annealed under argon showed a magnetic moment, which further pointed toward the formation of a NiO<sub>x</sub> phase (Figure 6, 10a,b).<sup>48</sup> We hypothesize that the porous geometry of the NiTiO<sub>3</sub>/TiO<sub>2</sub> structures obtained after annealing TiO<sub>2</sub>:Ni in air was created by the sintering of the nanoneedle

bundles. The large density of interfaces of the initial bundles translated in the formation of a large density of holes on the sintered material, which could be aided by the simultaneous outward diffusion of Ni ions to form NiTiO<sub>3</sub> domains. On the contrary, annealing in argon did not allow a similar level of sintering of the nanostructures, which was promoted in air by the ubiquitous presence of oxygen. Thus, the material obtained from the annealing process in argon maintained smaller crystal domains and presented a less porous structure. The specific surface areas of NiTiO<sub>3</sub>/TiO<sub>2</sub> and NiO<sub>x</sub>/TiO<sub>2</sub> is 28.0 and 40.8 m<sup>2</sup>·g<sup>-1</sup>, respectively, matching with the process of formation (Figure 10c,d). With the annealing process in air, pure TiO<sub>2</sub> nanopowders did not result in porous materials as those obtained from TiO<sub>2</sub>:Ni because they did not present a proper initial nanostructuration.

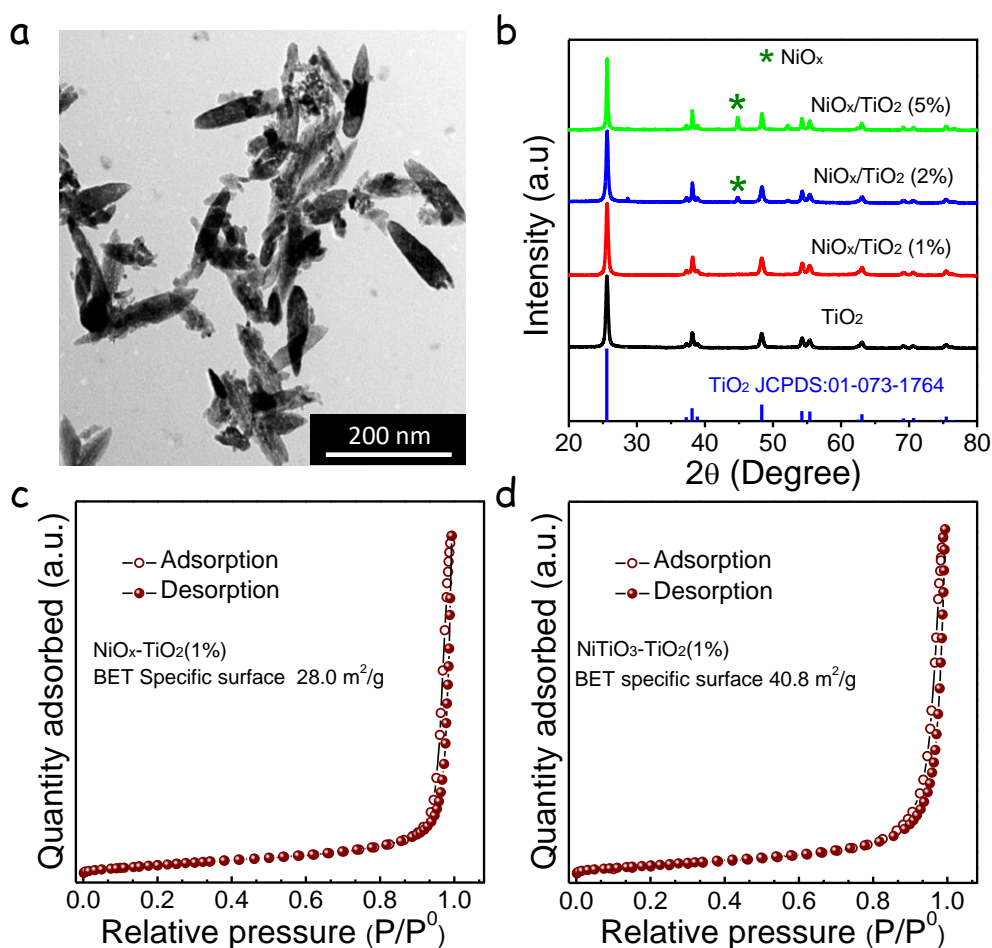


**Figure 10.** (a) TEM image of NiO<sub>x</sub>/TiO<sub>2</sub> (5%) annealed in argon. (b) XRD pattern of TiO<sub>2</sub> and NiO<sub>x</sub>/TiO<sub>2</sub> (1%, 2%, 5%) annealed in argon. Nitrogen adsorption (open symbols) and desorption (filled symbols) isotherms measured of (c) NiO<sub>x</sub>-TiO<sub>2</sub>(1%) and (d)

NiTiO<sub>3</sub>-TiO<sub>2</sub>(1%) at 77.3 K.

### **Photogeneration of Hydrogen**

To test their photocatalytic properties toward hydrogen evolution, the annealed materials were supported on a conventional filter paper and placed on a reactor containing a UV LED light source. An Ar flow saturated with a water-ethanol vapor mixture was flowed through this reactor. Exhaust gases were analyzed using GC, being acetaldehyde and hydrogen the main reaction products (Figure 1).

Figure 11a shows the accumulated hydrogen production during a 32 min reaction for NiTiO<sub>3</sub>/TiO<sub>2</sub> hetero-nanostructures having different nominal Ni concentrations. Data for bare TiO<sub>2</sub> and pure NiTiO<sub>3</sub> (Figures 12a,b) prepared following the same procedure (see experimental section for details) were also plotted in Figure 11a as reference. NiTiO<sub>3</sub>/TiO<sub>2</sub> hetero-nanostructures with a nominal 1% of Ni systematically provided the highest hydrogen production rates, with values up to 11.5 mmol·h<sup>-1</sup>g<sup>-1</sup> and an AQY of 11.6% at 365 nm, well above those previously reported for other Ni-Ti-O systems (Table 2). The hydrogen production rate of NiTiO<sub>3</sub>/TiO<sub>2</sub> (1%) was almost a fourfold higher than that of bare TiO<sub>2</sub> and 60 times larger than that of pure NiTiO<sub>3</sub> (Figure 11b, 13). The presence of larger amounts of Ni did not improve the evolution rate with respect to NiTiO<sub>3</sub>/TiO<sub>2</sub> (1%). We associate this experimental evidence with the blocking of the TiO<sub>2</sub> surface active sites when too large amounts of NiTiO<sub>3</sub> were grown on the TiO<sub>2</sub> surface. SEM characterization showed the morphology of the NiTiO<sub>3</sub>/TiO<sub>2</sub> hetero-nanostructures to remain unmodified after the catalytic test (Figure 11c). and SEM images of NiTiO<sub>3</sub>/TiO<sub>2</sub> (5%) before and after 30 min photocatalytic test.

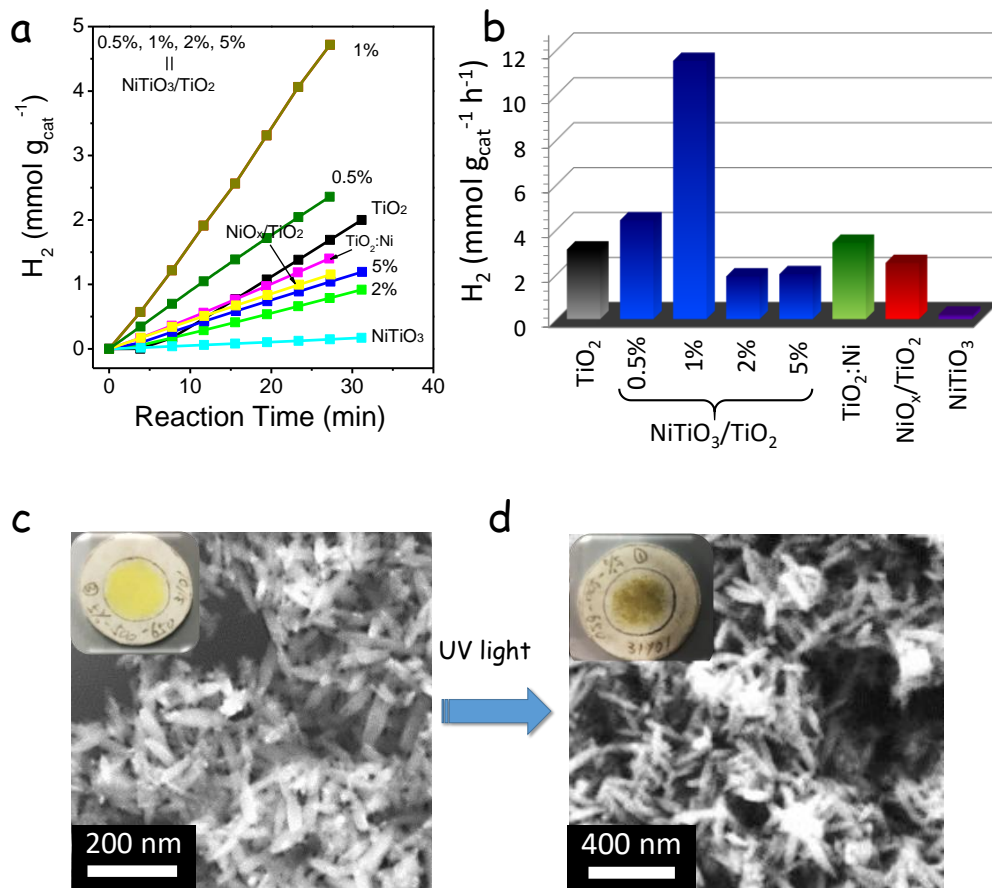


**Figure 11.** (a) H<sub>2</sub> production of TiO<sub>2</sub>, NiTiO<sub>3</sub>/TiO<sub>2</sub> (1%, 2%, 5%), NiO<sub>x</sub>/TiO<sub>2</sub> (1%) and NiTiO<sub>3</sub>. (b) H<sub>2</sub> production rate of TiO<sub>2</sub>, NiTiO<sub>3</sub>/TiO<sub>2</sub> (1%, 2%, 5%), NiO<sub>x</sub>/TiO<sub>2</sub> (1%) and NiTiO<sub>3</sub>. (c, d) Optical and SEM images of NiTiO<sub>3</sub>/TiO<sub>2</sub> (5%) before and after 30 min photocatalytic test.

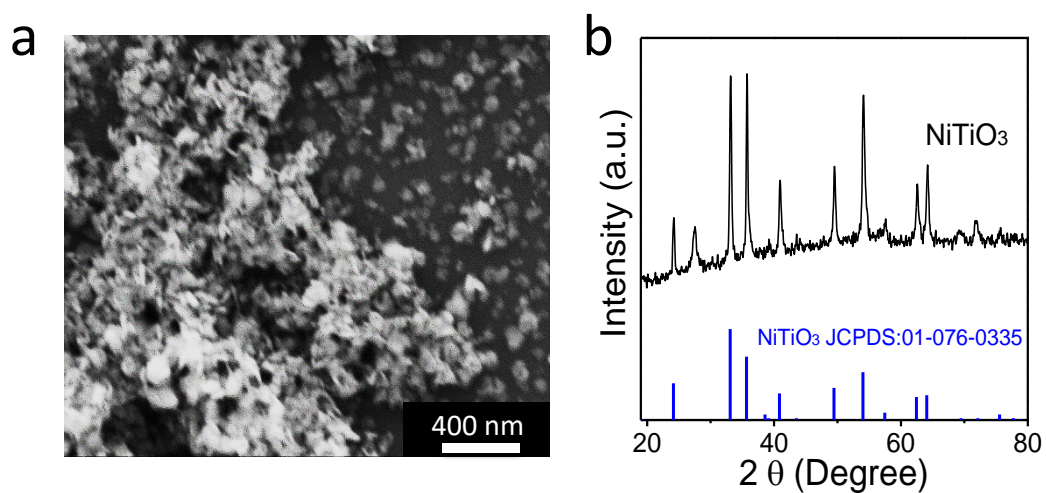


**Figure 12.** (a) SEM images (b) XRD pattern of NiTiO<sub>3</sub>.

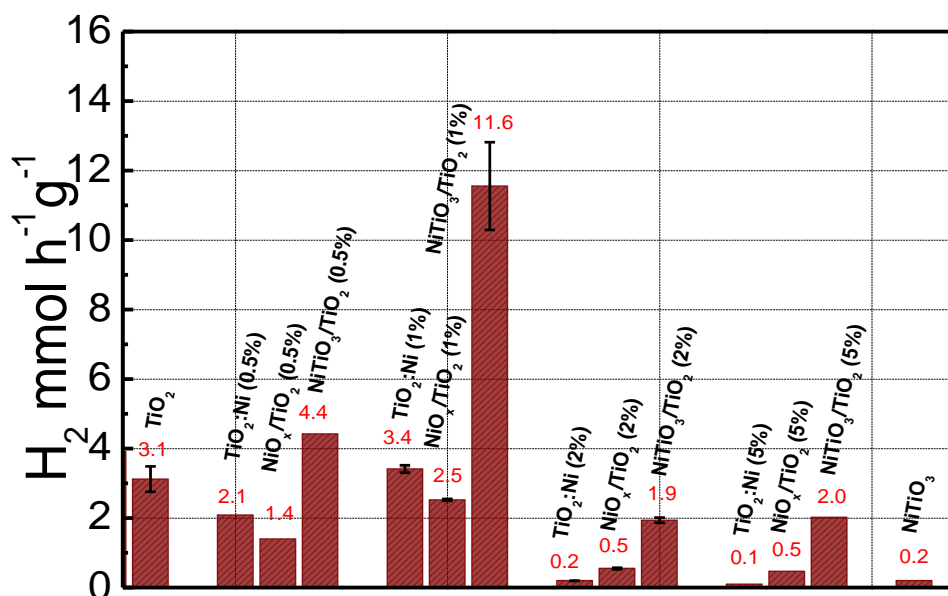


**Figure 13.** Photocatalytic H<sub>2</sub> production rates obtained from TiO<sub>2</sub>, NiTiO<sub>3</sub>, TiO<sub>2</sub>:Ni (1%), NiO<sub>x</sub>/TiO<sub>2</sub> (1%), NiTiO<sub>3</sub>/TiO<sub>2</sub> (1%, 2%, 5%).

**Table 2.** Comparison of the hydrogen evolution rate and the apparent quantum yield with reported Ni-Ti-O systems.

Photocatalyst	H <sub>2</sub> Evolution Rate μmol h <sup>-1</sup> g <sup>-1</sup>	Reaction conditions	AQY %	Ref.
Ni/NiO/N-TiO <sub>2-x</sub>	185	110W λ>420nm	7.5	S1
0.23%Ni(OH) <sub>2</sub> on TiO <sub>2</sub>	900	3W 365nm	12.4	S2
0.25wt% NiO-TiO <sub>2</sub>	261	3W 365nm	1.7	S3
TiO <sub>2</sub> -Ni(HCO <sub>3</sub> ) <sub>2</sub> -2.5%	377	300W 380nm (±5nm)	6.24	S4
0.32% Ni(NO <sub>3</sub> ) <sub>2</sub> -TiO <sub>2</sub>	163	3W 365nm	8.1	S5
Mesoporous NiO/TiO <sub>2</sub>	240	3W 365nm	1.7	S6
Pt NiO/TiO <sub>2</sub> 1:1 molar ratio	1,250	400W UV	7.8	S7
Hollow NiTiO <sub>3</sub> /TiO <sub>2</sub> (1%)	11,500	365nm	11.6	This work

We believe the enhancement of the photocatalytic properties of TiO<sub>2</sub> with the NiTiO<sub>3</sub> introduction to be related with an improvement of three fundamental parameters: i) surface area; ii) light absorption; and iii) charge separation. We estimate that the introduction of Ni had associated a factor 3 increase of the surface area with respect

to pure TiO<sub>2</sub> through the formation of the porous NiTiO<sub>3</sub>/TiO<sub>2</sub> hetero-nanostructures during the annealing process. Additionally, the presence of NiTiO<sub>3</sub> provided a higher light absorption coefficient at the used excitation wavelength. In case of using solar radiation, the presence of NiTiO<sub>3</sub> would provide an even larger improvement with respect to pure TiO<sub>2</sub>, as it would allow absorbing a larger portion of the solar spectra due to its smaller band gap (Figure 14). Besides, the proper band alignment of TiO<sub>2</sub> and NiTiO<sub>3</sub> allowed an efficient spatial charge separation that significantly reduced recombination of the photogenerated charge carriers before reaction.

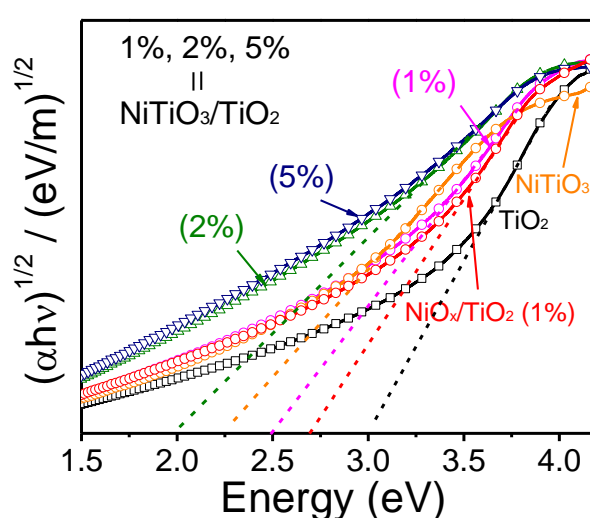


**Figure 14.** Kubelka-Munk function for TiO<sub>2</sub>, NiTiO<sub>3</sub>/TiO<sub>2</sub> (1, 2, 5%) and NiO<sub>x</sub>/TiO<sub>2</sub> including a linear fit (dashed lines) to determine the band gap energy.

To gain additional insight into the band structure alignment and the interfacial charge carrier dynamics at the NiTiO<sub>3</sub>/TiO<sub>2</sub> heterostructure, EIS analyses were carried out on TiO<sub>2</sub>, NiTiO<sub>3</sub>/TiO<sub>2</sub> (1%) and NiTiO<sub>3</sub> thin films in dark conditions. Representative impedance responses in the form of Nyquist plot for TiO<sub>2</sub> and NiTiO<sub>3</sub>/TiO<sub>2</sub> (1%) are displayed in Figure 15a. Responses typically feature a single semicircle. Interestingly, the size of the semicircle obtained for the TiO<sub>2</sub> sample was reduced with the incorporation of Ni. A more quantitative description of the EIS data can be provided by modelling the electrical response with an equivalent circuit, such as a Randles circuit (Figure 15a inset), which has been previously reported to successfully describe

nanostructured TiO<sub>2</sub> and other photocatalysts.<sup>22,50,54</sup> This circuit consists of a resistor  $R_S$  in series with a bulk capacitance  $C_{bulk}$ , attributed to the space charge region, and a second resistor  $R_{ct,bulk}$  that represents the charge transport resistance, both in parallel. At a first glance, the decrease in the size of the semicircle with the incorporation of Ni in TiO<sub>2</sub> suggests the reduction in the charge transport resistance,<sup>49,50</sup> which is further confirmed with the decrease of  $R_{ct,bulk}$  from 15.4 kΩ to 9.8 kΩ pointing out the amelioration of the charge transport process. In addition, the electron lifetime  $\tau_n$  can be calculated as the inverse of the angular frequency at the maximum of the Nyquist plot ( $2\pi f_{max}$ ),<sup>22</sup> highlighted in Figure 15a. Results reveal that  $\tau_n$  increases from 4.5 ms to 6.6 ms when the heterostructure is formed. In general,  $\tau_n$  is considered a metric of electron recombination, *i.e.*, the longer the value the lesser the charge recombination. The lengthening of  $\tau_n$  when TiO<sub>2</sub> is interfaced with NiTiO<sub>3</sub> underpins the effective charge carrier separation across the n-n heterojunction and thus the enhanced photocatalytic activity of the composite with respect TiO<sub>2</sub>. Similar behavior was reported by Wei and co-workers on NiTiO<sub>3</sub>/TiO<sub>2</sub> composite for inorganic sensitized solar cells.<sup>22</sup>

In an attempt to further interrogate the energy band positions, Mott–Schottky (M–S) plots were constructed from  $C_{bulk}$  values extracted from EIS measurements on TiO<sub>2</sub> and NiTiO<sub>3</sub> and further analyzed using the M–S equation:

$$C_{bulk}^{-2} = \frac{2}{qA^2 \epsilon \epsilon_0 N_D} \left( V - V_{fb} - \frac{kT}{q} \right)$$

where  $q$  is elementary charge,  $A$  is taken as the geometric area (assuming a low surface roughness spin-coated thin film),  $\epsilon$  is relative permittivity (taken to be 55 and 15 for TiO<sub>2</sub><sup>51</sup> and NiTiO<sub>3</sub>,<sup>52</sup> respectively),  $\epsilon_0$  is vacuum permittivity,  $N_D$  is donor density,  $V$  is applied potential,  $V_{fb}$  is flat band potential,  $k$  is Boltzmann constant, and  $T$  is absolute temperature. The positive slope in the linear region (dashed line in Figure 4b) unambiguously confirmed the n-type character of both NiTiO<sub>3</sub> and TiO<sub>2</sub>, whereas  $V_{fb}$  values of –0.186 V and –0.276 V vs. RHE were obtained for TiO<sub>2</sub> and NiTiO<sub>3</sub>, respectively. Likewise,  $N_D$  shows values of  $1.1 \times 10^{18} \text{ cm}^{-3}$  for TiO<sub>2</sub> and  $5.5 \times 10^{17} \text{ cm}^{-3}$  for NiTiO<sub>3</sub>. Similar values have also been reported by Thimsen et al. on nanocrystalline

anatase TiO<sub>2</sub>,<sup>51</sup> and by Trari and co-workers on nanostructured NiTiO<sub>3</sub>.<sup>53</sup> We note that the depletion width is estimated to be 20 nm in the linear region of M–S plot for both TiO<sub>2</sub> and NiTiO<sub>3</sub> so that M–S analysis can be reasonably applied in the case of not fully depleted feature.<sup>54</sup> Considering the density-of-state effective mass for electrons  $m_{de}$  for nanocrystalline anatase TiO<sub>2</sub> is  $9.1 \times 10^{-30}$  kg,<sup>51</sup> and for nanostructured NiTiO<sub>3</sub> is  $1.9 \times 10^{-30}$  kg,<sup>55</sup> the effective density of states in the CB  $N_C$  is:<sup>54,56</sup>

$$N_C \equiv 2 \left( \frac{2\pi m_{de} kT}{h^2} \right)^{\frac{3}{2}}$$

where  $h$  is Planck constant.  $N_C$  is estimated to be  $7.7 \times 10^{20}$  cm<sup>-3</sup> for TiO<sub>2</sub>, and  $7.5 \times 10^{19}$  cm<sup>-3</sup> for NiTiO<sub>3</sub>. Since the ratio between  $N_D$  and  $N_C$  is in all cases less than 0.05, both TiO<sub>2</sub> and NiTiO<sub>3</sub> could be treated as nondegenerate semiconductors, and therefore, the Boltzmann statistics can be applied:<sup>54,56</sup>

$$E_{CB} - E_F = kT \ln \left( \frac{N_C}{N_D} \right)$$

where  $E_{CB}$  is the bottom of the CB and  $E_F$  is the Fermi level position.  $E_{CB}$  is found to be around 168 mV and 126 mV above  $V_{fb}$  for TiO<sub>2</sub> and NiTiO<sub>3</sub>, respectively.

Based on the aforementioned results, Figure 15c displays a scheme of the electronic band structures. The relative band alignment between NiTiO<sub>3</sub> and TiO<sub>2</sub> allows the formation of a direct Z-scheme heterojunction. In such Ni-TiO<sub>2</sub> system, while photogenerated electrons in the CB of TiO<sub>2</sub> recombine with photogenerated holes in the VB of NiTiO<sub>3</sub>, photogenerated electrons with strong reduction ability remain in the CB of NiTiO<sub>3</sub> ready to reduce water into hydrogen and photogenerated holes with strong oxidation abilities in the VB of TiO<sub>2</sub> could drive ethanol dehydrogenation to acetaldehyde and hydrogen. Therefore, the formation of a direct Z-scheme NiTiO<sub>3</sub>/TiO<sub>2</sub> heterojunction can promote photogenerated carriers with strong redox abilities to drive photocatalytic reaction.<sup>57</sup> As a result, NiTiO<sub>3</sub>/TiO<sub>2</sub> composites at optimal NiTiO<sub>3</sub> loading condition shows a significantly increased photocatalytic activity. Similar Z-scheme photocatalytic systems have also been reported such as TiO<sub>2</sub>/Rh,<sup>58</sup> TiO<sub>2</sub>/CdS,<sup>59</sup> and CdS/cobalt–benzimidazole.<sup>60</sup>

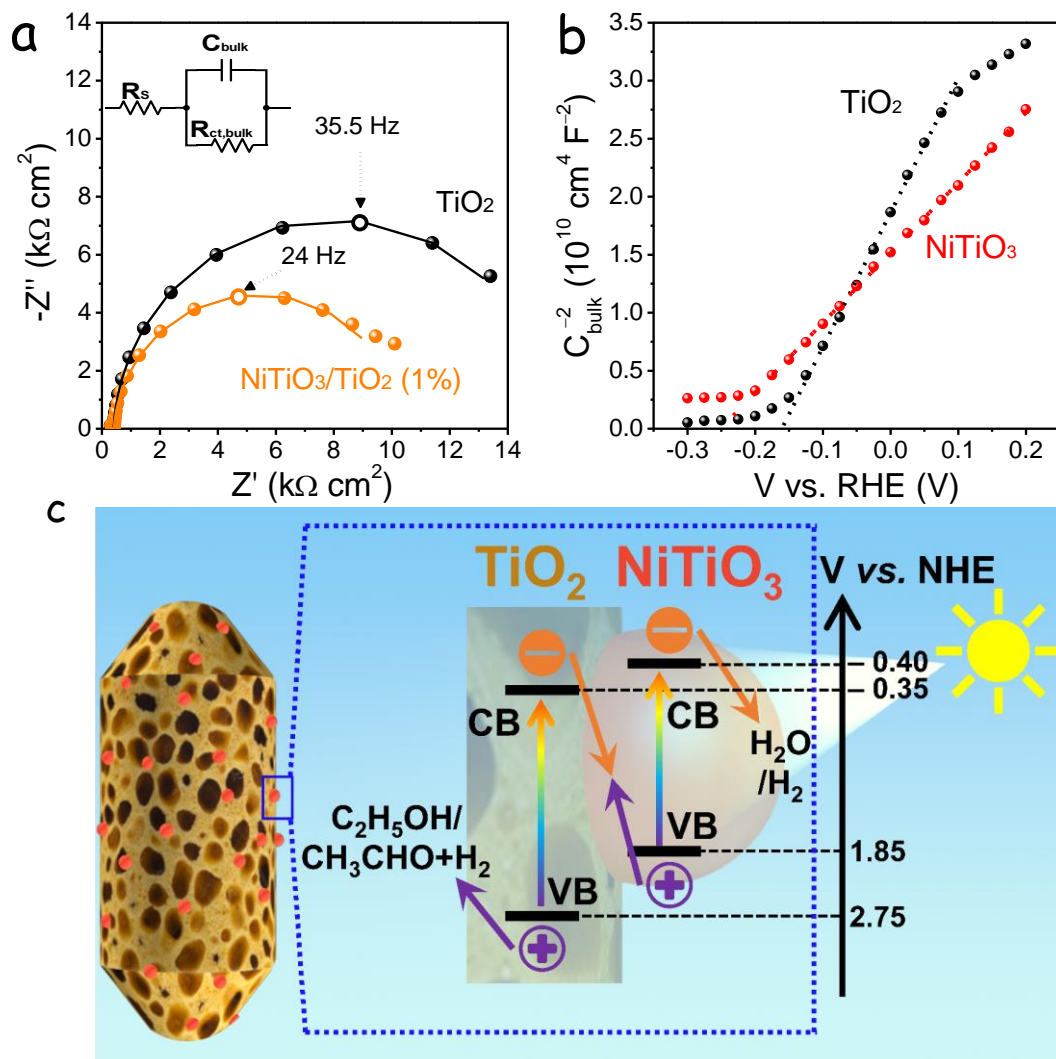


**Figure 15.** a) Representative impedance response of  $\text{TiO}_2$  (black sphere) and  $\text{NiTiO}_3/\text{TiO}_2$  (1%) (orange sphere) with the corresponding fit (solid lines) in Nyquist plot. The maximum point of the Nyquist plot is highlighted (hollow), and the equivalent circuit used is included as an inset. b) Mott–Schottky plot of  $\text{TiO}_2$  (black sphere) and  $\text{NiTiO}_3$  (red sphere) including a linear fit (dashed lines). c) Schematics of the electronic band structures of a Z-scheme  $\text{NiTiO}_3/\text{TiO}_2$  heterojunction.

## 2.5 Conclusions

Porous  $\text{NiTiO}_3/\text{TiO}_2$  heterostructures were prepared from the annealing in air of  $\text{TiO}_2\text{:Ni}$  nanoneedle bundles obtained from a hydrothermal route. Pores were generated during the sintering of the nanostructured bundles due to the presence of a large density of interfaces on the precursor material.  $\text{NiTiO}_3/\text{TiO}_2$  heterostructures were used for photocatalytic hydrogen generation from ethanol-water solutions at room temperature.  $\text{NiTiO}_3/\text{TiO}_2$  hetero-structures provided unprecedented  $\text{H}_2$

production rates up to  $11.5 \text{ mmol}\cdot\text{h}^{-1}\text{g}^{-1}$  and an AQY of 11.6%. This excellent performance was associated to the improvement of three parameters, surface area, light absorption and charge separation. We estimated a factor 3 increase of the surface area with the introduction of Ni through the formation of porous NiTiO<sub>3</sub>/TiO<sub>2</sub> hetero-nanostructures during the annealing in air. Additionally, the presence of NiTiO<sub>3</sub>, with a lower band gap energy, provided a higher light absorption coefficient at the excitation wavelength. Besides, TiO<sub>2</sub> and NiTiO<sub>3</sub> presented a proper band alignment that allows an efficient spatial charge separation of the photogenerated charge carriers before reaction, as confirmed by EIS analysis.

## 2.6 References

1. Wu, X.; Lu, G. Q. Wang, L., Shell-in-shell TiO<sub>2</sub> hollow spheres synthesized by one-pot hydrothermal method for dye-sensitized solar cell application. *Energy Environ. Sci.*, **2011**, *4*, 3565–3572.
2. Wang, D. P.; H. C. Zeng, Multifunctional Roles of TiO<sub>2</sub> Nanoparticles for Architecture of Complex Core–Shells and Hollow Spheres of SiO<sub>2</sub>–TiO<sub>2</sub>–Polyaniline System. *Chem. Mater.*, **2009**, *21*, 4811–4823.
3. Xiang, Q.; Yu, J.; Jaroniec, M. Synergetic Effect of MoS<sub>2</sub> and Graphene as Cocatalysts for Enhanced Photocatalytic H<sub>2</sub> Production Activity of TiO<sub>2</sub> Nanoparticles. *J. Am. Chem. Soc.*, **2012**, *134*, 6575–6578.
4. Ma, Y.; Wang, X.; Jia, Y.; Chen, X.; Han, H.; Li, C. Titanium Dioxide-Based Nanomaterials for Photocatalytic Fuel Generations. *Chem. Rev.*, **2014**, *114*, 9987–10043.
5. Su, D.; Dou, S.; Wang, G.; Anatase TiO<sub>2</sub>: Better Anode Material Than Amorphous and Rutile Phases of TiO<sub>2</sub> for Na-Ion Batteries. *Chem. Mater.*, **2015**, *27*, 6022–6029.
6. Liu, J.; Bai, H.; Wang, Y.; Liu, Z.; Zhang, X.; Sun, D. D. Self-Assembling TiO<sub>2</sub> Nanorods on Large Graphene Oxide Sheets at a Two-Phase Interface and Their Anti-Recombination in Photocatalytic Applications. *Adv. Funct. Mater.*, **2010**, *20*, 4175–4181.
7. Liu, B.; Zeng, H. C. Carbon Nanotubes Supported Mesoporous Mesocrystals of Anatase TiO<sub>2</sub>. *Chem. Mater.*, **2008**, *20*, 2711–2718.
8. Gopal, N. O.; Lo, H. H.; Ke, S. C. Chemical State and Environment of Boron Dopant in B,N-Codoped Anatase TiO<sub>2</sub> Nanoparticles: An Avenue for Probing Diamagnetic Dopants in TiO<sub>2</sub> by Electron Paramagnetic Resonance Spectroscopy. *J. Am. Chem. Soc.*, **2008**, *130*, 2760–2761.
9. Burda, C.; Lou, Y.; Chen, X.; Samia, A. C. S.; Stout, J.; Gole, J. L. Enhanced Nitrogen Doping in TiO<sub>2</sub> Nanoparticles. *Nano Lett.*, **2003**, *3*, 1049–1051.
10. Chiodi, M.; Cheney, C. P.; Vilmercati, P.; Cavaliere, E.; Mannella, N.; Weitering, H. H.; Gavioli, L. Enhanced Dopant Solubility and Visible-Light Absorption in Cr–N Codoped TiO<sub>2</sub> Nanoclusters. *J. Phys. Chem. C*, **2012**, *116*, 311–318.
11. Bouchet, R.; Weibel, A.; Knauth, P.; Mountjoy, G.; Chadwick, A. V. EXAFS Study of Dopant Segregation (Zn, Nb) in Nanocrystalline Anatase (TiO<sub>2</sub>). *Chem. Mater.*,

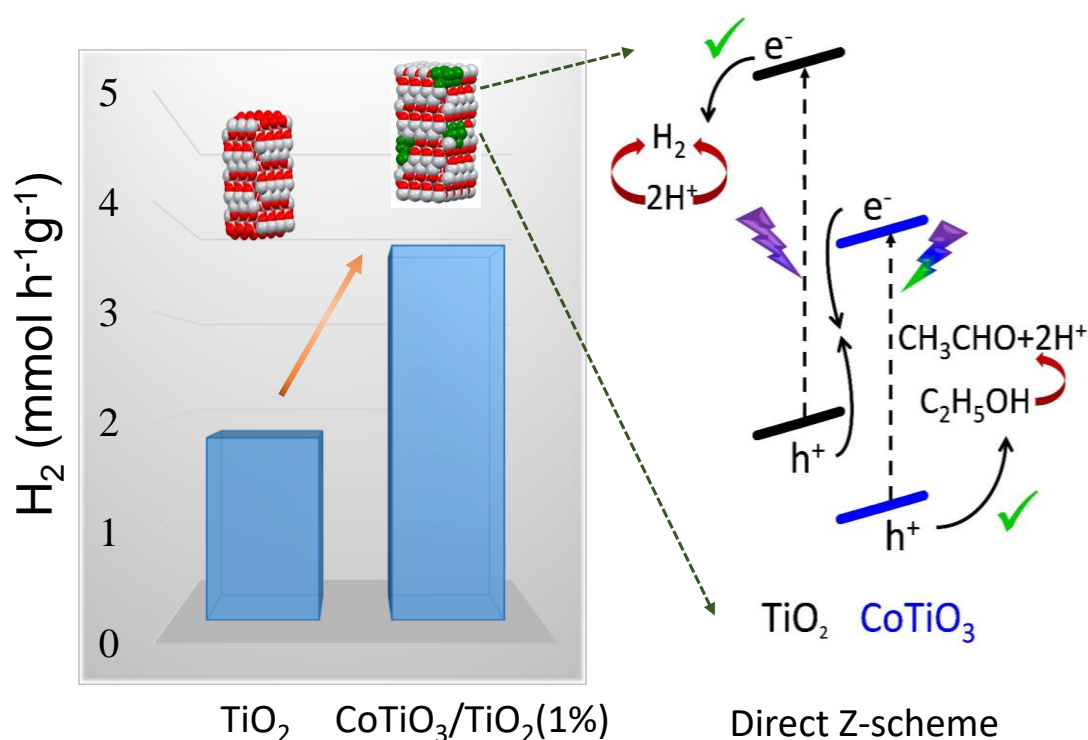
- 2003**, *15*, 4996–5002.
12. Murdoch, M.; Waterhouse, G. I. N.; Nadeem, M. A.; Metson, J. B.; Keane, M. A.; Howe, R. F.; Llorca, J.; Idriss, H. The effect of gold loading and particle size on photocatalytic hydrogen production from ethanol over Au/TiO<sub>2</sub> nanoparticles. *Nat. Chem.*, **2011**, *3*, 489–492.
  13. Waterhouse, G. I. N.; Wahab, A. K.; Al-Oufi, M.; Jovic, V.; Anjum, D. H.; Sun-Waterhouse, D.; Llorca, J.; H. Idriss, Hydrogen production by Tuning the Photonic Band Gap with the Electronic Band Gap of TiO<sub>2</sub>. *Sci. Rep.*, **2013**, *3*, 2849.
  14. Pan, J. H.; Zhang, X.; Du, A. J.; Sun, D. D.; Leckie, J. O. Self-Etching Reconstruction of Hierarchically Mesoporous F-TiO<sub>2</sub> Hollow Microspherical Photocatalyst for Concurrent Membrane Water Purifications. *J. Am. Chem. Soc.*, **2008**, *130*, 11256–11257.
  15. Yang, S. C.; Yang, D. J.; Kim, J.; Hong, J. M.; Kim, H. G.; Kim, I. D.; Lee, H. Hollow TiO<sub>2</sub> Hemispheres Obtained by Colloidal Templating for Application in Dye-Sensitized Solar Cells. *Adv. Mater.*, **2008**, *20*, 1059–1064.
  16. Hwang, J. Y.; Kim, H. M.; Lee, S. K.; Lee, J. H.; Abouimrane, A.; Khaleel, M. A.; Belharouak, I.; Manthiram A.; Sun, Y. K. Lithium-Sulfur Batteries: High-Energy, High-Rate, Lithium–Sulfur Batteries: Synergetic Effect of Hollow TiO<sub>2</sub>-Webbed Carbon Nanotubes and a Dual Functional Carbon-Paper Interlayer. *Adv. Energy Mater.*, **2016**, *6*, 1–7.
  17. Fan, H.; Li, H.; Liu, B.; Lu, Y.; Xie, T.; Wang, D. Photoinduced Charge Transfer Properties and Photocatalytic Activity in Bi<sub>2</sub>O<sub>3</sub>/BaTiO<sub>3</sub> Composite Photocatalyst. *ACS Appl. Mater. Interfaces*, **2012**, *4*, 4853–4857.
  18. Inceesungvorn, B.; Teeranunpong, T.; Nunkaew, J.; Suntalelat, S.; Tantraviwat, D. Novel NiTiO<sub>3</sub>/Ag<sub>3</sub>VO<sub>4</sub> composite with enhanced photocatalytic performance under visible light. *Catal. Commun.*, **2014**, *54*, 35–38.
  19. Wang, X.; Xu, C.-N.; Yamada, H.; Nishikubo, K.; Zheng, X.-G. Electro-Mechano-Optical Conversions in Pr<sup>3+</sup>-Doped BaTiO<sub>3</sub>–CaTiO<sub>3</sub> Ceramics. *Adv. Mater.*, **2005**, *17*, 1254–1258.
  20. Wu, F.; Yu, Y.; Yang, H.; German, L. N.; Li, Z.; Chen, J.; Yang, W.; Huang, L.; Shi, W.; Wang, L. Wang, X. Simultaneous Enhancement of Charge Separation and Hole Transportation in a TiO<sub>2</sub>–SrTiO<sub>3</sub> Core–Shell Nanowire Photoelectrochemical System. *Adv. Mater.*, **2017**, *29*, 1701432.
  21. Qu, Y.; Zhou, W.; Ren, Z.; Du, S.; Meng, X.; Tian, G.; Pan, K.; Wang, G.; Fu, H. Facile preparation of porous NiTiO<sub>3</sub> nanorods with enhanced visible-light-driven photocatalytic performance. *J. Mater. Chem.*, **2012**, *22*, 16471–16476.
  22. Li, Y.-Y.; Wang, J.-G.; Sun, H.-H.; Wei, B. Heterostructured TiO<sub>2</sub>/NiTiO<sub>3</sub> Nanorod Arrays for Inorganic Sensitized Solar Cells with Significantly Enhanced Photovoltaic Performance and Stability. *ACS Appl. Mater. Interfaces*, **2018**, *10*, 11580–11586.
  23. Dahl, M.; Liu, Y.; Yin, Y. Composite Titanium Dioxide Nanomaterials. *Chem. Rev.*, **2014**, *114*, 9853–9889.
  24. Tang, C.; Xu, W.; Chen, C.; Li, Y.; Xu, L. Unraveling the Orientation of MoS<sub>2</sub> on TiO<sub>2</sub> for Photocatalytic Water Splitting. *Adv. Mater. Interfaces*, **2017**, *4*, 1700361.
  25. Tian, J.; Hao, P.; Wei, N.; Cui, H.; Liu, H. 3D Bi<sub>2</sub>MoO<sub>6</sub> Nanosheet/TiO<sub>2</sub> Nanobelt Heterostructure: Enhanced Photocatalytic Activities and Photoelectrochemistry

- Performance. *ACS Catal.*, **2015**, *5*, 4530–4536.
26. Barreca, D.; Carraro, G.; Gasparotto, A.; Maccato, C.; Warwick, M. E. A.; Kaunisto, K.; Sada, C.; Turner, S.; Gönüllü, Y.; Ruoko, T. P.; Borgese, L.; Bontempi, E.; Tendeloo, G.; Lemmetyinen, Van H.; Mathur, S. Fe<sub>2</sub>O<sub>3</sub>–TiO<sub>2</sub> Nano-heterostructure Photoanodes for Highly Efficient Solar Water Oxidation. *Adv. Mater. Interfaces*, **2015**, *2*, 1–11.
  27. Rawool, A.; Pai, M. R.; Banerjee, A. M.; Arya, A.; Ningthoujam, R.; Tewari, R.; Rao, R.; Chalke, B.; Ayyub, P.; Tripathi, A. *pn* Heterojunctions in NiO:TiO<sub>2</sub> composites with type-II band alignment assisting sunlight driven photocatalytic H<sub>2</sub> generation. *Appl. Catal. B Environ.*, **2018**, *221*, 443–458.
  28. Wei, Y.; Cheng, G.; Xiong, J.; Xu, F.; Chen, R. Positive Ni(HCO<sub>3</sub>)<sub>2</sub> as a Novel Cocatalyst for Boosting the Photocatalytic Hydrogen Evolution Capability of Mesoporous TiO<sub>2</sub> Nanocrystals. *ACS Sustain. Chem. Eng.*, **2017**, *5*, 5027–5038.
  29. Yu, J.; Hai, Y.; Cheng, B. Enhanced Photocatalytic H<sub>2</sub>-Production Activity of TiO<sub>2</sub> by Ni(OH)<sub>2</sub> Cluster Modification. *J. Phys. Chem. C*, **2011**, *115*, 4953–4958.
  30. Hu, S.; Li, F.; Fan, Z.; Gui, J. Improved photocatalytic hydrogen production property over Ni/NiO/N–TiO<sub>2-x</sub> heterojunction nanocomposite prepared by NH<sub>3</sub> plasma treatment. *J. Power Sources*, **2014**, *250*, 30–39.
  31. Liu, S.; Xue, S.; Zhang, W.; Zhai, J.; Chen, G. Significantly enhanced dielectric property in PVDF nanocomposites flexible films through a small loading of surface-hydroxylated Ba<sub>0.6</sub>Sr<sub>0.4</sub>TiO<sub>3</sub> nanotubes. *J. Mater. Chem. A*, **2014**, *2*, 18040–18046.
  32. Pan, J. H.; Shen, C.; Ivanova, I.; Zhou, N.; Wang, X.; Tan, W. C.; Xu, Q. H.; Bahnemann, D. W.; Wang, Q. Self-Template Synthesis of Porous Perovskite Titanate Solid and Hollow Submicrospheres for Photocatalytic Oxygen Evolution and Mesoscopic Solar Cells. *ACS Appl. Mater. Interfaces*, **2015**, *7*, 14859–14869.
  33. Xin, Y.; Jiang, J.; Huo, K.; Hu, T.; Chu, P. K. Bioactive SrTiO<sub>3</sub> Nanotube Arrays: Strontium Delivery Platform on Ti-Based Osteoporotic Bone Implants. *ACS Nano*, **2009**, *3*, 3228–3234.
  34. Peng, S.; Yang, Y.; Tan, J.; Gan, C.; Li, Y. In situ loading of Ni<sub>2</sub>P on Cd<sub>0.5</sub>Zn<sub>0.5</sub>S with red phosphorus for enhanced visible light photocatalytic H<sub>2</sub> evolution. *Appl. Surf. Sci.*, **2018**, *447*, 822–828.
  35. Zhang, W.; Li, Y.; Peng, S. Template-free synthesis of hollow Ni/reduced graphene oxide composite for efficient H<sub>2</sub> evolution. *J. Mater. Chem. A*, **2017**, *5*, 13072–13078.
  36. Peng, S.; Zeng X.; Li, Y. Titanate nanotube modified with different nickel precursors for enhanced Eosin Y-sensitized photocatalytic hydrogen evolution. *Int. J. Hydrogen Energy*, **2015**, *40*, 6038–6049.
  37. Molins, E.; Benito, M.; Mata, I.; Martínez, L.; Soler, L.; Llorca, J. Au/TiO<sub>2</sub> Lyogels for Hydrogen Production. *MRS Adv.*, **2017**, *2*, 3499–3504.
  38. Martínez, L.; Soler, L.; Angurell, I.; Llorca, J. Effect of TiO<sub>2</sub> nanoshape on the photoproduction of hydrogen from water-ethanol mixtures over Au<sub>3</sub>Cu/TiO<sub>2</sub> prepared with preformed Au-Cu alloy nanoparticles. *Appl. Catal. B Environ.*, **2019**, *248*, 504–514.
  39. Li, Y.; Han, P.; Hou, Y.; Peng, S.; Kuang, X. Oriented Zn<sub>m</sub>In<sub>2</sub>S<sub>m+3</sub>@In<sub>2</sub>S<sub>3</sub> heterojunction with hierarchical structure for efficient

- photocatalytic hydrogen evolution. *Appl. Catal. B Environ.*, **2019**, *244*, 604–611.
40. Li, Y.; Li, H.; Li, Y.; Peng, S.; Hu, Y. H. Fe-B alloy coupled with Fe clusters as an efficient cocatalyst for photocatalytic hydrogen evolution. *Chem. Eng. J.*, **2018**, *344*, 506–513.
  41. Li, Y.; Hou, Y.; Fu, Q.; Peng, S.; Hu, Y. H. Oriented growth of ZnIn<sub>2</sub>S<sub>4</sub>/In(OH)<sub>3</sub> heterojunction by a facile hydrothermal transformation for efficient photocatalytic H<sub>2</sub> production. *Appl. Catal. B Environ.*, **2017**, *206*, 726–733.
  42. Imani, R.; Dillert, R.; Bahnemann, D. W.; Pazoki, M.; Apih, T.; Kononenko, V.; Repar, N.; Kralj-Iglič, V.; Boschloo, G.; Drobne, D.; Edvinsson, T.; Iglič, A. Multifunctional Gadolinium-Doped Mesoporous TiO<sub>2</sub> Nanobeads: Photoluminescence, Enhanced Spin Relaxation, and Reactive Oxygen Species Photogeneration, Beneficial for Cancer Diagnosis and Treatment. *Small*, **2017**, *13*, 1700349.
  43. Huo, K.; Li, Y.; Chen, R.; Gao, B.; Peng, C.; Zhang, W.; Hu, L.; Zhang, X.; Chu, P. K. Recyclable Non-Enzymatic Glucose Sensor Based on Ni/NiTiO<sub>3</sub>/TiO<sub>2</sub> Nanotube Arrays. *Chempluschem*, **2015**, *80*, 576–582.
  44. Toby, B. H.; Dreele, R. B. Von. GSAS-II: the genesis of a modern open-source all purpose crystallography software package. *J. Appl. Cryst.*, **2013**, *46*, 544–549.
  45. Cozzoli, P. D.; Kornowski, A. Weller, H. Low-Temperature Synthesis of Soluble and Processable Organic-Capped Anatase TiO<sub>2</sub> Nanorods. *J. Am. Chem. Soc.*, **2003**, *125*, 14539–14548.
  46. Wu, H. B.; Hng, H. H.; Lou, X. W. D. Direct Synthesis of Anatase TiO<sub>2</sub> Nanowires with Enhanced Photocatalytic Activity. *Adv. Mater.*, **2012**, *24*, 2567–2571.
  47. Huang, J.; Jiang, Y.; Li, G.; Xue, C.; Guo, W. Hetero-structural NiTiO<sub>3</sub>/TiO<sub>2</sub> nanotubes for efficient photocatalytic hydrogen generation. *Renew. Energy*, **2017**, *111*, 410–415.
  48. Kim, J. H.; Zhu, K.; Yan, Y.; Perkins, C. L.; Frank, A. J. Microstructure and Pseudocapacitive Properties of Electrodes Constructed of Oriented NiO-TiO<sub>2</sub> Nanotube Arrays. *Nano Lett.*, **2010**, *10*, 4099–4104.
  49. Zuo, Y.; Liu, Y.; Li, J.; Du, R.; Yu, X.; Xing, C.; Zhang, T.; Yao, L.; Arbiol, J.; Llorca, J.; Sivula, K.; Guijarro, N.; Cabot, A. Solution-Processed Ultrathin SnS<sub>2</sub>-Pt Nanoplates for Photoelectrochemical Water Oxidation. *ACS Appl. Mater. Interfaces*, **2019**, *11*, 6918–6926.
  50. Zhu, X.; Guijarro, N.; Liu, Y.; Schouwink, P.; Wells, R. A.; Formal, F. Le; Sun, S.; Gao, C.; Sivula, K. Spinel Structural Disorder Influences Solar-Water-Splitting Performance of ZnFe<sub>2</sub>O<sub>4</sub> Nanorod Photoanodes. *Adv. Mater.*, **2018**, *30*, 1801612.
  51. Thimsen, E.; Martinson, A. B. F.; Elam, J. W.; Pellin, M. J. Energy levels, electronic properties, and rectification in ultrathin p-NiO films synthesized by atomic layer deposition. *J. Phys. Chem. C*, **2012**, *116*, 16830–16840.
  52. Chuang, S. H.; Hsieh, M. L.; Wang, D. Y. Structure and Dielectric Properties of NiTiO<sub>3</sub> Powders Synthesized by the Modified Sol-Gel Method. *J. Chinese Chem. Soc.*, **2012**, *59*, 628–632.
  53. Boudjellal, L.; Belhadi, A.; Brahimi, R.; Boumaza S.; Trari, M. Physical and photoelectrochemical properties of the ilmenite NiTiO<sub>3</sub> prepared by wet chemical method and its application for O<sub>2</sub> evolution under visible light. *Mater. Sci. Semicond. Process.*, **2018**, *75*, 247–252.

54. Liu, Y.; Formal, F. Le; Boudoire, F.; Yao, L.; Sivula, K.; Guijarro, N. Insights into the interfacial carrier behaviour of copper ferrite (CuFe<sub>2</sub>O<sub>4</sub>) photoanodes for solar water oxidation. *J. Mater. Chem. A*, **2019**, *7*, 1669–1677.
55. Ruiz Preciado, M. A.; Kassiba, A.; Morales-Acevedo, A.; Makowska-Janusik, M. Vibrational and electronic peculiarities of NiTiO<sub>3</sub> nanostructures inferred from first principle calculations. *RSC Adv.*, **2015**, *5*, 17396–17404.
56. Rudan, M. *Physics of Semiconductor Devices*, 2015.
57. Xu, Q.; Zhang, L.; Yu, J.; Wageh, S.; Al-Ghamdi, A. A.; Jaroniec, M. Direct Z-scheme photocatalysts: Principles, synthesis, and applications. *Mater. Today*, **2018**, *21*, 1042–1063.
58. Glover, E. N. K.; Ellington, S. G.; Sankar, G.; Palgrave, R. G. The nature and effects of rhodium and antimony dopants on the electronic structure of TiO<sub>2</sub>: towards design of Z-scheme photocatalysts. *J. Mater. Chem. A*, **2016**, *4*, 6946–6954.
59. Low, J.; Dai, B.; Tong, T.; Jiang C.; Yu, J. In Situ Irradiated X - Ray Photoelectron Spectroscopy Investigation on a Direct Z-Scheme TiO<sub>2</sub>/CdS Composite Film Photocatalyst. *Adv. Mater.*, **2019**, *31*, 1802981.
60. Yu, W.; Zhang, S.; Chen, J.; Xia, P.; Richter, M. H.; Chen, L.; Xu, W.; Jin, J.; Chen, S.; Peng, T. Biomimetic Z-scheme photocatalyst with a tandem solid-state electron flow catalyzing H<sub>2</sub> evolution. *J. Mater. Chem. A*, **2018**, *6*, 15668–15674.
- S1. Hu, S.; Li, F.; Fan Z.; Gui, J. Improved photocatalytic hydrogen production property over Ni/NiO/N–TiO<sub>2-x</sub> heterojunction nanocomposite prepared by NH<sub>3</sub> plasma treatment. *J. Power Sources*, **2014**, *250*, 30–39.
- S2. Yu, J.; Hai Y.; Cheng, B. Enhanced Photocatalytic H<sub>2</sub>-Production Activity of TiO<sub>2</sub> by Ni(OH)<sub>2</sub> Cluster Modification. *J. Phys. Chem. C*, **2011**, *115*, 4953–4958.
- S3. Li, L.; Cheng, B.; Wang Y.; Yu, J. Enhanced photocatalytic H<sub>2</sub>-production activity of bicomponent NiO/TiO<sub>2</sub> composite nanofibers. *J. Colloid Interface Sci.*, **2015**, *449*, 115–121.
- S4. Wei, Y.; Cheng, G.; Xiong, J.; Xu, F.; Chen, R. Positive Ni(HCO<sub>3</sub>)<sub>2</sub> as a Novel Cocatalyst for Boosting the Photocatalytic Hydrogen Evolution Capability of Mesoporous TiO<sub>2</sub> Nanocrystals. *ACS Sustain. Chem. Eng.*, **2017**, *5*, 5027–5038.
- S5. Wang, W.; Liu, S.; Nie, L.; Cheng, B.; Yu, J. Enhanced photocatalytic H<sub>2</sub>-production activity of TiO<sub>2</sub> using Ni(NO<sub>3</sub>)<sub>2</sub> as an additive. *Phys. Chem. Chem. Phys.*, **2013**, *15*, 12033–12039.
- S6. Li, L.; Cheng, B.; Wang, Y.; Yu, J. Enhanced photocatalytic H<sub>2</sub>-production activity of bicomponent NiO/TiO<sub>2</sub> composite nanofibers. *J. Colloid. Interf. Sci.*, **2015**, *449*, 115–121.
- S7. Rawool, A.; Pai, M. R.; Banerjee, A. M.; Arya, A.; Ningthoujam, R.; Tewari, R.; Rao, R.; Chalke, B.; Ayyub P.; Tripathi, A. pn Heterojunctions in NiO:TiO<sub>2</sub> composites with type-II band alignment assisting sunlight driven photocatalytic H<sub>2</sub> generation. *Appl. Catal. B Environ.*, **2018**, *221*, 443–458.

## Chapter 3 A Direct Z-Scheme for the Photocatalytic Hydrogen Production from a Water Ethanol Mixture on CoTiO<sub>3</sub>/TiO<sub>2</sub> Heterostructures



### 3.1 Abstract

Photocatalytic  $H_2$  evolution from ethanol dehydrogenation is a convenient strategy to store solar energy in a highly valuable fuel with potential zero net  $\text{CO}_2$  balance. Herein, we report on the synthesis of  $\text{CoTiO}_3/\text{TiO}_2$  composite catalysts with controlled amounts of highly distributed  $\text{CoTiO}_3$  nanodomains for photocatalytic ethanol dehydrogenation. We demonstrate these materials to provide outstanding hydrogen evolution rates under UV and visible illumination. The origin of this enhanced activity is extensively analyzed. In contrast to previous assumptions, UV–vis absorption spectra and ultraviolet photoelectron spectroscopy (UPS) prove  $\text{CoTiO}_3/\text{TiO}_2$  heterostructures to have a type II band alignment, with the CB minimum of  $\text{CoTiO}_3$

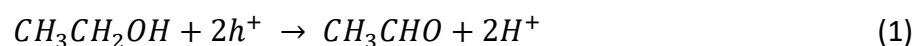
below the  $\text{H}_2/\text{H}^+$  energy level. Additional steady-state photoluminescence (PL) spectra, time-resolved PL spectra (TRPLS), and electrochemical characterization prove such heterostructures to result in enlarged life times of the photogenerated charge carriers. These experimental evidences point toward a direct Z-scheme as the mechanism enabling the high photocatalytic activity of  $\text{CoTiO}_3/\text{TiO}_2$  composites toward ethanol dehydrogenation. In addition, we probe small changes of temperature to strongly modify the photocatalytic activity of the materials tested, which could be used to further promote performance in a solar thermo-photocatalytic reactor.

### 3.2 Introduction

Hydrogen is regarded as one of the most convenient energy vectors owing to its abundance, cleanness, and high energy density. However, as there is no natural source of molecular hydrogen,  $\text{H}_2$  needs to be produced from chemical compounds such as water, hydrocarbons, or alcohols, which requires a supply of energy. Among the possible sources of hydrogen, ethanol is particularly suitable both thermodynamically and in terms of net  $\text{CO}_2$  emissions. The production of hydrogen from ethanol is less energetically demanding than from water splitting, and the product can be more easily separated. At the same time, ethanol is the most common liquid fuel derived from biomass, being worldwide-produced in huge quantities ( $\sim 10^{11}$  liters annually) by the fermentation of sugars from corn starch and sugar cane and from large volume low value biomass like lignocellulose and organic waste.<sup>1-4</sup> Ethanol biosourcing compensates  $\text{CO}_2$  released during combustion through its capture during photosynthesis, leading to a near zero net  $\text{CO}_2$  footprint. In addition, being liquid at ambient temperature, ethanol can be easily stored and transported to the point that the already established infrastructure for ethanol production and distribution makes it a very convenient precursor of other fuels, including  $\text{H}_2$  and higher alcohols.<sup>4,5</sup>

In terms of source of energy, the use of solar energy to generate fuels and particularly hydrogen is especially attractive due to its abundance and ubiquitous availability at zero cost. From another point of view, the production of solar fuels can be regarded as a suitable strategy to store this intermittent form of energy.<sup>6,7</sup>

Photocatalysts allow the production of molecular hydrogen from ethanol dehydrogenation using solar energy as unique energy input.<sup>1</sup> In the simplest scenario, ethanol can be photocatalytically dehydrogenated at ambient pressure and temperature, yielding molecular hydrogen and acetaldehyde, and releasing no CO<sub>2</sub>:



Acetaldehyde is a particularly versatile chemical precursor extensively used by the chemical industry because the aldehyde moiety provides a functional handle that, through different reaction pathways, can be used to yield a range of products, including upgraded fuels as well as large volume commodity chemicals such as acetic acid or butadiene, among others.<sup>8-10</sup> Besides, this dehydrogenation reaction is also the limiting step in the synthesis of higher alcohols through the Guerbet reaction. Thus, separating it from the rest of the process could allow not only saving energy but also improving product selectivity by reducing the process maximum temperature.<sup>4, 11, 12</sup>

To engineer an efficient photocatalyst for solar energy storage into fuels it is necessary to ensure an effective absorbance of the solar radiation, long lasting photogenerated charge carriers, which generally requires a means of charge separation, and a proper surface interaction with all the involved chemical species. To satisfy these demanding requirements, composite materials are generally used to extend the range of spectrum absorption, drive charge separation and offer additional adsorption/reaction sites. In many systems it is found that the photocatalytic reaction is most likely occurring at the interface between two different materials, what makes the engineering of this interface particularly important.<sup>7</sup> To minimize recombination sites and defects, the interphase can be optimized by the direct growth of one phase from the surface of the other, or even more conveniently, by the segregation of nanodomains of the two phases from a common precursor material. To maximize the interface and minimize diffusion and side reactions of the involved species, a nanoscale dispersion of the different phases is required.

TiO<sub>2</sub> is the prototype photocatalyst due to its outstanding optoelectronic properties,

natural abundance, high photocorrosion resilience, lack of toxicity and low cost.<sup>13, 14</sup> However, TiO<sub>2</sub> practical application is hampered by its large bandgap, that limits the range of solar spectra used.<sup>15, 16</sup> The doping of titania with different elements and its combination with light absorbers have been demonstrated effective in extending the range of solar spectrum absorbed. But this improvement generally comes at the cost of decreasing internal quantum efficiencies due to increased charge carrier recombination, resulting in a limited overall improvement of the photon-to-fuel energy conversion efficiency.

Cobalt titanate (CoTiO<sub>3</sub>) is a narrow band gap oxide semiconductor with a ABO<sub>3</sub> perovskite crystal structure, large carrier mobility, excellent stability, and high absorption coefficient.<sup>17-19</sup> In combination with graphitic carbon nitride (g-C<sub>3</sub>N<sub>4</sub>) and Pt, it has been recently explored for photocatalytic hydrogen generation through a direct Z-scheme, where holes photogenerated in CoTiO<sub>3</sub> participate in the oxidation reaction, electrons photogenerated in the g-C<sub>3</sub>N<sub>4</sub> drive the reduction reaction, and at the interphase of the two materials electrons photogenerated in CoTiO<sub>3</sub> recombine with holes generated in g-C<sub>3</sub>N<sub>4</sub>.<sup>17</sup> CoTiO<sub>3</sub>/TiO<sub>2</sub> composites have also been synthesized and used in multiple applications. In terms of synthesis, Yi et al. reported TiO<sub>2</sub>@CoTiO<sub>3</sub> core-shell nanowires grown in a two-step hydrothermal process at 180 °C.<sup>20</sup> Zou et al. reported the production of TiO<sub>2</sub>@CoTiO<sub>3</sub> core-shell structures by a simple precipitation method and the posterior annealing of the products at a temperature in the range 600 °C to 1000 °C for 1 h.<sup>19</sup> Sarkar et al. hydrothermally synthesized TiO<sub>2</sub> and mixed it with a CTAB-solution of cobalt nitrate. The obtained dried mixture was subsequently calcined at 550 °C for 3 h in air to produce CoTiO<sub>3</sub>/TiO<sub>2</sub> composites.<sup>22</sup> In terms of applications, CoTiO<sub>3</sub>/TiO<sub>2</sub> composites have been used for photoelectrochemical water splitting;<sup>20</sup> photocatalytic dye degradation,<sup>21</sup> oxidative dehydrogenation of cyclohexane;<sup>22</sup> dry reforming of methane;<sup>23</sup> peroxymonosulfate activation and metronidazole degradation;<sup>24</sup> resistive humidity sensing;<sup>25</sup> electrochemical sensing of dopamine;<sup>26</sup> and anode in lithium ion batteries,<sup>27</sup> but surprisingly CoTiO<sub>3</sub>/TiO<sub>2</sub> composites have not been thoroughly tested as photocatalysts for H<sub>2</sub> production from bioethanol dehydrogenation.

Herein,  $\text{CoTiO}_3/\text{TiO}_2$  photocatalysts with different  $\text{CoTiO}_3$  amounts are produced by phase segregation during annealing of a Co-doped  $\text{TiO}_2$  precursor prepared by hydrothermal reaction.  $\text{CoTiO}_3/\text{TiO}_2$  photocatalysts were tested for hydrogen generation from ethanol dehydration in gas phase. A 10% alcohol solution in water was used owing to its optimized activity and its proximity to commercial bioethanol, produced in the form of diluted aqueous solution from biomass fermentation. Notice that using aqueous solutions, thus avoiding the costly ethanol separation and purification, is fundamental for the cost-effectiveness of the process.<sup>2, 3, 5</sup>

### 3.3 Experimental Section

**Chemicals:** Titanium (IV) isopropoxide (97%), hexadecylamine (HDA, 90%) and ammonium hydroxide (28-30%) were ordered from Sigma Aldrich. Ethanol (96%) was purchased from PanReac AppliChem ITW Reagents. Cobalt (II) nitrate hexahydrate (98%) was purchased from Fluka.

**Synthesis of precursor photocatalysts ( $\text{TiO}_2$ ,  $\text{CoTiO}_3$  and  $\text{TiO}_2:\text{Co}$ ):** To produce  $\text{TiO}_2:\text{Co}$  precursor particles, first 0.45 g HDA was mixed with 40 mL ethanol at room temperature and stirred for 5 mins. Then, an accurate quantity of  $\text{Co}(\text{NO}_3)_2 \cdot 6\text{H}_2\text{O}$  (11.3, 22.5, 45, and 112.5 to obtain 0.5, 1, 2, and 5 mol% concentrations, respectively) was introduced under stirring for another 5 min. Then, 2.3 mL titanium isopropoxide was added dropwise and kept stirring 16 h at ambient temperature. The mixture was washed 3 times with ethanol by centrifuging to collect the final product. The product was subsequently mixed with a solution of 20 mL of ethanol, 10 mL of MiliQ water and 2.2 mL of ammonium hydroxide. Then it was kept for 16 h without stirring. Afterward, the mixture was placed in an autoclave reactor with a Teflon liner (50 mL) and maintained at 170 °C for 14 h. Afterwards, it was cooled down to room temperature and the product was washed three times with ethanol, then dry them at 60 °C overnight. Reference  $\text{TiO}_2$  and  $\text{CoTiO}_3$  materials were produced in the same way, but using no cobalt nitrate for the former and a 1:1 molar ratio of cobalt nitrate and titanium isopropoxide for the later.

**Preparation of annealed photocatalysts ( $\text{TiO}_2$ ,  $\text{CoTiO}_3$  and  $\text{CoTiO}_3/\text{TiO}_2$ ):**  $\text{CoTiO}_3/\text{TiO}_2$

(0.5, 1, 2 and 5 at%) were obtained by annealing the corresponding dried TiO<sub>2</sub>:Co precursors obtained by hydrothermal reaction at 650 °C for 8 h with synthetic air flow. Reference TiO<sub>2</sub> and CoTiO<sub>3</sub> materials were also obtained by annealing dried samples at 650 °C for 8 h with synthetic air flow.

**Characterization:** The particle morphology and size were analyzed using transmission electron microscopy (TEM) in a ZEISS LIBRA 120, working at 120 KeV. High angle annular dark field (HAADF) scanning TEM and high-resolution TEM (HRTEM) analysis were performed on a FEI Tecnai F20 field emission gun microscope operated at 200 keV combined with a Gatan Quantum electron energy-loss spectroscopy (EELS) detector. Scanning electron microscopy (SEM) was conducted using a ZEISS Auriga microscope. X-ray diffraction analyses (XRD) were carried out on a Bruker D8-Advance X-ray diffractometer (2 $\theta$ : 20°-80°, scanning rate was set to 5°/min). The optical properties of photocatalysts were evaluated by UV/Visible diffuse spectroscopy (UV-Vis-NIR Shimadzu 3600). X-ray photoelectron spectroscopy (XPS) was conducted with an Al anode XR50 source on a SPECS equipment using a Phoibos 150 MCD-9 detector (150 W). Steady-state photoluminescence (PL) spectra were conducted by a high-resolution photoluminescence spectrofluorometer (Horiba Jobin Yvon Fluorolog-3). For the time-resolved photoluminescence spectroscopy (TRPL) measurements, a nanosecond LED with 350 nm peak wavelength (Horiba NanoLED N-390, pulse width < 1.3 ns) was applied to excite the samples. TRPL decay was resolved at 400 nm. Average lifetimes were obtained by fitting the TPPL spectra with DAS6 software (Horiba). Transient photocurrent (TPC) and electrochemical impedance spectroscopy (EIS) analyses were conducted using a Bio-Logic SP-300. Photocatalysts were coated on transparent conducting substrates (FTO) and were used as working electrode. Ag/AgCl was used as reference electrode and a Pt wire as counter electrode. For impedance characterization, a sinusoidal potential was applied to the working electrode with an amplitude of 25 mV and a frequency in the range 100 kHz - 50 mHz. Impedance response fitting was conducted using ZView (Scribner Associates). In TPC measurements, the same three-electrode configuration was employed and a Xenon arc lamp (Newport, 450 W) was used as light source. UV photoelectron Spectroscopy (UPS) measurements were performed on a Thermo Fisher Scientific Escalab 250Xi.

Nitrogen adsorption–desorption isotherms of the samples were obtained on a surface area analyzer (Micromeritics Tristar II 3020) at 77 K.

**Photocatalytic Hydrogen Evolution Measurements:** A cellulose paper impregnated with the photocatalyst (2.0 mg) was held inside a photocatalytic reactor equipped with  $365 \pm 5$  nm UV LEDs (Figure S21). Light irradiation at the sample position was  $79.1 \text{ mW}\cdot\text{cm}^{-2}$ . Saturated Ar gas stream was prepared by bubbling Ar ( $20 \text{ mL}\cdot\text{min}^{-1}$ ) through a Dreschel bottle containing a water-ethanol vapour mixture with a molar ratio 9. The photoreactor exit was analysed online by gas chromatography equipped with Plot U, MS 5 Å, and Stabilwax columns every 4 min. Saturated Ar was purged into system ( $20 \text{ mL}\cdot\text{min}^{-1}$ , 30 min) to remove oxygen before performing the experiment. The UV-visible light source contained two LEDs emitting at  $372 \pm 5$  nm and two LEDs emitting visible light (correlated color temperature 6099 K, color rendering index 74) Figure S21. In this system light irradiation at the sample position was  $11.2 \pm 0.5 \text{ mW}\cdot\text{cm}^{-2}$  for UV light and  $0.017 \pm 0.005 \text{ mW}\cdot\text{cm}^{-2}$  for visible light.<sup>32, 50, 51</sup>

The AQY was estimated using the following equation:

$$\text{AQY} = \frac{2n_{\text{H}_2}}{n_p} \cdot 100 = \frac{2nN_A}{E_T/E_p} \cdot 100 \quad (3)$$

where  $n_{\text{H}_2}$  is the number of evolved hydrogen molecules and  $n_p$  the number of incident photons reaching the catalyst. The number of incident photons can be calculated by  $n_p = E_T/E_p$ , where  $E_T$  is the total energy reaching the catalyst and  $E_p$  is the energy of a photon.  $E_T$  can be calculated by  $E_T = PSt$ , where  $P$  ( $\text{W}\cdot\text{m}^{-2}$ ) is the power density of the incident monochromatic light,  $S$  ( $\text{m}^2$ ) is the irradiation area and  $t$  (s) is the duration of the incident light exposure.  $E_p$  can be calculated by  $E_p = hc/\lambda$ , where  $h$  is the Planck's constant,  $c$  the speed of light and  $\lambda$  (m) is the wavelength of the incident monochromatic light. The number of hydrogen molecules can be calculated as  $n_{\text{H}_2} = nN_A$ , where  $n$  is  $\text{H}_2$  moles evolved during the time of light exposure ( $t$ ), and  $N_A$  is the Avogadro constant. In our experimental conditions, the wavelength of the incident light was  $\lambda = 365$  nm, the power density of the incident light at the paper surface was  $P = 79.1 \text{ mW}\cdot\text{cm}^{-2}$  and the irradiation area were  $S = \pi R^2 = 3.14 \times 0.75^2 = 1.77 \text{ cm}^2$ .<sup>32, 50</sup>

### 3.4 Result and discussion

#### Photocatalyst Characterization.

Cobalt-doped titania ( $\text{TiO}_2\text{:Co}$ ) nanopowders with different Co amounts were obtained by the simultaneous hydrothermal reaction of titanium(IV) isopropoxide and cobalt(II) nitrate at 170 °C for 14 h. XRD patterns of these materials only displayed the anatase  $\text{TiO}_2$  crystallographic phase (Figure 1). Co introduction resulted in a shift of the anatase diffraction peaks to lower angles, which indicated the incorporation of Co inside the  $\text{TiO}_2$  lattice structure. Energy-dispersive X-ray (EDX) analysis showed the  $\text{TiO}_2\text{:Co}$  nanopowders to contain Co/Ti atomic ratios above the nominal values, which evidenced a better reaction yield of cobalt(II) nitrate than titanium(IV) isopropoxide (Table 1). TEM micrographs (Figure 4b and Figure 2) displayed most  $\text{TiO}_2\text{:Co}$  particles to have an elongated geometry, with lengths in the range of 100– 200 nm and thicknesses around 30–60 nm. In the absence of hexadecylamine in the precursor solution, much more aggregated materials were obtained (Figure 3).

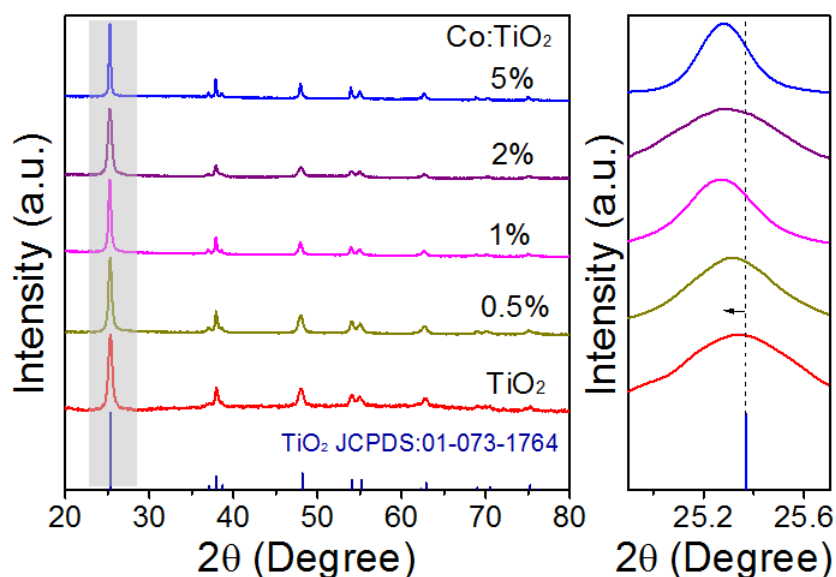


**Figure 1.** XRD patterns of as-synthesized  $\text{TiO}_2$  and  $\text{TiO}_2\text{:Co}$  (1%, 2%, 5%) particles.

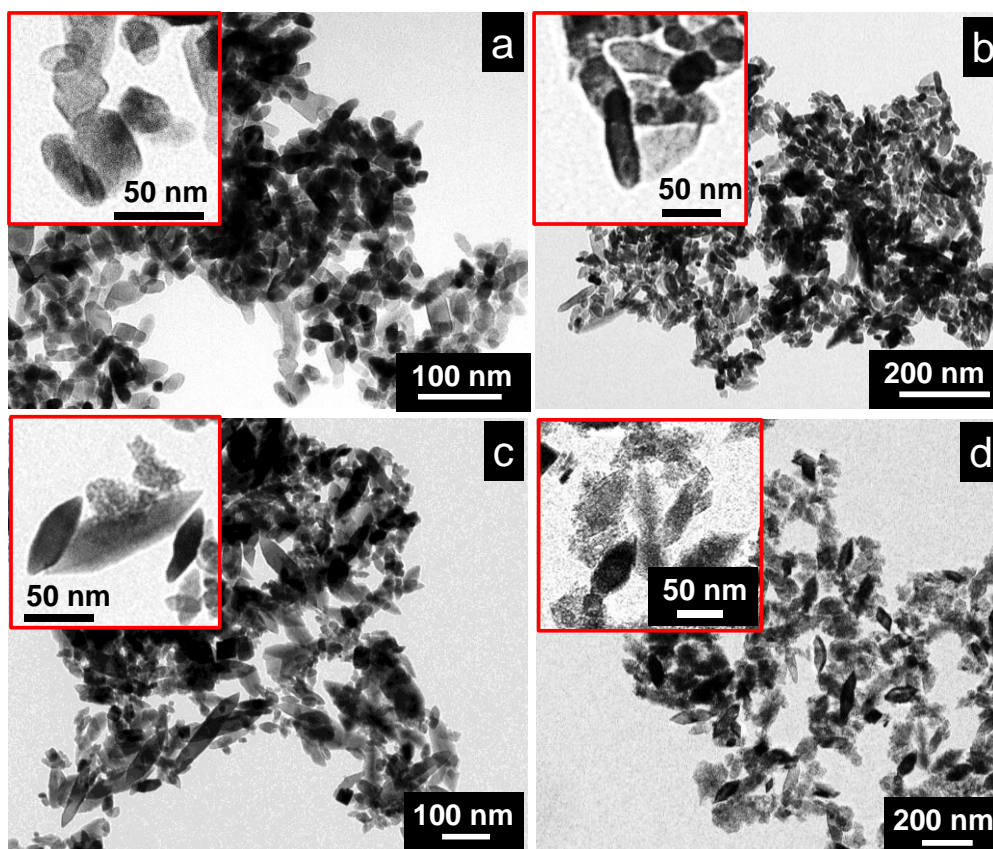


**Figure 2.** Representative TEM micrographs of as-synthesized TiO<sub>2</sub>:Co particles with different Co nominal ratios: (a) 0.5%, (b) 1%, (c) 2%, and (d) 5%.

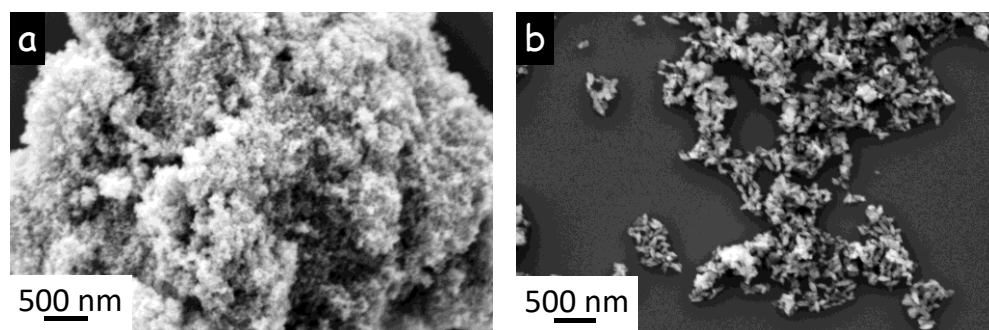


**Figure 3.** (a) Representative SEM micrographs of TiO<sub>2</sub>:Co (5%) obtained without HDA (a) and with HDA (b).

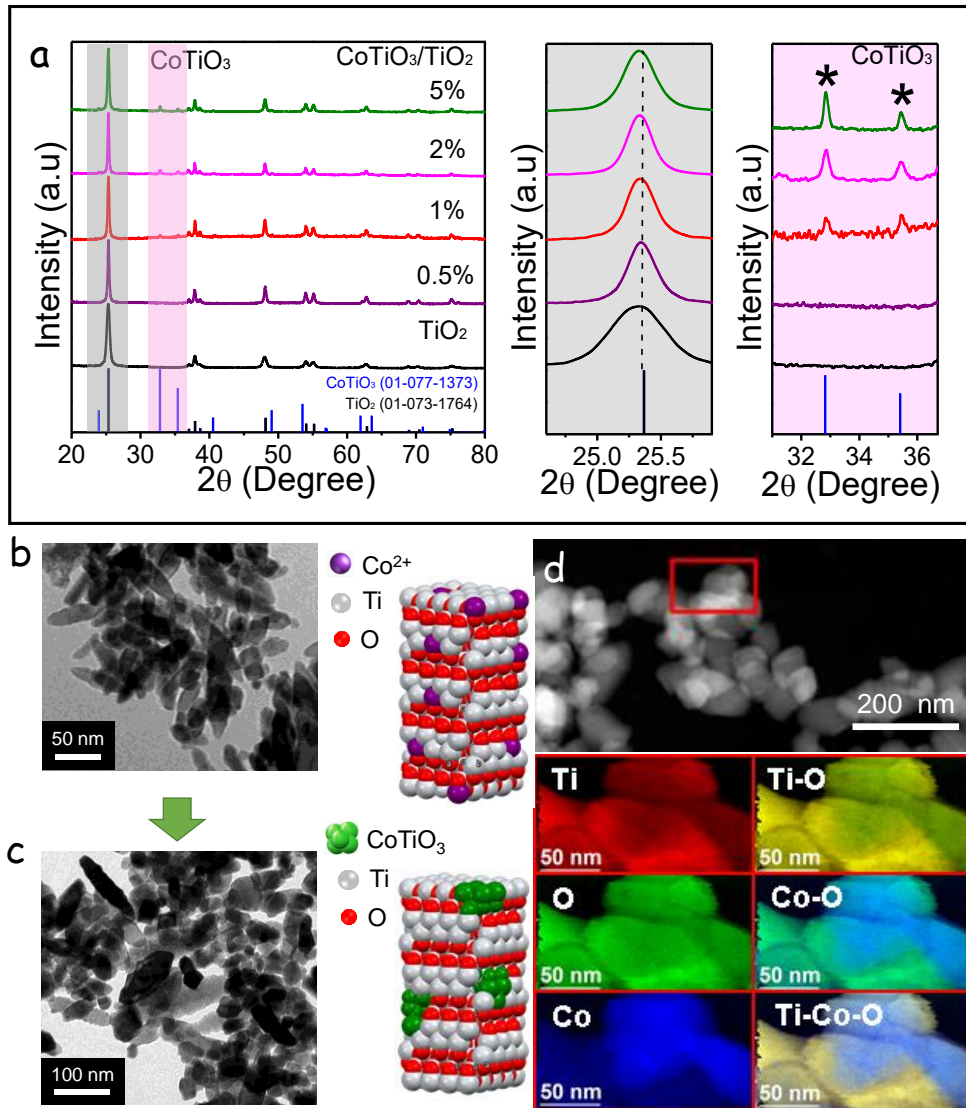


**Figure 4.** (a) XRD patterns of CoTiO<sub>3</sub>/TiO<sub>2</sub> (0, 1, 2, 5%). (b, c) TEM micrograph and atomic scheme of the precursor TiO<sub>2</sub>:Co (1%) nanopowder (b) and the CoTiO<sub>3</sub>/TiO<sub>2</sub> (1%) nanocomposite (c). (d) STEM image of a CoTiO<sub>3</sub>/TiO<sub>2</sub> composite and corresponding EELS elemental maps for Ti, O, Co and its combinations as noted in each map.

**Table 1.** Elemental analysis of TiO<sub>2</sub>, TiO<sub>2</sub>:Co and CoTiO<sub>3</sub>/TiO<sub>2</sub> samples.

Catalysts	EDX		XPS	
	Ti (at%)	Co (at%)	Ti (at%)	Co (at%)
TiO <sub>2</sub>	100	0		
TiO <sub>2</sub> :Co (1%)	96	4		
TiO <sub>2</sub> :Co (2%)	94	6		
CoTiO <sub>3</sub> /TiO <sub>2</sub> (1%)	96	4	97	3
CoTiO <sub>3</sub> /TiO <sub>2</sub> (2%)	94	6	96	4
CoTiO <sub>3</sub> /TiO <sub>2</sub> (5%)	90	10	92	8

Co-doped TiO<sub>2</sub> nanopowders were used as precursors to produce Ti/Co oxide composites. Precursor TiO<sub>2</sub>:Co nanopowders were annealed at 650 °C for 8 h with synthetic air flow (Figure 5). XRD patterns of the annealed materials (Figure 4a) displayed the characteristic peaks of both anatase TiO<sub>2</sub> (JCPDS no. 01-073-1764)<sup>28</sup> and CoTiO<sub>3</sub> (JCPDS no. 01-077-1373).<sup>29</sup> As expected, when increasing the nominal Co content in the precursor material, the relative intensity of the CoTiO<sub>3</sub> diffraction peaks became stronger (Figure 4a). In addition, the shift of the anatase peaks detected in the precursor TiO<sub>2</sub>:Co materials disappeared, indicating the segregation of Co ions to form the CoTiO<sub>3</sub> phase. TEM analysis showed the particles within the annealed powder to just partially preserve the elongated geometry of the precursor (Figure 4c and Figure 6). Elemental maps showed the CoTiO<sub>3</sub> phase to be evenly distributed throughout the CoTiO<sub>3</sub>/TiO<sub>2</sub> nanocomposite within crystal domains of a similar size as those of TiO<sub>2</sub> (Figure 4d and Figures 7). The composition of the materials was analyzed by EDX, and it is displayed in Table 1. The amount of Co obtained in the CoTiO<sub>3</sub>/TiO<sub>2</sub> nanocomposite was similar to that obtained in the precursor TiO<sub>2</sub>:Co, i.e., above the nominal Co concentration introduced. Still, we will use the nominal Co concentration to refer to the different samples.

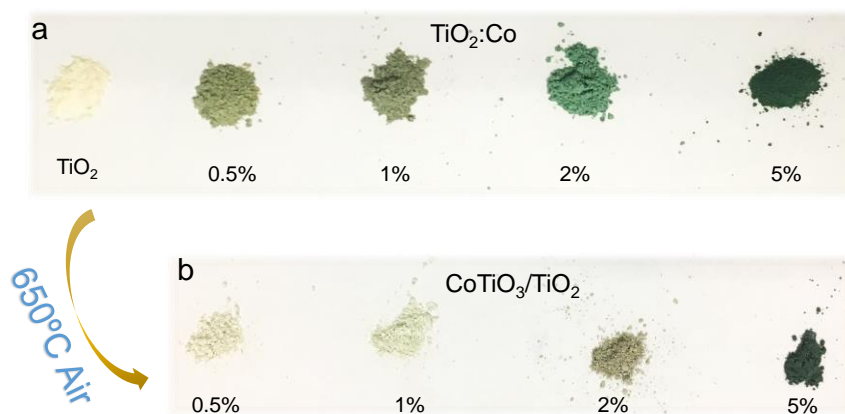


**Figure 5.** Optical images of TiO<sub>2</sub>:Co nanopowder before annealing (a) and CoTiO<sub>3</sub>/TiO<sub>2</sub> powders after annealing (b).

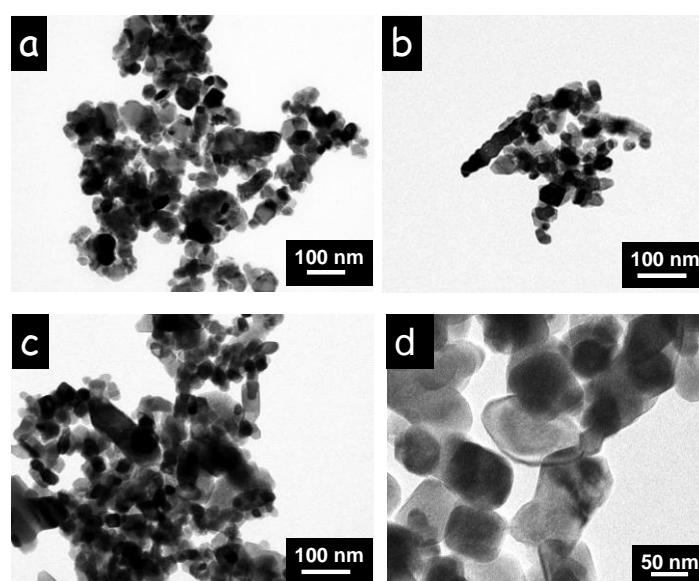


**Figure 6.** Representative TEM micrographs of CoTiO<sub>3</sub>/TiO<sub>2</sub>: (a) 0.5%; (b) 1%; (c) 2%; (d) 5%.

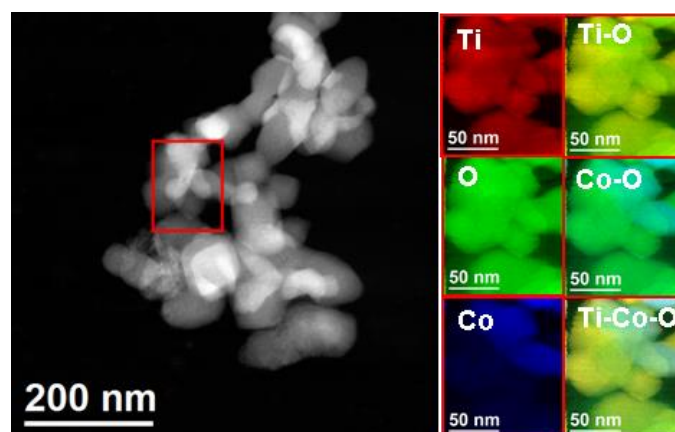


**Figure 7.** EELS chemical composition maps from the red squared area in the STEM micrograph obtained from CoTiO<sub>3</sub>/TiO<sub>2</sub> (1%). Individual Ti L<sub>2,3</sub>-edge at 456 eV (red), O K-edge at 532 eV (green) and Co L<sub>2,3</sub>-edge at 779 eV, as well as its composites.

UV-vis spectroscopy showed the optical band gap of the composites to decrease with the amount of Co introduced, from 2.8 eV for CoTiO<sub>3</sub>/TiO<sub>2</sub> (0.5%) to 2.35 eV for CoTiO<sub>3</sub>/TiO<sub>2</sub> (5%), as shown in Figure 8. Nitrogen adsorption-desorption isotherms of the composite materials are displayed in Figure 9. The Brunauer-Emmett-Teller (BET) specific surface area of the material ranged from 18.8 m<sup>2</sup>/g for CoTiO<sub>3</sub>/TiO<sub>2</sub> (1%) to 30.8 m<sup>2</sup>/g for CoTiO<sub>3</sub>/TiO<sub>2</sub> (5%).

As reference materials, pure TiO<sub>2</sub> and CoTiO<sub>3</sub> powders were synthesized by decomposition of titanium(IV) isopropoxide and proper amounts of titanium(IV) isopropoxide and cobalt(II) nitrate, respectively (see details in the Experimental Section). XRD patterns of the annealed samples (Figure 10a) displayed the pure anatase TiO<sub>2</sub> and CoTiO<sub>3</sub> phases. The band gaps of TiO<sub>2</sub> and CoTiO<sub>3</sub>, estimated via the Tauc plot from the UV-visible absorption spectra,<sup>30</sup> were 3.0 and 2.3 eV, respectively (Figure 10b and Figure 8). TEM/HRTEM micrographs of TiO<sub>2</sub> and CoTiO<sub>3</sub> nanopowders showed them to be composed of irregular shaped particle with average sizes of ca. 30 and 60 nm, respectively (Figures 11).

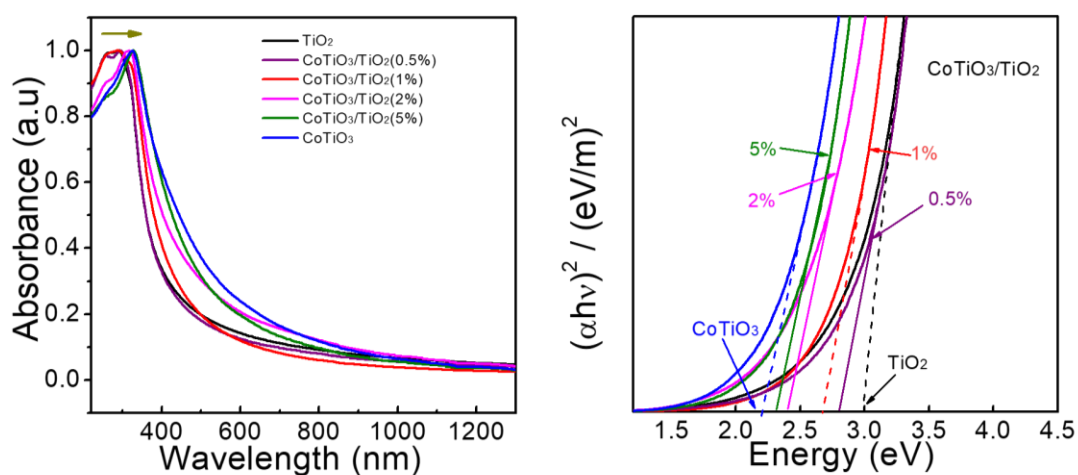


**Figure 8.** UV-vis spectra and Kubelka-Munk plot for TiO<sub>2</sub>, CoTiO<sub>3</sub>, CoTiO<sub>3</sub>/TiO<sub>2</sub> (0.5, 1, 2, 5%) and CoTiO<sub>3</sub>/TiO<sub>2</sub> samples including a linear fit (dashed lines) to determine the optical band gap. The band gaps of CoTiO<sub>3</sub>/TiO<sub>2</sub>(0.5, 1, 2, 5%) are 2.8 eV, 2.7 eV, 2.4 eV and 2.35 eV, respectively.

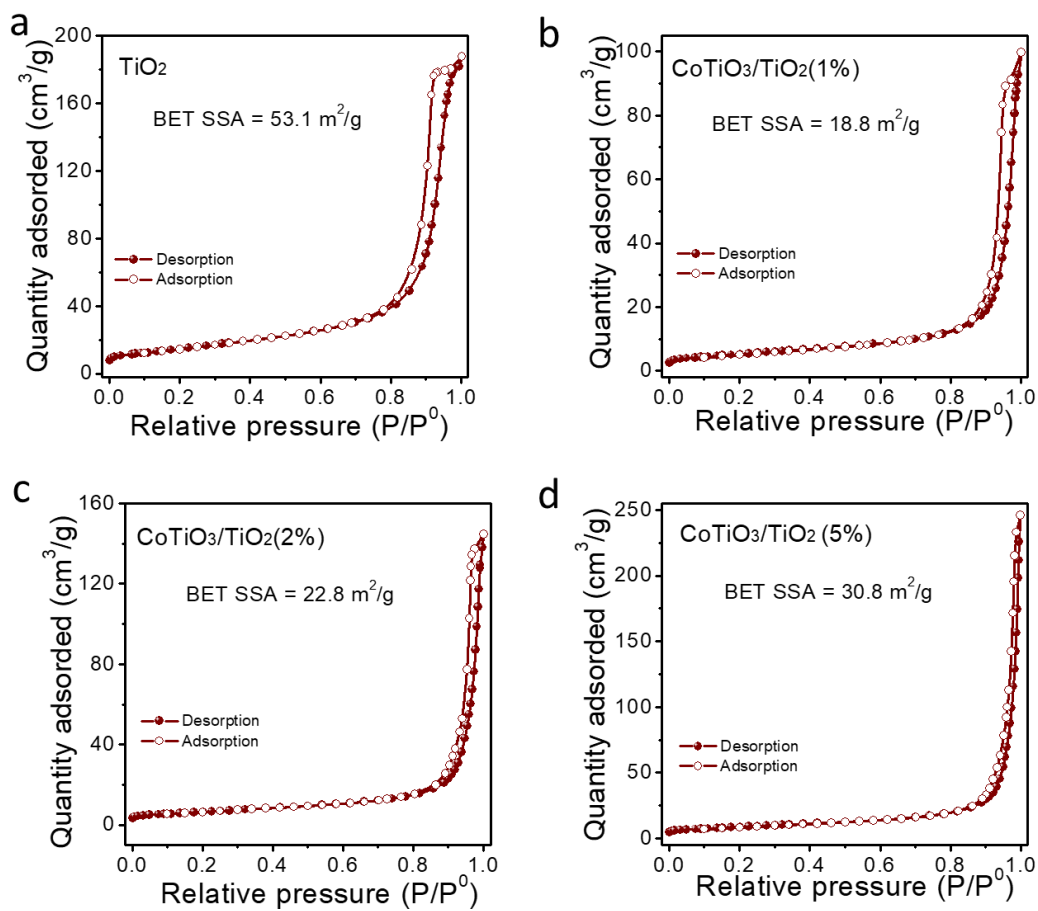


**Figure 9.** Nitrogen adsorption (open symbols) and desorption (solid symbols) isotherms measured from (a)  $\text{TiO}_2$ , (b)  $\text{CoTiO}_3/\text{TiO}_2$  (1%), (c)  $\text{CoTiO}_3/\text{TiO}_2$  (2%), and (d)  $\text{CoTiO}_3/\text{TiO}_2$  (5%) at 77 K. The calculated BET specific surface areas (SSA) are specified within each graph.

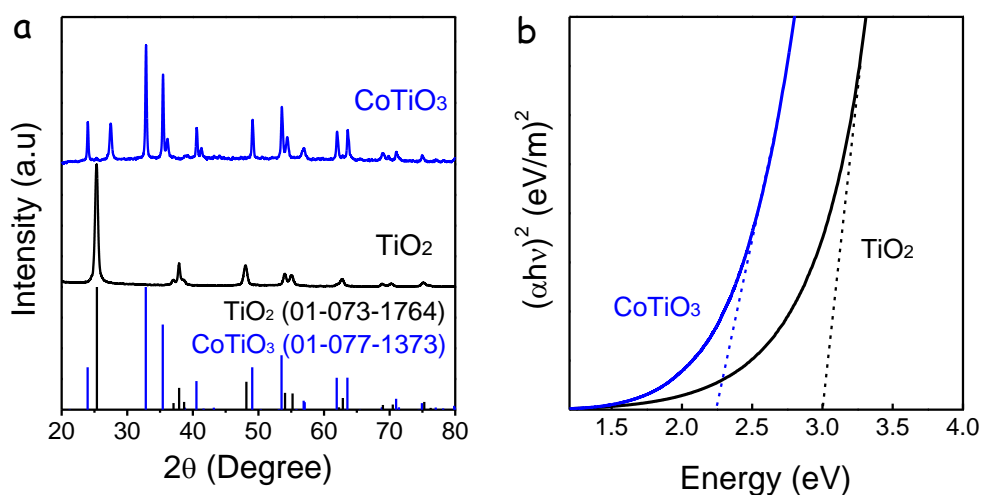


**Figure 10.** (a) XRD patterns of  $\text{TiO}_2$  and  $\text{CoTiO}_3$ , (b) Kubelka-Munk function for  $\text{TiO}_2$  and  $\text{CoTiO}_3$  with a linear fit to determine the band gap energy.

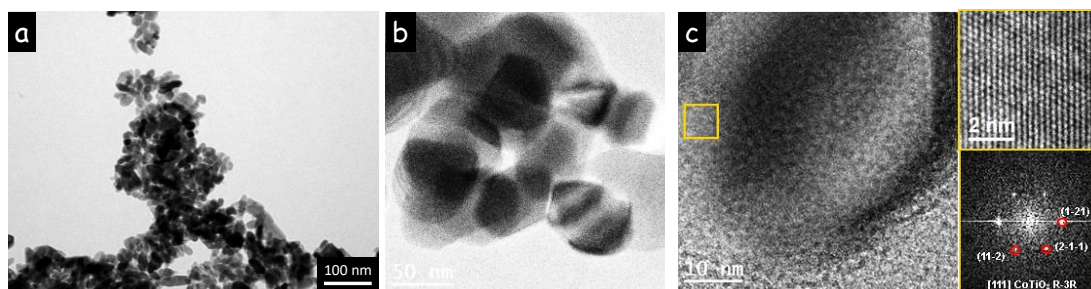
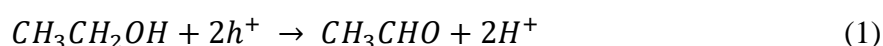


**Figure 11.** Representative TEM micrograph of TiO<sub>2</sub> nanoparticles. (b) TEM micrograph of CoTiO<sub>3</sub> nanoparticles. (c) HRTEM micrograph of CoTiO<sub>3</sub>, detail of the yellow squared region and its corresponding power spectrum.

### Photocatalytic Hydrogen Production

Figure 12a,b displays the UV photocatalytic activity of CoTiO<sub>3</sub>/TiO<sub>2</sub> nanopowders with different amounts of CoTiO<sub>3</sub> in the production of hydrogen using a 10% ethanol solution in water (see the Experimental Section for details). The activities of the reference TiO<sub>2</sub> and CoTiO<sub>3</sub> catalysts and that of the Co-doped TiO<sub>2</sub> were also measured and displayed. The products of the reaction were analyzed online by gas chromatography with three columns for a complete analysis. The only products encountered were hydrogen and acetaldehyde (in addition to the reactants ethanol and water; Figure 13). The molar ratio between hydrogen and acetaldehyde was in all cases 1, demonstrating that the photoproduction of hydrogen originated from the dehydrogenation of ethanol according to the scheme



Indeed, the photoproduction of hydrogen from water–ethanol mixtures has been actually studied in detail in the literature and it has been demonstrated that ethanol is the source of hydrogen.<sup>6</sup> Water is introduced in the reaction mixture to avoid the blockage of the active sites by acetaldehyde, which is known to adsorb strongly on inorganic oxides.<sup>31</sup>

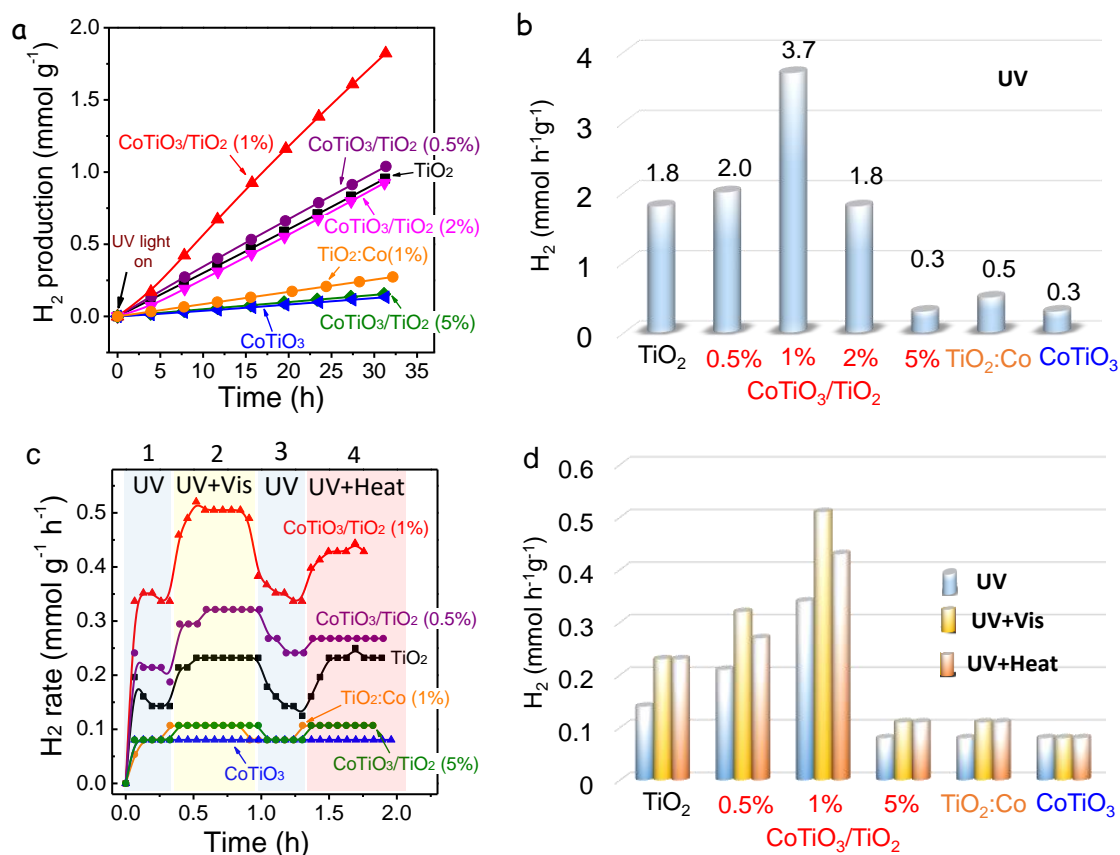


**Figure 12.** (a) Photocatalytic H<sub>2</sub> evolution on TiO<sub>2</sub>, CoTiO<sub>3</sub>/TiO<sub>2</sub> (1, 2, 5%), TiO<sub>2</sub>:Co (1%) and CoTiO<sub>3</sub> under UV light irradiation ( $365 \pm 5$  nm,  $79.1 \pm 0.5$  mW·cm<sup>-2</sup>). (b) HER from data displayed in (a). (c) HER measured from CoTiO<sub>3</sub>/TiO<sub>2</sub> (0.5, 1, 5%), TiO<sub>2</sub>, CoTiO<sub>3</sub>, TiO<sub>2</sub>:Co (1%) under different conditions: 1) UV light irradiation ( $372 \pm 5$  nm,  $11.2 \pm 0.5$  mW·cm<sup>-2</sup>); 2) UV ( $372 \pm 5$  nm,  $11.2 \pm 0.5$  mW·cm<sup>-2</sup>) plus visible light irradiation ( $0.017 \pm 0.005$  mW·cm<sup>-2</sup>); 3) UV light irradiation, 4) UV light irradiation and heating to compensate temperature ( $\sim 34$ - $36$  °C); (d) HER obtained from data displayed in (c).

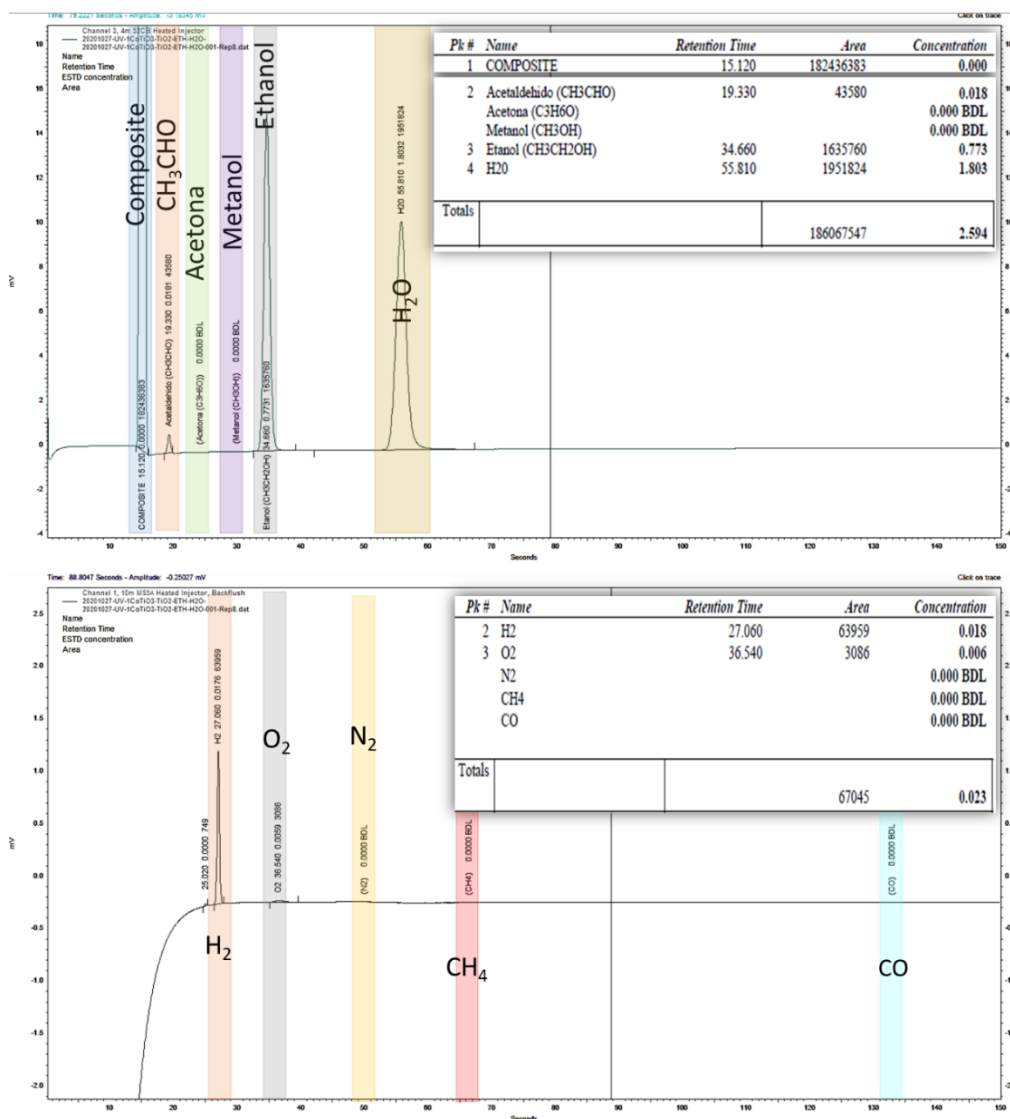


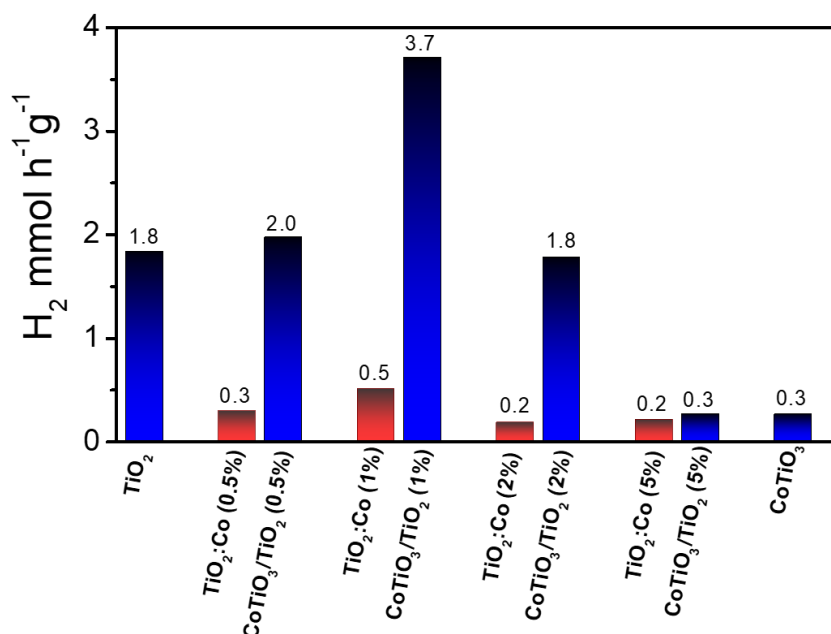
**Figure 13.** Gas chromatography analysis of the products obtained over CoTiO<sub>3</sub>/TiO<sub>2</sub> (1%). The only products are hydrogen and acetaldehyde in a 1:1 molar ratio.

The hydrogen evolution rate (HER) values measured under UV light (365 ± 5 nm) for the reference TiO<sub>2</sub> and CoTiO<sub>3</sub> catalysts were 1.8 and 0.3 mmol h<sup>-1</sup> · g<sup>-1</sup>, respectively. On the other hand, among the series of CoTiO<sub>3</sub>/TiO<sub>2</sub> samples tested, the CoTiO<sub>3</sub>/TiO<sub>2</sub> (1%) photocatalyst exhibited the highest HER, 3.7 mmol h<sup>-1</sup> · g<sup>-1</sup>, 2-fold higher than TiO<sub>2</sub> and a factor of 12 above CoTiO<sub>3</sub>. Under the same conditions, the HER of the TiO<sub>2</sub>:Co (1%) catalyst was just 0.5 mmol h<sup>-1</sup> · g<sup>-1</sup>. Actually, as shown in Figure 14, all the nanocomposites of CoTiO<sub>3</sub>/TiO<sub>2</sub> (0.5, 2, and 5%) displayed a significantly larger HER than those obtained from Co-doped titania, TiO<sub>2</sub>:Co (0.5, 2, and 5%). Figure 15 displays

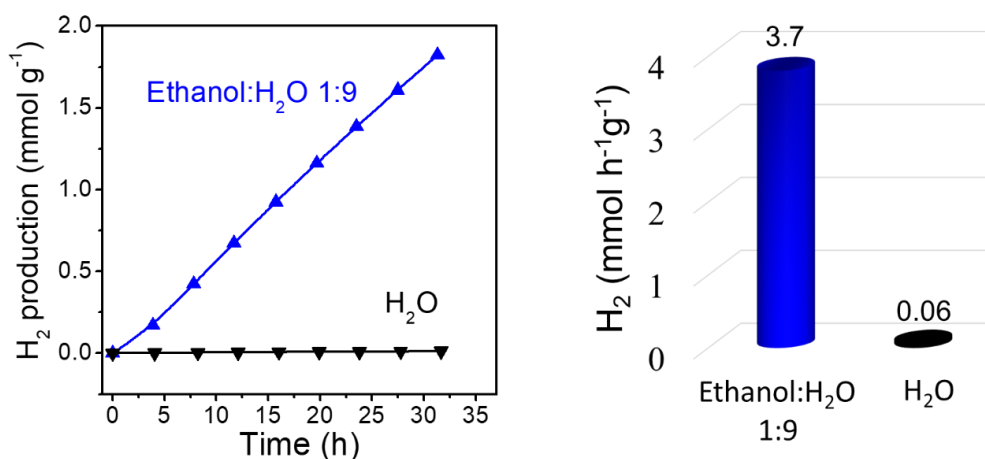
a comparison of the hydrogen evolution rate measured under UV light in pure water and in ethanol:water (1:9). The small amount of hydrogen produced in pure water demonstrates the important role of ethanol as a sacrificial agent. On Table 2, the results obtained from the CoTiO<sub>3</sub>/TiO<sub>2</sub> samples analyzed in the present work are compared with literature values on other Co–Ti systems. The apparent quantum yield (AQY) of CoTiO<sub>3</sub>/TiO<sub>2</sub> (1%), estimated as described in the Experimental Section, was 1.1%, notably above the 0.5% estimated for pure TiO<sub>2</sub> (Figure 16).

Figure 12 c shows the HER photocatalytic activities under UV light ( $372 \pm 5$  nm) when adding visible light or heat (see the Experimental Section for details). Experiments involved four consecutive steps: (1) upon turning on UV light, the HER began to increase until it stabilized. At this point, the sample temperature was ca. 24°C. (2) With UV light on, visible light was turned on, which increased the HER of most of the samples. The addition of visible light also increased the sample temperature, up to ca. 34–36°C. (3) Maintaining UV light on, visible light was turned off, which resulted in a relatively slow decrease of the HER and a temperature decrease down to 24°C. The slow HER decrease already denoted a significant effect of temperature on the observed increase of HER with visible light. (4) Still, with UV light on, the reactor was heated to 34–36°C, which also resulted in an increase of the HER for most catalysts. Comparing the HER obtained in stages 2 and 4 (Figure 12c,d), it was observed that the addition of visible light or heat resulted in a very significant increase of the HER for most samples. In the case of the reference TiO<sub>2</sub> catalyst and Co-doped TiO<sub>2</sub>, the very significant activity enhancement obtained with visible light was fully associated with the slight increase of temperature. Notice that almost a 2-fold increase of the HER was obtained with a temperature change of just 10°C, which opens the door for an efficient solar energy conversion through the thermophotocatalytic process. This strong influence of temperature in the photoproduction of hydrogen from the dehydrogenation of ethanol is related to the high adsorption energies of acetaldehyde on inorganic oxides, blocking the catalyst active sites. Moderate increases of temperature result into significantly weaker adsorption of acetaldehyde, resulting in the unblocking of the catalyst active sites.<sup>31,32</sup> CoTiO<sub>3</sub>/TiO<sub>2</sub> catalysts also showed an important increase of activity with the minor increase of temperature tested.

However, CoTiO<sub>3</sub>/TiO<sub>2</sub> samples displayed a much more significant increase of the HER when incorporating the visible light irradiation than when just heating the sample to the reached temperature. Among the different CoTiO<sub>3</sub>/TiO<sub>2</sub> composites, CoTiO<sub>3</sub>/TiO<sub>2</sub> (1%) displayed the highest performance when combining UV and visible light. Finally, the incorporation of visible light or temperature had a minor influence on the HER of CoTiO<sub>3</sub>.



**Figure 14.** Photocatalytic hydrogen production rates measured with TiO<sub>2</sub>, CoTiO<sub>3</sub>, TiO<sub>2</sub>:Co and CoTiO<sub>3</sub>/TiO<sub>2</sub> (1%, 2%, 5%) samples.



**Figure 15.** Comparison of the photocatalytic H<sub>2</sub> evolution on CoTiO<sub>3</sub>/TiO<sub>2</sub> (1%) under UV light irradiation ( $365 \pm 5$  nm,  $79.1 \pm 0.5$  mW·cm<sup>-2</sup>) in ethanol:water (1:9) and only water.

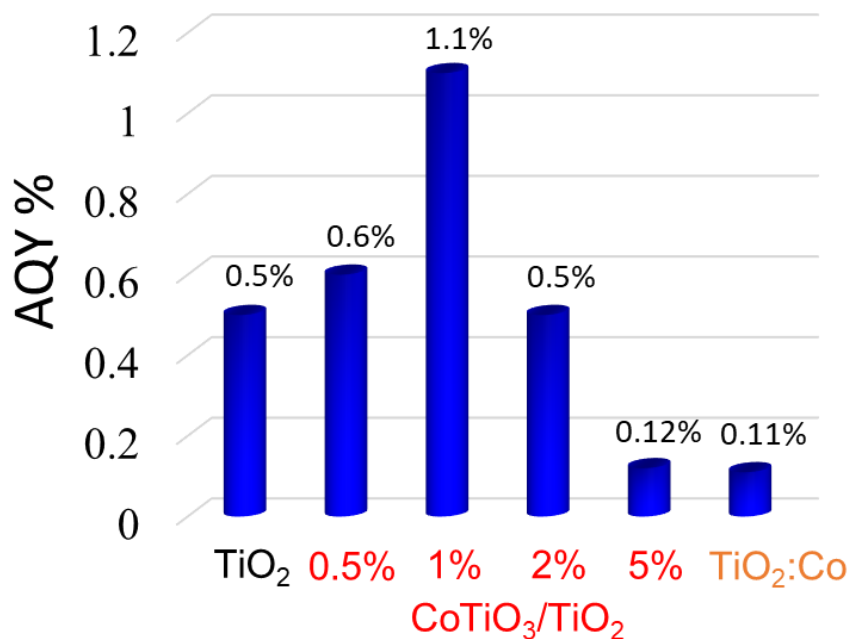


**Figure 16.** Apparent quantum yield (AQY) obtained under UV light from the different samples.

**Table S2.** Comparison of the hydrogen evolution rate and with reported Co-Ti-O systems.

Photocatalyst	H <sub>2</sub> Evolution Rate μmol h <sup>-1</sup> g <sup>-1</sup>	Reaction conditions	Ref.
TiO <sub>2</sub> /CoP (1%)	604	λ<400 nm 0.12 mW cm <sup>-2</sup>	S1
0.5 wt% CoP/TiO <sub>2</sub>	8,350	380-800 nm 1.5 mW cm <sup>-2</sup>	S2
CoO <sub>x</sub> (0.019 wt%) /TiO <sub>2</sub> /Pt (0.046 wt%)	7,882	λ<400 nm 35 mW cm <sup>-2</sup>	S3
CoO <sub>x</sub> /TiO <sub>2</sub> Co:Ti 2.9%	1,240	λ<400 nm 33 mW cm <sup>-2</sup>	S4
0.2% Cu-0.01% Co <sub>3</sub> O <sub>4</sub> /TiO <sub>2</sub>	286	380 nm 15.5 mW cm <sup>-2</sup>	S5
2 wt% Co <sub>3</sub> O <sub>4</sub> /TiO <sub>2</sub>	7,000	λ<400 nm 43 mW cm <sup>-2</sup>	S6
Co(0.5%):N-TiO <sub>2</sub>	197	λ>400 nm 380 mW cm <sup>-2</sup>	S7
CoTiO <sub>3</sub> /TiO <sub>2</sub> (1%)	3,800	365 nm 79.1 mW cm <sup>-2</sup>	This work

As shown in Figure 17a, just a slight deactivation of the  $\text{CoTiO}_3/\text{TiO}_2$  (1%) catalyst was observed when testing the activity for three consecutive cycles. A comparison of the XRD patterns and TEM images of the  $\text{CoTiO}_3/\text{TiO}_2$  (5%) sample before and after the photocatalytic tests (Figures 17b,c,d) revealed no apparent changes, suggesting that the  $\text{CoTiO}_3/\text{TiO}_2$  heterojunction possessed a good structural photostability.

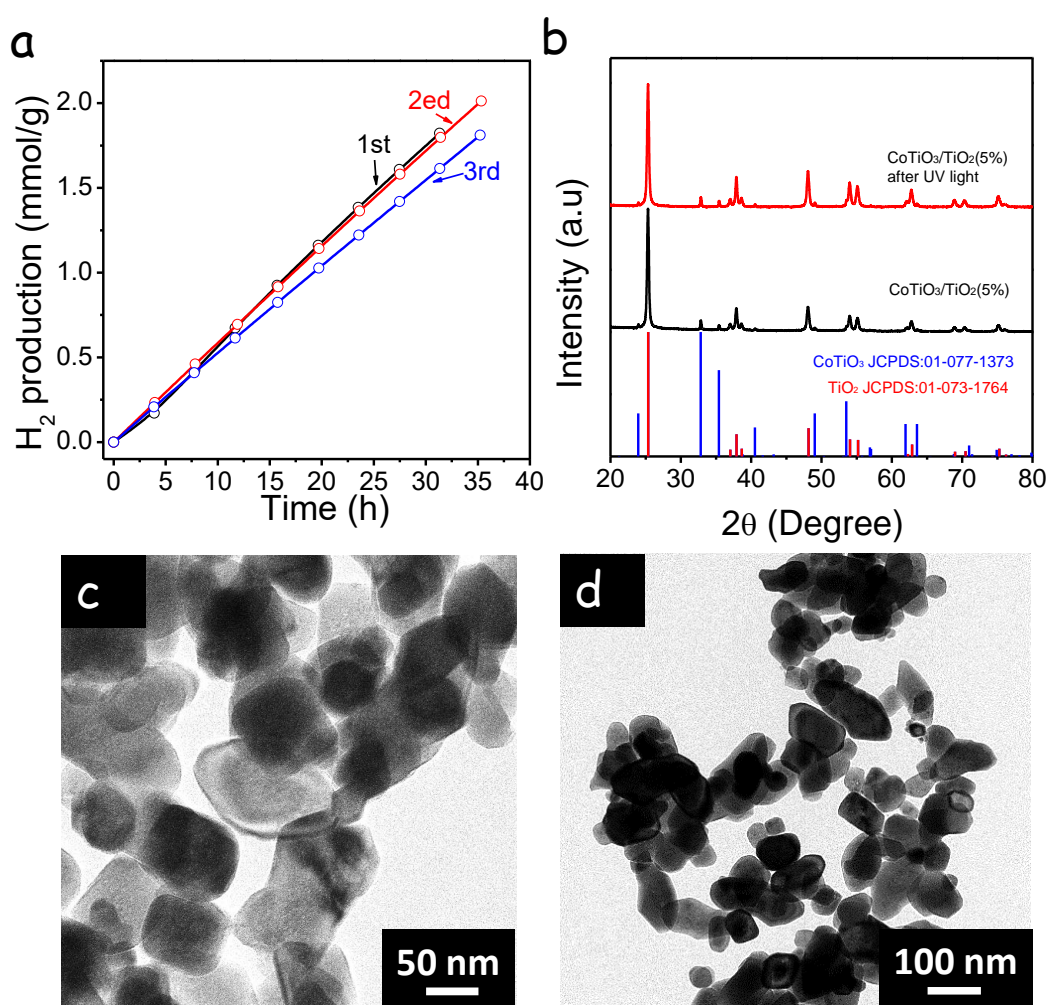


**Figure 17.** (a) Three consecutive cycles of photocatalytic hydrogen production under UV light using the same  $\text{CoTiO}_3/\text{TiO}_2$  (1%) sample. (b) XRD pattern of  $\text{CoTiO}_3/\text{TiO}_2$  (5%) before and after photocatalytic hydrogen production under UV light. TEM micrographs of  $\text{CoTiO}_3/\text{TiO}_2$  (5%) sample before (c) and after (d) photocatalytic hydrogen production under UV light.

The photocatalytic performance of semiconductor materials is closely related to the charge separation, transport, and transfer processes that strongly depend on their

relative electronic energy level positions. To gain insights from the photocatalytic process and to understand the enhanced performance of  $\text{CoTiO}_3/\text{TiO}_2$  composites at optimal loading, a set of spectroscopic analysis was carried out. The steady-state PL spectra recorded on  $\text{TiO}_2$  and  $\text{CoTiO}_3/\text{TiO}_2$  (1%) showed a characteristic peak around 400 nm (Figure 18a), which was in line with recent reports on PL spectra of  $\text{TiO}_2$ .<sup>33,34</sup> The lower PL intensity of the  $\text{CoTiO}_3/\text{TiO}_2$  composite originated from the reduced radiative charge recombination in  $\text{TiO}_2$  due to  $\text{CoTiO}_3$  incorporation. Similar PL attenuation effects were reported by Chen et al. on noble metal-decorated  $\text{TiO}_2$  nanocrystals<sup>34</sup> and by Zuo et al. on  $\text{SnS}_2\text{-Pt}$  nanoheterostructures.<sup>35</sup> To analyze the role of  $\text{CoTiO}_3$ , TRPL spectra of  $\text{TiO}_2$  and  $\text{CoTiO}_3/\text{TiO}_2$  heterostructures were measured and compared. The TRPL spectra tracked at 400 nm are shown in Figure 18b. The PL intensity of  $\text{CoTiO}_3/\text{TiO}_2$  (1%) was observed to decay significantly slower than for pristine  $\text{TiO}_2$ . The fitting revealed an average lifetime of 35.8 ns for  $\text{CoTiO}_3/\text{TiO}_2$  (1%) and 5.9 ns for  $\text{TiO}_2$ . The longer lifetime recorded over  $\text{CoTiO}_3/\text{TiO}_2$  proved that the heterojunction contributed to the charge separation, increasing, in this way, their recombination time.

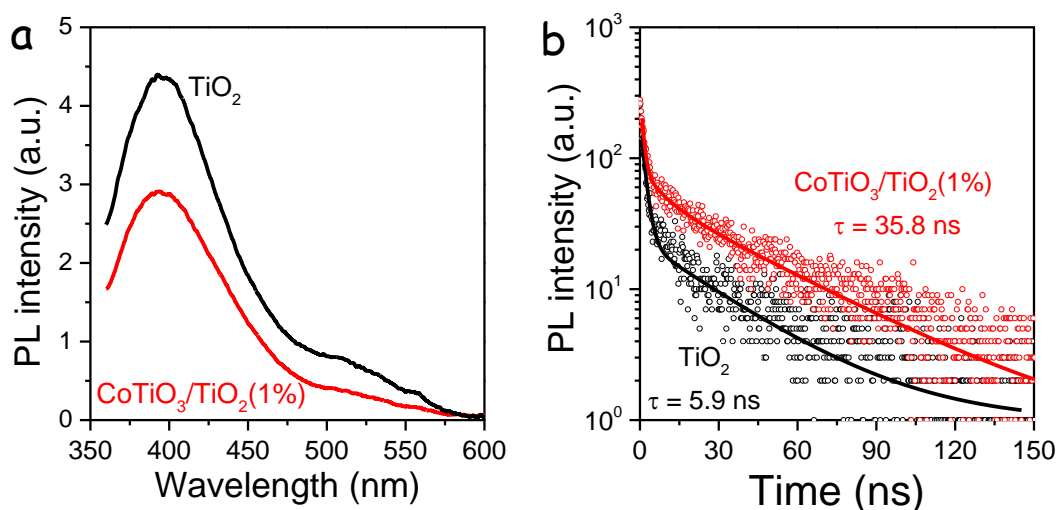


**Figure 18.** (a) Steady-state photoluminescence spectra. (b) Time-resolved photoluminescence spectra with corresponding fitting curves.

TPC and EIS measurements were conducted using photocatalyst films deposited on FTO substrates (see the Experimental Section for details). As shown in Figure 19a, the

loading of CoTiO<sub>3</sub> on TiO<sub>2</sub> at an optimal composition (1%) resulted in significantly enhanced photocurrent responses, with a higher steady-state photocurrent at 0.6 V versus a reversible hydrogen electrode (RHE) in contrast with pristine TiO<sub>2</sub> that may be related to an improved charge transfer process. As expected, the trend of a steady-state photocurrent matches with photocatalytic performance in Figure 12, indicating that the photocurrent in TPC measurements is linked to the hydrogen evolution reaction. Notably, TPC spikes, whose amplitude represents the degree of surface recombination,<sup>36</sup> were larger in pristine TiO<sub>2</sub> than in CoTiO<sub>3</sub>/TiO<sub>2</sub> (1%). This result indicated that the CoTiO<sub>3</sub>/TiO<sub>2</sub> heterojunction at optimal loading efficiently suppresses the surface charge recombination process. In the case of CoTiO<sub>3</sub>/TiO<sub>2</sub> (5%), which produces the least H<sub>2</sub> among other CoTiO<sub>3</sub>/TiO<sub>2</sub> heterojunctions, the TPC shows the lowest photocurrent and the largest transient spikes, indicating that a heterojunction with an excessive amount of CoTiO<sub>3</sub> can hamper the performance. Similar TPC responses have been reported on other photocatalyst systems, for example, carbon nanotube loaded TiO<sub>2</sub>,<sup>37</sup> a TiO<sub>2</sub>/Fe<sub>2</sub>TiO<sub>5</sub>/Fe<sub>2</sub>O<sub>3</sub> triple heterojunction,<sup>38</sup> and Bi<sub>2</sub>O<sub>3</sub>@TiO<sub>2</sub> photocatalyst.<sup>39</sup>

EIS measurements showed that qualitatively speaking, and as deduced from the Nyquist plots (Figure 19b), CoTiO<sub>3</sub>/TiO<sub>2</sub> (1%) was less resistive than TiO<sub>2</sub>,<sup>40</sup> indicating that the formation of the heterojunction at optimal loading facilitated the charge transport process. The semicircle diameter for 0.5% and 2% loading is close to that of pristine TiO<sub>2</sub>, indicating a similar resistivity. As shown in the inset of Figure 5b, a Randles equivalent circuit was employed to fit the data, which consisted of a series resistor  $R_S$ , a bulk resistor  $R_{ct,bulk}$  for charge transport resistance, and a bulk capacitor  $C_{bulk}$  for space charge region capacitance.<sup>41</sup> The data fitting showed that CoTiO<sub>3</sub>/TiO<sub>2</sub> (1%) had two times lower  $R_{ct,bulk}$  than TiO<sub>2</sub>. With only 1% incorporation of CoTiO<sub>3</sub> on TiO<sub>2</sub> the value of  $R_{ct,bulk}$  was reduced a twofold, from 5.77 kΩ to 2.68 kΩ. Fitting results for different loadings are listed in Table 3, where trend of  $R_{ct,bulk}$  follows well with H<sub>2</sub> production performance, indicating charge transport in heterojunctions is essential for photocatalytic reactions. Likewise, the electron lifetime,  $\tau_n$ , could be estimated by the RC time constant of the Randles circuit.<sup>32</sup>

Generally speaking,  $\tau_n$  characterizes the electron recombination; a shorter  $\tau_n$  means a faster recombination process. The formation of the CoTiO<sub>3</sub>/TiO<sub>2</sub> heterojunction at optimal loading (1%) boosted  $\tau_n$  from 1.3 ms to 2.9 ms, which implies that the heterojunction reduced charge recombination probably due to a promoted charge separation, consistent with TRPL results.

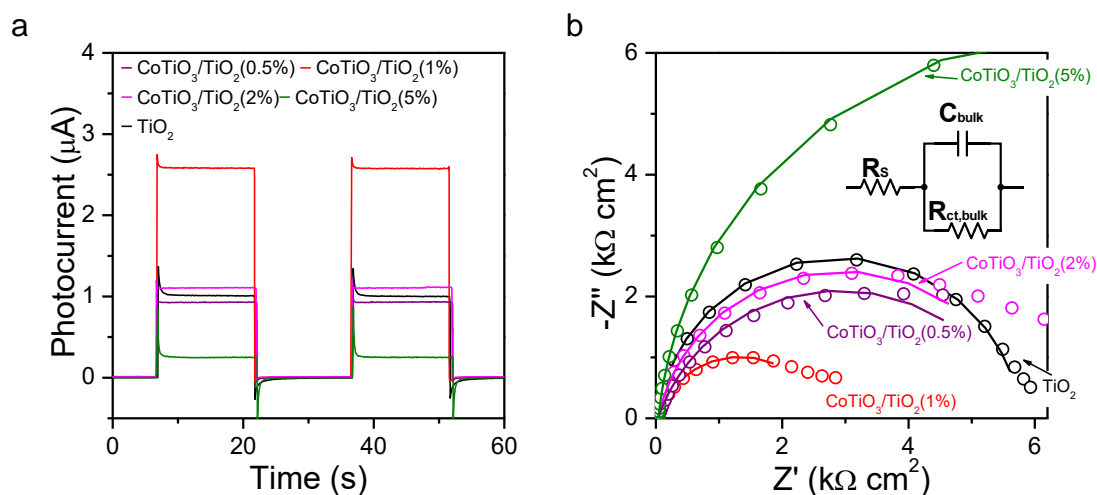


**Figure 19.** (a) Transient photocurrent response. (b) Nyquist plot of impedance response with corresponding equivalent circuit for fitting.

**Table 3.** EIS data fitting results.

Photocatalyst	$R_{ct,bulk}$ (kΩ)	$C_{bulk}$ (μF)	$R_s$ (Ω)
TiO <sub>2</sub>	5.77	3.18	41.89
CoTiO <sub>3</sub> /TiO <sub>2</sub> (0.5%)	5.74	18.86	36.51
CoTiO <sub>3</sub> /TiO <sub>2</sub> (1%)	2.68	13.67	37.37
CoTiO <sub>3</sub> /TiO <sub>2</sub> (2%)	5.80	6.85	39.53
CoTiO <sub>3</sub> /TiO <sub>2</sub> (5%)	13.89	3.36	41.38

## Photocatalytic Mechanism

Using UPS, the valence band maximum (VBM) values of the  $\text{TiO}_2$  and  $\text{CoTiO}_3$  reference materials were determined to be at  $-6.57$  eV and  $-7.13$  eV versus vacuum, respectively (Figure 20a).<sup>15,42,43</sup> Taking into account the measured band gaps and VBM position, the band alignment between  $\text{TiO}_2$  and  $\text{CoTiO}_3$  corresponded to that of a type II heterostructure (left scheme in Figure 21). Thus, considering a type II heterojunction charge-transfer mechanism, within the  $\text{CoTiO}_3/\text{TiO}_2$  heterojunction, photogenerated electrons would travel from  $\text{TiO}_2$  to  $\text{CoTiO}_3$  and holes from  $\text{CoTiO}_3$  to  $\text{TiO}_2$ . However, because the conduction band maximum (CBM) of  $\text{CoTiO}_3$  is at a lower position than the  $\text{H}_2/\text{H}^+$  level, the free electrons of  $\text{CoTiO}_3$  see an energy barrier to reduce  $\text{H}^+$  into  $\text{H}_2$  (left scheme in Figure 21).<sup>43</sup> This does not match well with the enhanced photocatalytic performance observed in  $\text{CoTiO}_3/\text{TiO}_2$  composites with respect to  $\text{TiO}_2$ .

Actually, taking into account the electron energy band position of the two materials and intrinsic n-type character of  $\text{TiO}_2$  and p-type character of  $\text{CoTiO}_3$ , upon placing the two materials in contact, an injection of electrons from  $\text{TiO}_2$  to  $\text{CoTiO}_3$  will occur. This charge redistribution will create an electric field at the interphase. In view of the small size of the crystallites and the moderate charge carrier concentration characterizing these types of materials, this electric field will probably extend through the whole  $\text{TiO}_2$  and  $\text{CoTiO}_3$  domains. The electric field will thus drive electrons photogenerated within  $\text{TiO}_2$  and holes photogenerated within  $\text{CoTiO}_3$  away from the interphase and holes photogenerated within the  $\text{TiO}_2$  and electrons photogenerated within  $\text{CoTiO}_3$  toward the interphase, where they probably recombine (right scheme in Figure 21). As a result, photogenerated electrons in the CB of  $\text{TiO}_2$ , thus having a high reduction potential, are driven toward the surface with a reduced probability of recombination with VB holes. Thus,  $\text{TiO}_2$  photogenerated electrons could reduce protons into hydrogen more effectively. Likewise, photogenerated holes in the VB of  $\text{CoTiO}_3$ , i.e., with a strong oxidation potential, are driven to the surface with a lower chance to recombine with CB electrons. Thus,  $\text{CoTiO}_3$  photogenerated holes can more efficiently drive ethanol dehydrogenation to acetaldehyde and protons. Overall, a clear synergism between the two materials is established through this direct Z-scheme charge transfer

mechanism.<sup>44-48</sup>

Finally, Figure 20b,c,d show the O 1s, Ti 2p, and Co 2p XPS spectra of the reference samples and CoTiO<sub>3</sub>/TiO<sub>2</sub> composites. The most interesting aspect of these analyses was the additional peak (532.5 eV) appearing at a lower binding energy than the main O 1s peak (529.6 eV) corresponding to lattice oxygen. This new peak should be associated with OH<sup>-</sup> groups.<sup>49</sup> The notable increase of surface-adsorbed species and particularly hydroxyl groups in the CoTiO<sub>3</sub>/TiO<sub>2</sub> composites is indicative of the promoted charge separation and tendency of part of the charge carriers to migrate toward the surface away from an interphase, where they can promote molecular adsorption and redox reactions.

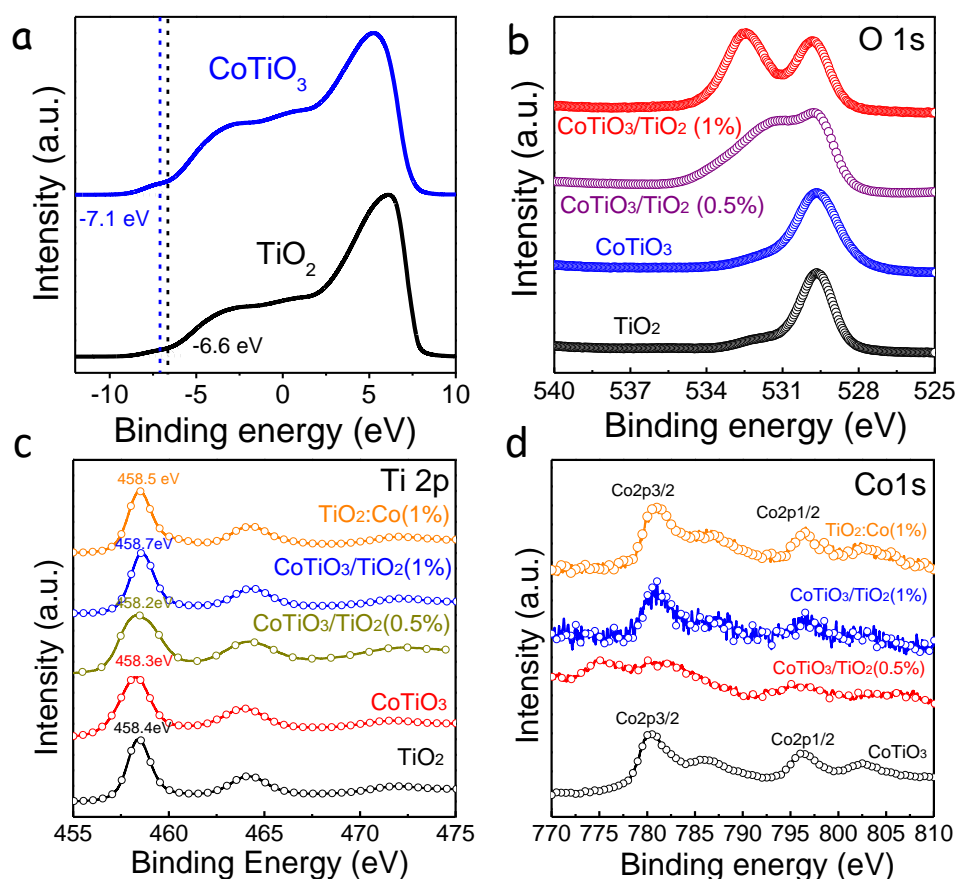


**Figure 20.** (a) UPS spectrum for TiO<sub>2</sub> and CoTiO<sub>3</sub>. (b) O 1s XPS spectra of TiO<sub>2</sub>, CoTiO<sub>3</sub>, CoTiO<sub>3</sub>/TiO<sub>2</sub> (0.5%) and CoTiO<sub>3</sub>/TiO<sub>2</sub> (1%). High resolution XPS spectra of (c) Ti 2p and (d) Co 2p regions from TiO<sub>2</sub>, CoTiO<sub>3</sub>, and CoTiO<sub>3</sub>/TiO<sub>2</sub> (0.5%, 1, 2, 5%).

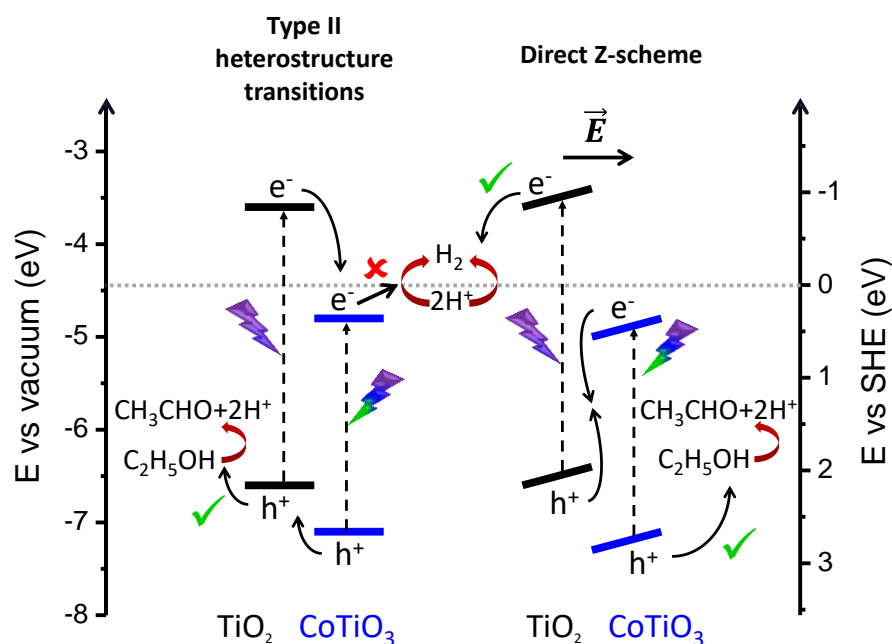


**Figure 21.** Schematic illustration of the relative energy levels of  $\text{TiO}_2$  and  $\text{CoTiO}_3$  and simplified charge transfer mechanism between  $\text{TiO}_2$  and  $\text{CoTiO}_3$  in a conventional type II heterostructure and a direct Z-scheme.

### 3.5 Conclusions

A simple method for the synthesis of  $\text{CoTiO}_3/\text{TiO}_2$  heterostructures with tuned  $\text{CoTiO}_3$  amounts was presented. The materials showed an excellent activity in the photocatalytic hydrogen evolution from ethanol dehydrogenation, with the HER under UV light well above those of  $\text{TiO}_2$ ,  $\text{CoTiO}_3$ , and Co-doped  $\text{TiO}_2$ . We also observed a significant influence of visible light on the HER of  $\text{CoTiO}_3/\text{TiO}_2$  heterostructures beyond the important effect of the increased temperature. Electrochemical impedance spectroscopy and static and time-resolved PL measurements showed the formed heterostructures to promote charge separation, extending the lifetime of photogenerated charge carriers. UV-vis spectroscopy and UPS analysis showed the alignment of the energy levels of the two materials to resemble a type II heterostructure, with the CBM of  $\text{CoTiO}_3$  below the  $\text{H}_2/\text{H}^+$  energy level. In such type II heterostructures, electron transfer from n-type  $\text{TiO}_2$  to p-type  $\text{CoTiO}_3$  is to be expected, generating an electric field within the material that drives photogenerated electrons within  $\text{TiO}_2$  and photogenerated holes within  $\text{CoTiO}_3$  away from the interphase and photogenerated holes in  $\text{TiO}_2$  and electrons in  $\text{CoTiO}_3$  toward the

interphase where they recombine. All these evidences pointed out toward a direct Z-scheme mechanism as responsible of the enhanced photocatalytic ethanol dehydrogenation activity of CoTiO<sub>3</sub>/TiO<sub>2</sub> composites over that of TiO<sub>2</sub>.

### 3.6 References

1. Zhang, X.; Luo, L.; Yun, R.; Pu, M.; Zhang, B.; Xiang, X., Increasing the Activity and Selectivity of TiO<sub>2</sub>-Supported Au Catalysts for Renewable Hydrogen Generation from Ethanol Photoreforming by Engineering Ti<sup>3+</sup> Defects. *ACS Sustain. Chem. Eng.* **2019**, *7*, 13856–13864.
2. Bušić, A.; Marđetko, N.; Kundas, S.; Morzak, G.; Belskaya, H.; Ivančić Šantek, M.; Komes, D.; Novak, S.; Šantek, B., Bioethanol Production from Renewable Raw Materials and Its Separation and Purification: A Review. *Biotechnol.* **2018**, *56*, 289–311.
3. Lu, X.; Xie, S.; Yang, H.; Tong, Y.; Ji, H., Photoelectrochemical Hydrogen Production from Biomass Derivatives and Water. *Chem. Soc. Rev.* **2014**, *43*, 7581–7593.
4. Eagan, N. M.; Kumbhalkar, M. D.; Buchanan, J. S.; Dumesic, J. A.; Huber, G. W., Chemistries and Processes for the Conversion of Ethanol into Middle-Distillate Fuels. *Nat. Rev. Chem.* **2019**, *3*, 223–249.
5. Zhang, Q.; Liu, W.; Chen, B.; Qiu, S.; Wang, T., Upgrading of Aqueous Ethanol to Fuel Grade Higher Alcohols over Dandelion-like Ni-Sn Catalyst. *Energy Convers. Manage.* **2020**, *216*, 112914.
6. Murdoch, M.; Waterhouse, G.; Nadeem, M.; Metson, J.; Keane, M.; Howe, R.; Llorca, J.; Idriss, H., The Effect of Gold Loading and Particle Size on Photocatalytic Hydrogen Production from Ethanol over Au/TiO<sub>2</sub> Nanoparticles. *Nat. Chem.* **2011**, *3*, 489–492.
7. Yang, Y.; Chang, C. H.; Idriss, H., Photo-Catalytic Production of Hydrogen from Ethanol over M/TiO<sub>2</sub> Catalysts (M= Pd, Pt or Rh). *Appl. Catal. B Environ.* **2006**, *67*, 217–222.
8. Kalnenieks, U.; Balodite, E.; Ströhler, S.; Strazdina, I.; Rex, J.; Pentjuss, A.; Fuchino, K.; Bruheim, P.; Rutkis, R.; Pappas, K. M.; Poole, R. K.; Sawodny, O.; Bettenbrock, K., Improvement of Acetaldehyde Production in *Zymomonas Mobilis* by Engineering of Its Aerobic Metabolism. *Front. Microbiol.* **2019**, *10*, 2533.
9. Danner, H.; Braun, R., Biotechnology for the Production of Commodity Chemicals from Biomass. *Chem. Soc. Rev.* **1999**, *28*, 395–405.
10. Moore, C. M.; Staples, O.; Jenkins, R. W.; Brooks, T. J.; Semelsberger, T. A.; Sutton, A. D., Acetaldehyde as an Ethanol Derived Bio-Building Block: An Alternative to Guerbet Chemistry. *Green Chem.* **2017**, *19*, 169–174.
11. Staples, O.; Moore, C. M.; Leal, J. H.; Semelsberger, T. A.; McEnally, C. S.; Pfefferle, L. D.; Sutton, A. D., A simple, Solvent Free Method for Transforming Bio-Derived Aldehydes into Cyclic Acetals for Renewable Diesel Fuels. *Sustain. Energy Fuels* **2018**, *2*, 2742–2746.
12. Quesada, J.; Arreola-Sánchez, R.; Faba, L.; Díaz, E.; Rentería-Tapia, V. M.; Ordóñez, S., Effect of Au Nanoparticles on the Activity of TiO<sub>2</sub> for Ethanol Upgrading Reactions. *Appl. Catal. A General* **2018**, *551*, 23–33.

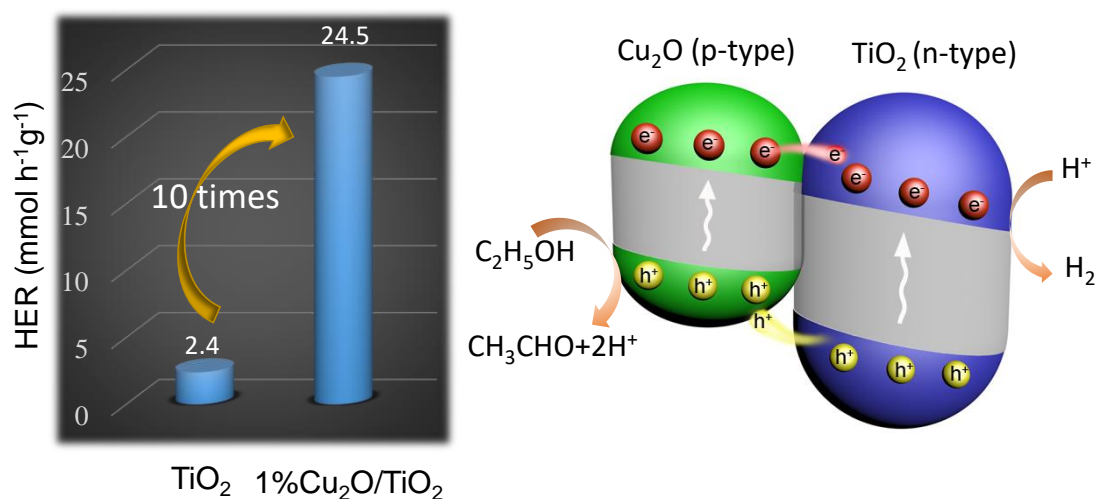
13. Shi, H.; Zhang, S.; Zhu, X.; Liu, Y.; Wang, T.; Jiang, T.; Zhang, G.; Duan, H., Uniform Gold-Nanoparticle-Decorated {001}-Faceted Anatase TiO<sub>2</sub> Nanosheets for Enhanced Solar-Light Photocatalytic Reactions. *ACS Appl. Mater. Interfaces* **2017**, *9*, 36907–36916.
14. Linsebigler, A. L.; Lu, G.; Yates Jr, J. T., Photocatalysis on TiO<sub>2</sub> Surfaces: Principles, Mechanisms, and Selected Results. *Chem. Rev.* **1995**, *95*, 735–758.
15. Ge, M.; Cao, C.; Huang, J.; Li, S.; Chen, Z.; Zhang, K.-Q.; Al-Deyab, S.; Lai, Y., A Review of One-Dimensional TiO<sub>2</sub> Nanostructured Materials for Environmental and Energy Applications. *J. Mater. Chem. A* **2016**, *4*, 6772–6801.
16. Muñoz-Batista, M. J.; Gómez-Cerezo, M. N.; Kubacka, A.; Tudela, D.; Fernández-García, M., Role of Interface Contact in CeO<sub>2</sub>-TiO<sub>2</sub> Photocatalytic Composite Materials. *ACS Catal.* **2014**, *4*, 63–72.
17. Ye, R.; Fang, H.; Zheng, Y.-Z.; Li, N.; Wang, Y.; Tao, X., Fabrication of CoTiO<sub>3</sub>/g-C<sub>3</sub>N<sub>4</sub> Hybrid Photocatalysts with Enhanced H<sub>2</sub> Evolution: Z-Scheme Photocatalytic Mechanism Insight. *ACS Appl. Mater. Interfaces* **2016**, *8*, 13879–13889.
18. Hashemian, S.; Foroghmoqhadam, A., Effect of Copper Doping on CoTiO<sub>3</sub> Ilmenite Type Nanoparticles for Removal of Congo Red from Aqueous Solution. *Chem. Eng. J.* **2014**, *235*, 299–306.
19. Zou, J.; Zheng, W., TiO<sub>2</sub>@CoTiO<sub>3</sub> Complex Green Pigments with Low Cobalt Content and Tunable Color Properties. *Ceram. Int.* **2016**, *42*, 8198–8205.
20. Li, Y.; Yang, W.; Wang, C.; Li, Z.; Lai, J.; Wang, L.; Huang, L., Achieving Controllable CoTiO<sub>3</sub>-Encapsulated TiO<sub>2</sub> Heterostructures for Enhanced Photoelectrochemical Water Splitting. *ACS Appl. Energy Mater.* **2019**, *2*, 8229–8235.
21. Sirsat, S. A.; Hecht, O.; Mirabal, C.; Pepe, D. A.; Yang, W.; Mohammad, Z.; Hadjiev, V. G.; Neal, J. A.; Hernandez, F. C. R., Bacteriostatic Effect of CoO-TiO<sub>2</sub> on *Listeria Monocytogenes* by the Presence of the Co-Catalytic CoO Nanoparticles. *J. Environ. Chem. Eng.* **2020**, *8*, 104259.
22. Sarkar, B.; Pendem, C.; Konathala, L. S.; Sasaki, T.; Bal, R., Formation of Ilmenite-Type CoTiO<sub>3</sub> on TiO<sub>2</sub> and Its Performance in Oxidative Dehydrogenation of Cyclohexane with Molecular Oxygen. *Catal. Commun.* **2014**, *56*, 5–10.
23. Nagaoka, K.; Takanabe, K.; Aika, K.-i., Modification of Co/TiO<sub>2</sub> for Dry Reforming of Methane at 2 MPa by Pt, Ru or Ni. *Appl. Catal. A General* **2004**, *268*, 151–158.
24. Li, H.; Gao, Q.; Wang, G.; Han, B.; Xia, K.; Zhou, C., Architecturing CoTiO<sub>3</sub> Overlayer on Nanosheets-Assembled Hierarchical TiO<sub>2</sub> Nanospheres as a Highly Active and Robust Catalyst for Peroxymonosulfate Activation and Metronidazole Degradation. *Chem. Eng. J.* **2020**, *392*, 123819.
25. Lu, J.; Liang, K.; Xu, C.; Wang, X.; Ouyang, H.; Huang, J.; Feng, L., Humidity Sensor Based on Heterogeneous CoTiO<sub>3</sub>/TiO<sub>2</sub> Film with Vertically Aligned Nanocrystalline Structure. *Vacuum* **2019**, *163*, 292–300.
26. Ehsan, M. A.; Naeem, R.; Khaledi, H.; Sohail, M.; Saeed, A. H.; Mazhar, M., Fabrication of CoTiO<sub>3</sub>-TiO<sub>2</sub> Composite Films from a Heterobimetallic Single Source Precursor for Electrochemical Sensing of Dopamine. *Dalton Trans.* **2016**, *45*, 10222–10232.
27. Liu, H.; Wu, X.; Guo, E.; Lu, Q., Tailored Synthesis of Coral-Like CoTiO<sub>3</sub>/Co<sub>3</sub>O<sub>4</sub>/TiO<sub>2</sub> Nanobelts with Superior Lithium Storage Capability. *Energy Technol.* **2020**, *8*, 1900774.

28. Xu, D.-X.; Lian, Z.-W.; Fu, M.-L.; Yuan, B.; Shi, J.-W.; Cui, H.-J., Advanced Near-Infrared-Driven Photocatalyst: Fabrication, Characterization, and Photocatalytic Performance of  $\beta$ -NaYF<sub>4</sub>: Yb<sup>3+</sup>, Tm<sup>3+</sup>@TiO<sub>2</sub> Core@shell Microcrystals. *Appl. Catal. B Environ.* **2013**, *142*, 377–386.
29. Sekhar, M. C.; Reddy, B. P.; Prakash, B. P.; Park, S.-H., Effects of Annealing Temperature on Phase Transformation of CoTiO<sub>3</sub> Nanoparticles and on Their Structural, Optical, and Magnetic Properties. *J. Supercond. Nov. Magn.* **2020**, *33*, 407–415.
30. Wei, N.; Cui, H.; Song, Q.; Zhang, L.; Song, X.; Wang, K.; Zhang, Y.; Li, J.; Wen, J.; Tian, J., Ag<sub>2</sub>O Nanoparticle/TiO<sub>2</sub> Nanobelt Heterostructures with Remarkable Photo-Response and Photocatalytic Properties under UV, Visible and near-Infrared Irradiation. *Appl. Catal. B Environ.* **2016**, *198*, 83–90.
31. Guil, J. M.; Homs, N.; Llorca, J.; Ramírez de la Piscina, P., Microcalorimetric and Infrared Studies of Ethanol and Acetaldehyde Adsorption to Investigate the Ethanol Steam Reforming on Supported Cobalt Catalysts. *J. Phys. Chem. B* **2005**, *109*, 10813–10819.
32. Castedo, A.; Casanovas, A.; Angurell, I.; Soler, L.; Llorca, J., Effect of Temperature on the Gas-Phase Photocatalytic H<sub>2</sub> Generation Using Microreactors under UVA and Sunlight Irradiation. *Fuel* **2018**, *222*, 327–333.
33. Yu, Y.; Wen, W.; Qian, X.-Y.; Liu, J.-B.; Wu, J.-M., UV and Visible Light Photocatalytic Activity of Au/TiO<sub>2</sub> Nanoforests with Anatase/Rutile Phase Junctions and Controlled Au Locations. *Scientific reports* **2017**, *7*, 1–13.
34. Chen, Y.; Wang, Y.; Li, W.; Yang, Q.; Hou, Q.; Wei, L.; Liu, L.; Huang, F.; Ju, M., Enhancement of Photocatalytic Performance with the Use of Noble-Metal-Decorated TiO<sub>2</sub> Nanocrystals as Highly Active Catalysts for Aerobic Oxidation under Visible-Light Irradiation. *Appl. Catal. B Environ.* **2017**, *210*, 352–367.
35. Zuo, Y.; Liu, Y.; Li, J.; Du, R.; Yu, X.; Xing, C.; Zhang, T.; Yao, L.; Arbiol, J.; Llorca, J.; Sivula, K.; Guijarro, N.; Cabot, A., Solution-Processed Ultrathin SnS<sub>2</sub>-Pt Nanoplates for Photoelectrochemical Water Oxidation. *ACS Appl. Mater. Interfaces* **2019**, *11*, 6918–6926.
36. Liu, Y.; Le Formal, F.; Boudoire, F.; Yao, L.; Sivula, K.; Guijarro, N., Insights into the Interfacial Carrier Behaviour of Copper Ferrite (CuFe<sub>2</sub>O<sub>4</sub>) Photoanodes for Solar Water Oxidation. *J. Mater. Chem. A* **2019**, *7*, 1669–1677.
37. Zhang, Y.; Gong, M.; Liu, X.; Ji, L.; Yang, Z.; Zhu, X., Preparation of Activated Carbon Nanotube Foams Loaded with Ag-Doped TiO<sub>2</sub> for Highly Efficient Photocatalytic Degradation under UV and Visible Light. *J. Mat. Sci.* **2019**, *54*, 2975–2989.
38. Deng, Y.; Xing, M.; Zhang, J., An Advanced TiO<sub>2</sub>/Fe<sub>2</sub>TiO<sub>5</sub>/Fe<sub>2</sub>O<sub>3</sub> Triple-Heterojunction with Enhanced and Stable Visible-Light-Driven Fenton Reaction for the Removal of Organic Pollutants. *Appl. Catal. B Environ.* **2017**, *211*, 157–166.
39. Reddy, N. L.; Emin, S.; Valant, M.; Shankar, M., Nanostructured Bi<sub>2</sub>O<sub>3</sub>@TiO<sub>2</sub> Photocatalyst for Enhanced Hydrogen Production. *Int. J. Hydrogen Energy* **2017**, *42*, 6627–6636.
40. Liu, Y.; Le Formal, F.; Boudoire, F.; Guijarro, N., Hematite Photoanodes for Solar Water Splitting: A Detailed Spectroelectrochemical Analysis on the pH-Dependent Performance. *ACS Appl. Energy Mater.* **2019**, *2*, 6825–6833.
41. Zuo, Y.; Liu, Y.; Li, J.; Du, R.; Han, X.; Zhang, T.; Arbiol, J.; Divins, N. r. J.; Llorca, J.;

- Guijarro, N. s., Guijarro, N.; Cabot, A., In situ Electrochemical Oxidation of Cu<sub>2</sub>S into CuO Nanowires as a Durable and Efficient Electrocatalyst for Oxygen Evolution Reaction. *Chem. Mater.* **2019**, *31*, 7732–7743.
42. Jiménez-Calvo, P.; Caps, V.; Ghazzal, M. N.; Colbeau-Justin, C.; Keller, V., Au/TiO<sub>2</sub> (P25)-gC<sub>3</sub>N<sub>4</sub> Composites with Low gC<sub>3</sub>N<sub>4</sub> Content Enhance TiO<sub>2</sub> Sensitization for Remarkable H<sub>2</sub> Production from Water under Visible-Light Irradiation. *Nano Energy* **2020**, *75*, 104888.
  43. Paramasivam, I.; Jha, H.; Liu, N., Schmuki, P., A Review of Photocatalysis Using Self-Organized TiO<sub>2</sub> Nanotubes and Other Ordered Oxide Nanostructures. *Small* **2012**, *8*, 3073–3103.
  44. Low, J.; Dai, B.; Tong, T.; Jiang, C.; Yu J., In Situ Irradiated X-Ray Photoelectron Spectroscopy Investigation on a Direct Z-Scheme TiO<sub>2</sub>/CdS Composite Film Photocatalyst. *Adv. Mater.* **2019**, *31*, 1802981.
  45. Jo, K.; Sivakumar, T., Facile Synthesis of Novel Redox-Mediator-Free Direct Z-Scheme CaIn<sub>2</sub>S<sub>4</sub> Marigold-Flower-like/TiO<sub>2</sub> Photocatalysts with Superior Photocatalytic Efficiency. *ACS Appl. Mater. Interfaces* **2015**, *7*, 17138–17154.
  46. Ma, K.; Yehezkeli, O.; Domaille, W.; Funke, H. H.; Cha, J. N., Enhanced Hydrogen Production from DNA-Assembled Z-Scheme TiO<sub>2</sub>-CdS Photocatalyst Systems. *Angew. Chem. Int. Ed.*, **2015**, *54*, 11490–11494.
  47. Yuan, L.; Weng, B.; Colmenares, J C., Sun Y.; Xu, Yi. J., Multichannel Charge Transfer and Mechanistic Insight in Metal Decorated 2D-2D Bi<sub>2</sub>WO<sub>6</sub>-TiO<sub>2</sub> Cascade with Enhanced Photocatalytic Performance. *Small* **2017**, *13*, 1702253.
  48. Zhou, P.; Yu, J.; Jaroniec, M., All-Solid-State Z-Scheme Photocatalytic Systems. *Adv. Mater.* **2014**, *26*, 4920–4935.
  49. Moulder, F., Handbook of X-Ray Photoelectron Spectroscopy. *Phys. electron.* **1995**, 230–232.
  50. Martínez, L.; Soler, L.; Angurell, I.; Llorca, J., Effect of TiO<sub>2</sub> Nanoshape on the Photoproduction of Hydrogen from Water-Ethanol Mixtures over Au<sub>3</sub>Cu/TiO<sub>2</sub> Prepared with Preformed Au-Cu Alloy Nanoparticles. *Appl. Catal. B Environ.* **2019**, *248*, 504–514.
  51. Xing, C.; Liu, Y.; Zhang, Y.; Liu, J.; Zhang, T.; Tang, P.; Arbiol, J.; Soler, L.; Sivula, K.; Guijarro, N., Wang, X.; Li, J.; Du, R.; Zuo, Y., Cabot, A.; Llorca, J., Porous NiTiO<sub>3</sub>/TiO<sub>2</sub> Nanostructures for Photocatalytic Hydrogen Evolution. *J. Mater. Chem. A* **2019**, *7*, 17053–17059.
  - S1. Liu, Q.; Huang, J.; Tang, H.; Yu, X.; Shen, J., Construction 0D TiO<sub>2</sub> Nanoparticles/2D CoP Nanosheets Heterojunctions for Enhanced Photocatalytic H<sub>2</sub> Evolution Activity. *J. Mater. Sci. Technol* **2020**, *56*, 196–205.
  - S2. Yue, X.; Yi, S.; Wang, R.; Zhang, Z.; Qiu, S., Cobalt Phosphide Modified Titanium Oxide Nanophotocatalysts with Significantly Enhanced Photocatalytic Hydrogen Evolution from Water Splitting. *Small* **2017**, *13*, 1603301.
  - S3. Zhang, J.; Yu, Z.; Gao, Z.; Ge, H.; Zhao, S.; Chen, C.; Chen, S.; Tong, X.; Wang, M.; Zheng, Z., Porous TiO<sub>2</sub> Nanotubes with Spatially Separated Platinum and CoO<sub>x</sub> Cocatalysts Produced by Atomic Layer Deposition for Photocatalytic Hydrogen Production. *Angew. Chem. Int. Ed.* **2017**, *56*, 816–820.
  - S4. Wang, Y.-F.; Hsieh, M.-C.; Lee, J.-F.; Yang, C.-M., Nonaqueous Synthesis of CoO<sub>x</sub>/TiO<sub>2</sub> Nanocomposites Showing High Photocatalytic Activity of Hydrogen

- Generation. *Appl. Catal., B* **2013**, *142*, 626–632.
- S5. Shen, H.; Ni, D.; Niu, P.; Zhou, Y.; Zhai, T.; Ma, Y., Enhancing Photocatalytic H<sub>2</sub> Evolution from Water on CuO-Co<sub>3</sub>O<sub>4</sub>/TiO<sub>2</sub>: The Key Roles of Co<sub>3</sub>O<sub>4</sub> Loading Amounts. *Int. J. Hydrogen Energy* **2017**, *42*, 30559–30568.
- S6. Bala, S.; Mondal, I.; Goswami, A.; Pal, U.; Mondal, R., Co-MOF as a Sacrificial Template: Manifesting a New Co<sub>3</sub>O<sub>4</sub>/TiO<sub>2</sub> System with a p–n Heterojunction for Photocatalytic Hydrogen Evolution. *J. Mater. Chem. A* **2015**, *3*, 20288–20296.
- S7. Wei, W.-D.; Liu, X.-Y.; Cui, S.-C.; Liu, J.-G., Loading of Co<sub>3</sub>O<sub>4</sub> onto Pt-Modified Nitrogen-Doped TiO<sub>2</sub> Nanocomposites Promotes Photocatalytic Hydrogen Production. *RSC. Adv* **2017**, *7*, 25650–25656.

## Chapter 4 Photodehydrogenation of ethanol over $\text{Cu}_2\text{O}/\text{TiO}_2$ heterostructures



### 4.1 Abstract

The photodehydrogenation of ethanol is a sustainable and potentially cost-effective strategy to produce hydrogen and acetaldehyde from renewable resources. The optimization of this process requires the use of highly active, stable and selective photocatalytic materials based on abundant elements, and the proper adjustment of the reaction conditions, including temperature. In this work,  $\text{Cu}_2\text{O}-\text{TiO}_2$  type-II heterojunctions with different  $\text{Cu}_2\text{O}$  amounts are obtained by a one-pot hydrothermal method. The structural and chemical properties of the produced materials and their activity toward ethanol photodehydrogenation under UV and visible light illumination are evaluated. The  $\text{Cu}_2\text{O}-\text{TiO}_2$  photocatalysts exhibit a high selectivity toward acetaldehyde production and up to tenfold higher hydrogen evolution rates compared to bare  $\text{TiO}_2$ . We further discern here the influence of temperature and visible light absorption on photocatalytic performance. Our results point toward the combination of energy sources in thermo-photocatalytic reactors as an efficient strategy for solar energy conversion.

## 4.2 Introduction

Molecular hydrogen, a clean energy carrier and a key component in the chemical industry, is mostly produced through partial oxidation and steam reforming of natural gas, and coal gasification. To move away from the exploitation of fossil fuels, cost- and energy-effective strategies for the direct production of hydrogen from renewable sources need to be defined. In this context, biomass resources are a particularly compelling alternative source of hydrogen owing to their renewable character and their near net-zero CO<sub>2</sub> footprint.<sup>1-6</sup> Additional advantages of the hydrogen production from dehydrogenation of biomass-derived organics are the potential to co-produce valuable side organic chemicals for better process economics and the possibility to implement cost-effective waste abatement processes.<sup>7-8</sup>

Among the possible dehydrogenation processes, photocatalytic routes that make use of ubiquitous, abundant and renewable solar energy are especially attractive. Photocatalytic processes also enable the dehydrogenation reaction to take place in milder conditions, which further decreases costs and can increase the side product selectivity compared with thermocatalytic analogues.<sup>2</sup> From another point of view, the photocatalytic production of fuels can be considered as a convenient strategy to store intermittent solar energy.<sup>9,10</sup>

In this scenario, the photodehydrogenation of ethanol to produce molecular hydrogen and acetaldehyde using solar light as the only energy input is especially appealing.<sup>6,11</sup> As a liquid, ethanol can be easily stored and transported. Besides, ethanol can be easily produced from several biomass-derived feedstocks and organic residues such as sewage sludge.<sup>12-14</sup> Additionally, bioethanol aqueous solutions can be directly used, without the need for purification. Compared with water splitting, the production of hydrogen from ethanol is thermodynamically advantageous ( $\Delta G^0 = +237 \text{ kJ}\cdot\text{mol}^{-1}$  for water oxidation vs.  $\Delta G^0 = +41.5 \text{ kJ}\cdot\text{mol}^{-1}$  for ethanol oxidation to acetaldehyde), which decreases the energy input required to drive hydrogen production.<sup>2,8</sup> Compared with water splitting, ethanol dehydrogenation also enables a much simpler product purification, preventing the H<sub>2</sub> and O<sub>2</sub> back reaction. Besides, compared with ethanol photoreforming, ethanol photodehydrogenation to H<sub>2</sub> and acetaldehyde could have a

threefold higher economical profitability associated with the high economic value of the side product.<sup>15</sup>

In terms of catalysts, while photocatalytic water splitting requires semiconductors with conduction and VB edges sufficiently above and below the potentials for H<sup>+</sup> reduction and water oxidation, respectively, ethanol dehydrogenation can be activated in semiconductors with significantly lower band gaps. On the other hand, the catalytic dehydrogenation of ethanol competes with the deoxygenation, reforming, and decomposition reactions, which makes the selectivity of the catalytic process fundamental to ensure cost-effectiveness.<sup>1</sup>

Copper oxides, Cu<sub>2-x</sub>O, have raised increasing attention as photocatalytic materials owing to their abundance, low cost, minor environmental and health impact, and suitable optoelectronic properties. Cu<sub>2-x</sub>O are p-type semiconductors with a very energetic CB and a relatively low bandgap, 2.1 eV for Cu<sub>2</sub>O and 1.2 eV for CuO, that enables absorption of the visible range of the solar spectra. As a drawback, Cu<sub>2-x</sub>O have poor photostability, being prone to photocorrosion in reaction conditions. Besides, Cu<sub>2-x</sub>O generally presents a large defect density that results in a relatively fast recombination of photogenerated charge carriers. To solve these limitations, Cu<sub>2-x</sub>O can be combined with TiO<sub>2</sub> within p-n heterojunctions that protect the Cu<sub>2-x</sub>O against photocorrosion and reduce charge carrier recombination. The synergism between the two materials is enabled by the appropriate CB edges of Cu<sub>2-x</sub>O, -1.79 V for Cu<sub>2</sub>O and -1.03 V for CuO, which allows the rapid injection of the photogenerated electrons from the Cu<sub>2-x</sub>O to the TiO<sub>2</sub> CB.<sup>8,15,16-19</sup> Thus the combination of Cu<sub>2-x</sub>O and TiO<sub>2</sub> is regarded as a highly interesting photocatalyst to: i) stabilize the Cu<sub>2-x</sub>O; ii) boost the overall catalytic activity by extending light absorption of TiO<sub>2</sub> toward the visible light range; and iii) maximize external quantum yield by a rapid charge separation between the two phases enabled by their adequate band edges.

While the concept of a p-n heterojunction between Cu<sub>2-x</sub>O and TiO<sub>2</sub> that promotes catalytic activity is pleasantly simple, real systems are much more complex and Cu<sub>2-x</sub>O have been reported to promote catalytic activity through several different mechanisms: i) Cu<sub>2-x</sub>O can absorb visible light and transfer photogenerated electrons

to TiO<sub>2</sub> where H<sub>2</sub> evolves, while using photogenerated holes to oxidize the organic species;<sup>20</sup> ii) Cu<sub>2-x</sub>O can absorb visible light but use photogenerated electrons to evolve H<sub>2</sub> and recombine photogenerated holes at the Cu<sub>2-x</sub>O/TiO<sub>2</sub> interphase within a Z-scheme mechanism;<sup>21</sup> iii) Cu<sub>2-x</sub>O nanoparticles can be reduced to metallic copper during ethanol photodehydrogenation and the resulting metal nanoparticles can act as co-catalyst, stabilizing photogenerated electrons, promoting the water reduction reaction, simultaneously reducing the rate of charge recombination and thus also making more holes available for the oxidation reaction.<sup>15,22,23</sup> iv) Cu<sup>δ+</sup> and Cu<sup>0</sup> on the surface of supported Cu clusters can also participate as catalysts in the ethanol oxidation to acetaldehyde;<sup>17</sup> v) copper ions can be partially incorporated into the TiO<sub>2</sub> lattice substituting Ti<sup>4+</sup> ions and creating oxygen vacancies that decrease the TiO<sub>2</sub> bandgap.<sup>15,19,24,25</sup> All these effects strongly depend on the synthesis procedure, the TiO<sub>2</sub> surface area and its structural and chemical properties, which affect the Cu dispersion and oxidation state<sup>22</sup>, and the TiO<sub>2</sub> phase that also determines the interaction with Cu and the Cu role.<sup>26</sup>

Most previous works assign the performance promotion of Cu<sub>2-x</sub>O/TiO<sub>2</sub> with respect to TiO<sub>2</sub> to the extension of light absorption toward the visible range of the solar spectra. However, in most previous works mainly UV excitation is used, and the overall and local temperature changes associated with the visible light absorption is usually neglected.

In the present work, we aim at gaining additional understanding of the mechanism behind the synergistic promotion of the catalytic performance in Cu<sub>2</sub>O/TiO<sub>2</sub>, while simultaneously contributing to the optimization of this system. In this direction, we present a one-pot hydrothermal synthesis strategy to produce Cu<sub>2</sub>O/TiO<sub>2</sub> nanocomposites with controlled Cu<sub>2</sub>O amounts. The photocatalytic performance of Cu<sub>2</sub>O/TiO<sub>2</sub> toward ethanol dehydrogenation is tested using both UV and visible light irradiation. We then determine the direct contribution of visible light, beyond increasing temperature, toward increasing catalytic activity. We test photocatalytic activity in the gas phase as it offers additional advantages including lower light scattering, easier scale-up, higher stability, easier product recovery and even higher

selectivity.<sup>7,15</sup> Besides, using time-resolved photoluminescence measurements and analyzing the band alignment between the two materials, we show the activity promotion to proceed through a conventional p-n type II heterojunction.

### **4.3 Materials and Methods**

#### **Chemicals**

Titanium (IV) isopropoxide (97%, Sigma-Aldrich, St. Louis, MI, USA), copper (II) nitrate hexahydrate (98%, Fluka, Buchs, Switzerland), ethanol (96%, PanReac AppliChem GmbH, Darmstadt, Germany), polyvinylpyrrolidone (PVP, 90%, Sigma-Aldrich, St. Louis, MI, USA), and sodium sulfate (Alfa Aesar™, Ward Hill, MA, USA) were used without further purification.

#### **Synthesis of Photocatalysts**

PVP (0.45 g) was dissolved in Milli-Q water:ethanol (1:2) (40 mL) under stirring at room temperature. To this solution, a proper amount of  $\text{Cu}(\text{NO}_3)_2 \cdot 6\text{H}_2\text{O}$  was added (0, 11.3, 22.5, 45 and 112.5 mg to reach 0, 0.5, 1, 2 and 5 at%, respectively) by stirring for 5 min. Then, 2.3 mL of titanium (IV) isopropoxide was added dropwise, followed by stirring for 10 hours at room temperature. Finally, the suspension was transferred to a 50 mL Teflon-lined autoclave and maintained at 170 °C for 14 hours.

#### **Structural and chemical characterization**

The morphology and size of the particles were obtained by transmission electron microscopy (TEM) using a ZEISS LIBRA 120 (Carl Zeiss, Jena, Germany) instrument. Elemental analysis was carried out using an Oxford energy dispersive X-ray spectrometer (EDX) combined with the Zeiss Auriga SEM (Carl Zeiss, Jena, Germany) working at 20.0 kV. The crystal structure of the samples was determined by X-ray diffraction (XRD) using a D8 Advance (Bruker, Billerica, MA, USA) equipment with Ni-filtered  $\text{Cu-K}\alpha$  radiation ( $\lambda = 0.15406 \text{ \AA}$ ) operating at 40 mA and 40 kV. UV-Vis absorption spectra were recorded on a UV-Vis spectrophotometer (Shimadzu, UV-3600i Plus, Japan),  $\text{BaSO}_4$  was used as a reference standard. The spectra were recorded at room temperature in air within the range of 300-800 nm. High-resolution

transmission electron microscopy (HRTEM) images and scanning transmission electron microscopy (STEM) studies were conducted on an FEI Tecnai F20 field emission gun microscope operated at 200 kV with a point-to-point resolution of 0.19 nm, which was equipped with high angle annular dark-field (HAADF) and a Gatan Quantum electron energy loss spectroscopy (EELS) detectors. X-ray photoelectron spectroscopy (XPS) was done on a SPECS system (SPECS GmbH, Berlin, Germany) equipped with an Al anode XR50 source operating at 150 mW and a Phoibos 150 MCD-9 detector (SPECS GmbH, Berlin, Germany). Data processing was performed with the CasaXPS program (Casa Software Ltd., UK). Steady-state photoluminescence (PL) spectra were conducted by a high-resolution photoluminescence spectrofluorometer (Horiba Jobin Yvon Fluorolog-3). For the time-resolved photoluminescence spectroscopy (TRPL) measurements, a nanosecond LED with a 350 nm peak wavelength (Horiba NanoLED N390, France, pulse width < 1.3 ns) was applied to excite the samples. The TRPL decay was resolved at 400 nm. Average lifetimes were obtained by fitting the TPPL spectra with DAS6 software (Horiba).

### **Photoelectrochemical measurements**

Photoelectrochemical (PEC) properties were measured using CHI760e (CHI 760E, CH Instrument, China) in a three-electrode cell with a platinum mesh as the counter electrode and an Ag/AgCl reference electrode. Na<sub>2</sub>SO<sub>4</sub> (0.5 M) was used as the electrolyte solution. The working electrode was prepared by depositing Cu<sub>2</sub>O/TiO<sub>2</sub> on an indium tin oxide (ITO) glass electrode (1 cm×1 cm) and heating at 200 °C for 1 h. Potentials vs. Ag/AgCl were converted into potentials vs. reversible hydrogen electrode (RHE) according to the Nernst equation ( $E_{RHE}=E_{Ag/AgCl}+0.059pH+0.196$ ). Electrochemical impedance spectroscopy (EIS) measurements were carried out with a sinusoidal ac perturbation of 5 mV applied over the frequency range of 0.01–100000 Hz. The transient photocurrent (TPC) of the as-prepared photocatalysts were measured with an AM1.5G solar power system used as the light irradiation source (100 mW·cm<sup>-2</sup>) at an ambient temperature and without any light irradiation source. Mott-Schottky (M-S) measurements were carried out in dark with a scanning speed of bias potential ranging from -1.4 to 0.2 V at a scan rate of 0.01 V s<sup>-1</sup>. The linear sweep

voltammetry was carried out with a scanning speed of bias potential ranging from  $-1.2$  to  $0.6$  V at a scan rate of  $0.01$  V  $s^{-1}$ .

### Photocatalytic test

In a typical experiment, a cellulose paper impregnated with  $2.0$  mg of the photocatalyst was placed inside a photocatalytic reactor that was equipped with UV LEDs ( $365 \pm 5$  nm, from SACOPA S.A.U) (Figure S1). A light irradiation of  $79.1 \pm 0.5$   $mW \cdot cm^{-2}$  was measured for UV light at the sample position. A saturated Ar gas stream was prepared by bubbling dry Ar gas through a Dreschel bottle with a water:ethanol vapor mixture (9:1, molar ratio,  $20$   $mL \cdot min^{-1}$ ). The photoreactor effluent was monitored online every 4 min using gas chromatography (GC) (Agilent 3000A MicroGC) with three columns: MS 5 Å, Plot U and Stabilwax. The system was purged with the saturated Ar stream ( $20$   $mL \cdot min^{-1}$ , 30 min) to remove oxygen before performing the experiments. The UV-visible light source contained two LEDs emitting at  $372 \pm 5$  nm and two LEDs emitting visible light (correlated color temperature (CCT) 6099 K, color rendering index (CRI) 74) in Figure S1. In this system, UV light irradiation was  $11.2 \pm 0.5$   $mW \cdot cm^{-2}$  at the sample position.

### Apparent quantum yield (AQY) calculation.

The AQY was estimated using the following equation:

$$AQY = \frac{2n_{H_2}}{n_p} \cdot 100 = \frac{2nN_A}{E_T/E_p} \cdot 100 \quad (1)$$

where  $n_{H_2}$  is the number of evolved hydrogen molecules and  $n_p$  is the number of incident photons reaching the catalyst. The number of incident photons can be calculated by  $n_p = E_T/E_p$ , where  $E_T$  is the total energy reaching the catalyst and  $E_p$  is the energy of a photon.  $E_T$  can be calculated by  $E_T = PSt$ , where  $P$  ( $W \cdot m^{-2}$ ) is the power density of the incident monochromatic light,  $S$  ( $m^2$ ) is the irradiation area and  $t$  (s) is the duration of the incident light exposure.  $E_p$  can be calculated by  $E_p = hc/\lambda$ , where  $h$  is the Planck's constant,  $c$  the speed of light and  $\lambda$  (m) is the wavelength of the incident monochromatic light. The number of hydrogen molecules can be calculated as  $n_{H_2} = nN_A$ , where  $n$  is  $H_2$  moles evolved during the time of light

exposure (t), and  $N_A$  is the Avogadro constant. In our experimental conditions with UV light, the wavelength of the incident light was  $\lambda = 365$  nm, the power density of the incident light at the paper surface was  $P=79.1$  mW·cm<sup>-2</sup> and the irradiation area was  $S = \pi R^2 = 3.14 \times 0.75^2 = 1.77$  cm<sup>2</sup>.

## 4.4 Results and discussion

### Structural, chemical and optical properties

Cu<sub>2</sub>O/TiO<sub>2</sub> nanocomposites with different Cu<sub>2</sub>O loading, between 0.5 at% and 5 at%, were synthesized by the hydrothermal reaction of copper(II) nitrate hexahydrate and titanium(IV) isopropoxide at 170 °C for 12 h. Figure 1a shows the XRD patterns of the TiO<sub>2</sub> and Cu<sub>2</sub>O/TiO<sub>2</sub> nanopowders. The main XRD peaks of all patterns could be indexed with the tetragonal anatase TiO<sub>2</sub> phase (JCPDS No. 01-071-1167). Additional XRD peaks at  $2\theta=36.4^\circ$  and  $42.3^\circ$  were identified in Cu<sub>2</sub>O/TiO<sub>2</sub> samples containing 1% and higher Cu<sub>2</sub>O amounts and were associated with the (111) and (200) family planes of the cubic Cu<sub>2</sub>O cuprite phase. From the XRD patterns, using the Scherrer equation, the size of the TiO<sub>2</sub> and Cu<sub>2</sub>O crystal domains was calculated to be ca. 7 nm and 50 nm, respectively, which pointed at the presence of some large Cu<sub>2</sub>O crystals.

TEM micrographs showed TiO<sub>2</sub> and Cu<sub>2</sub>O/TiO<sub>2</sub> nanopowders to consist of small nanoparticles with irregular shapes and an average size of ca. 10 nm (Figure 1b, 2a). HRTEM characterization of the 1% composite further confirmed the presence of both the tetragonal anatase TiO<sub>2</sub> and cubic Cu<sub>2</sub>O phases (Figure 1c). STEM-EELS compositional map displayed the elemental distribution (Figure 1d). By performing the quantitative relative compositional analysis we could extrapolate that Ti and O compositions oscillate between 30-35% and 65-70%, respectively. Only traces of Cu could be detected from the 1% composite (Table 1). This limitation and the small size of the Cu<sub>2</sub>O domains observed by HRTEM resulted in STEM-EELS compositional map showing homogeneous-like copper distributions (Figure 1d). SEM-EDX analysis showed the Cu concentration to match the nominal amount in low Cu-loaded samples, but to be lower than expected in 2% and 5% Cu<sub>2</sub>O/TiO<sub>2</sub> nanocomposites (Table 1).

XPS spectra showed the incorporation of Cu not to influence the Ti chemical state (Figure 1e, 2b,c), which displayed the Ti 2p<sub>3/2</sub> and Ti 2p<sub>1/2</sub> binding energies at 458.5 eV and 464.2 eV, respectively, consistent with Ti<sup>4+</sup> within a TiO<sub>2</sub> chemical environment.<sup>27-29</sup> Besides, Cu 2p<sub>3/2</sub> and Cu 2p<sub>1/2</sub> binding energies were 931.9 eV and 951.9 eV, pointing at a Cu<sup>+</sup> chemical state.<sup>30,31</sup> The surface composition of Cu matched the nominal amount of Cu in the 1% Cu<sub>2</sub>O/TiO<sub>2</sub> nanocomposite, but it was lower for the 2% Cu<sub>2</sub>O/TiO<sub>2</sub> nanocomposite, which is in part consistent with SEM-EDX analysis and in part associated to the formation of relatively large Cu<sub>2</sub>O particles when increasing the Cu loading, as observed by XRD.

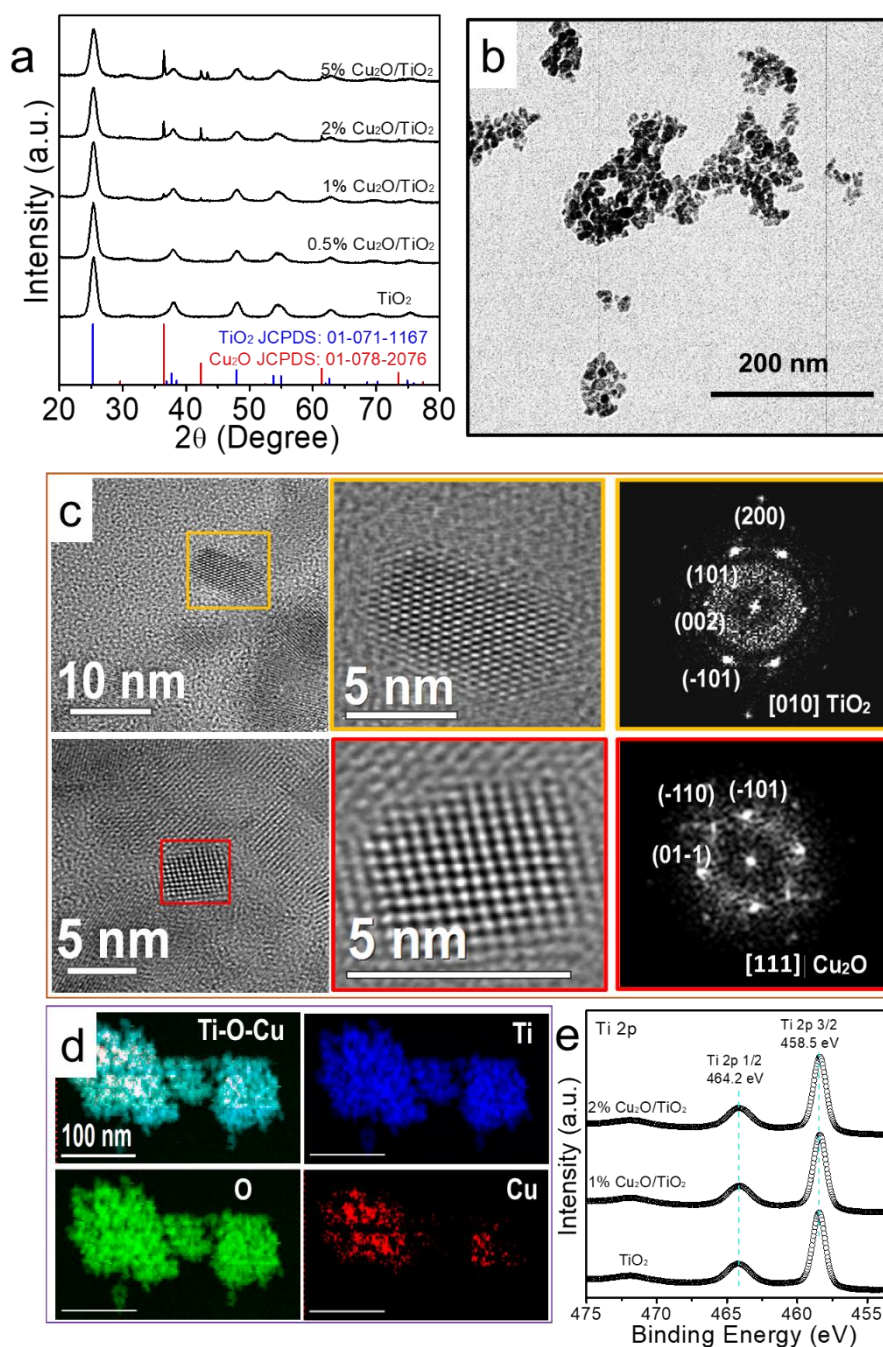


**Figure 1.** (a) Powder XRD pattern of TiO<sub>2</sub> and 0.5%, 1%, 2%, 5% Cu<sub>2</sub>O/TiO<sub>2</sub> nanocomposites. (b) TEM micrograph of 1% Cu<sub>2</sub>O/TiO<sub>2</sub>, with a scale bar of 200nm. (c) HRTEM analysis of the 1% Cu<sub>2</sub>O/TiO<sub>2</sub> sample. The upper image shows a crystal with a tetragonal anatase phase of TiO<sub>2</sub> visualized along the [010] zone axis. The lower image shows a cubic Cu<sub>2</sub>O crystallite visualized along the [111] zone axis. (d) STEM-ADF and STEM-EELS analysis of the 1% Cu<sub>2</sub>O/TiO<sub>2</sub> sample. Cu L-edges at 931 eV (red), O K-edge at 532 eV (green), and Ti L-edge at 456 eV (blue). (e) High resolution XPS spectra for Ti 2p core level of TiO<sub>2</sub>, and 1%, 2% Cu<sub>2</sub>O/TiO<sub>2</sub> nanocomposites.

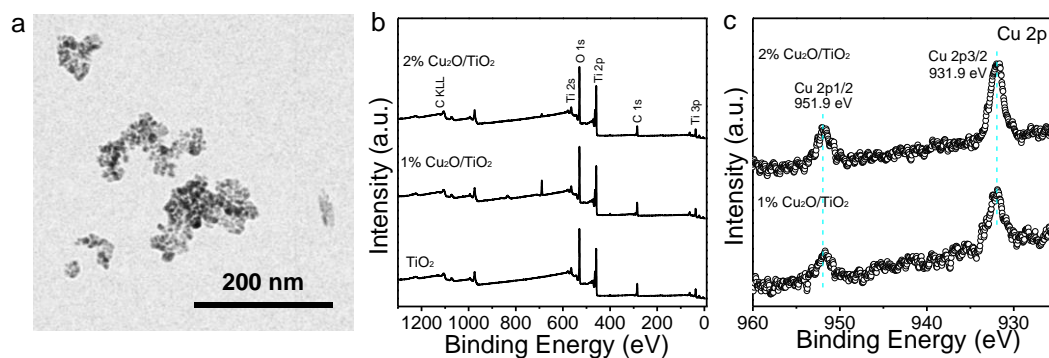


**Figure 2.** (a)TEM micrograph of TiO<sub>2</sub> nanocrystals. (b)Wide XPS spectrum of 0, 1% and 2% Cu<sub>2</sub>O/TiO<sub>2</sub> nanocomposites. (c) High resolution spectra for Cu 2p.

**Table 1.** Ti and Cu atomic concentrations of (1%, 2%, 5%)Cu/Cu<sub>2</sub>O/TiO<sub>2</sub>.

Catalyst	EDX		XPS	
	Ti (at%)	Cu (at%)	Ti (at%)	Cu (at%)
TiO <sub>2</sub>	100		100	
0.5% Cu <sub>2</sub> O/TiO <sub>2</sub>	99.4	0.6		
1% Cu <sub>2</sub> O/TiO <sub>2</sub>	99.1	0.9	98.9	1.1
2% Cu <sub>2</sub> O/TiO <sub>2</sub>	98.8	1.2	99.0	1.0
5% Cu <sub>2</sub> O/TiO <sub>2</sub>	97.1	2.9		

Figure 3 shows the UV-vis spectra of TiO<sub>2</sub> and Cu<sub>2</sub>O/TiO<sub>2</sub> nanopowders and the corresponding Tauc plot calculated as  $(\alpha h\nu)^{1/2}$  vs.  $h\nu$  to determine the direct bandgap of TiO<sub>2</sub> (Figure 3b) and as  $(\alpha h\nu)^2$  vs.  $h\nu$  to determine the indirect bandgap of Cu<sub>2</sub>O (Figure 3c). UV-vis absorption data showed a clear absorption edge at around 3.2 eV consistent with the TiO<sub>2</sub> bandgap. No clear shift of the absorption edge was observed with the introduction of Cu, which rules out a possible bandgap change related to the incorporation of Cu ions within the TiO<sub>2</sub> lattice. Besides, when incorporating Cu<sub>2</sub>O, additional light absorption in the visible region and with an absorption edge of ca. 2.0 eV was clearly observed, consistent with the presence of the Cu<sub>2</sub>O phase.<sup>32</sup>

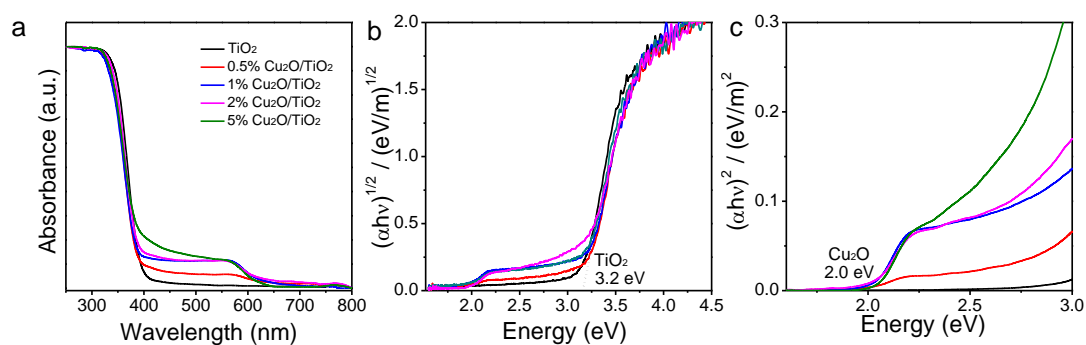


**Figure 3.** UV-vis absorption spectra (a) and Tauc plot calculated as  $(\alpha h\nu)^{1/2}$  vs.  $h\nu$  (b) and as  $(\alpha h\nu)^2$  vs.  $h\nu$  (c) for TiO<sub>2</sub> and 0.5%, 1%, 2%, 5% Cu<sub>2</sub>O/TiO<sub>2</sub> nanocomposites.

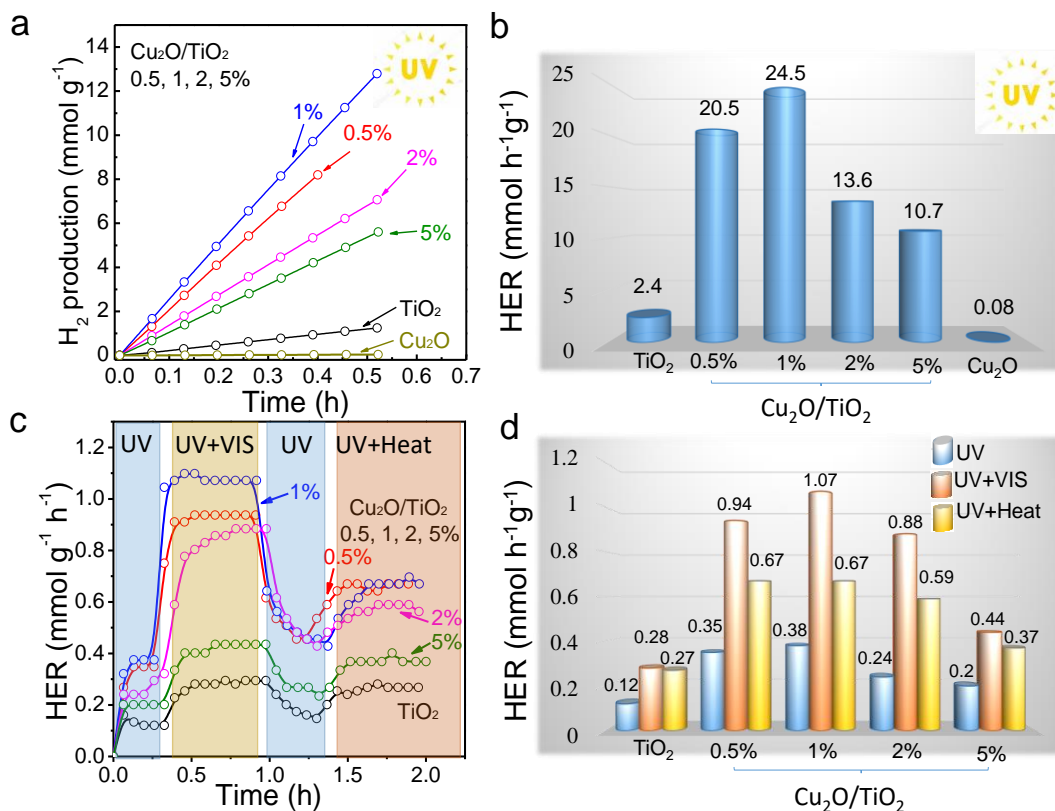
### Photocatalytic activity

Figure 4a,b displays the UV (365 ± 5 nm) photocatalytic activity of TiO<sub>2</sub>, Cu<sub>2</sub>O/TiO<sub>2</sub> and Cu<sub>2</sub>O nanopowders toward hydrogen production from a gas phase 10% ethanol solution in water. The composition of the effluent gas was monitored using gas chromatography, which showed acetaldehyde (2) and hydrogen (3) in a 1:1 molar ratio to be the two unique products of the reaction. These results proved both that the hydrogen was generated from the dehydrogenation of ethanol and not from water splitting, and that the reaction proceeded with very high selectivity toward acetaldehyde production, following the scheme:<sup>33</sup>



The hydrogen evolution rate (HER) measured under UV light for the reference TiO<sub>2</sub> was 2.4 mmol h<sup>-1</sup>·g<sup>-1</sup> (Figure 4a,b). HER strongly increased with the introduction of Cu<sub>2</sub>O (Table 2). Among the series of Cu<sub>2</sub>O/TiO<sub>2</sub> samples tested, the highest HRE were obtained for the 0.5% and 1% Cu<sub>2</sub>O/TiO<sub>2</sub> samples which displayed a HER of 20.5 mol g<sup>-1</sup> h<sup>-1</sup> and 24.5 mmol h<sup>-1</sup>g<sup>-1</sup>, a factor 10 above bare TiO<sub>2</sub>. Higher Cu<sub>2</sub>O loadings resulted in lower HER, 13.6 and 10.7 mmol g<sup>-1</sup> h<sup>-1</sup> for the 2 and 5% samples, respectively. We hypothesise the lower HER obtained when increasing the Cu loading above 1% to be related with an increase of the recombination rate associated with a faster recombination of the charge carriers photogenerated in the Cu<sub>2</sub>O phase than in

the TiO<sub>2</sub> phase. Besides, the formation of larger Cu<sub>2</sub>O domains when increasing the Cu loading could also play an important role. The AQY of the 1% Cu<sub>2</sub>O/TiO<sub>2</sub> was 6.4 %, whereas the AQY for TiO<sub>2</sub>, 0.5, 2, and 5% Cu<sub>2</sub>O/TiO<sub>2</sub> were 0.6%, 5.3%, 3.5% and 2.8%, respectively (Figure 5a). Table 2 displays a comparison of the AQY obtained here with those obtained in previous works. On the other hand, the HER of bare Cu<sub>2</sub>O was very moderate, just 0.8 mmol h<sup>-1</sup>g<sup>-1</sup>, demonstrating both the important role played by TiO<sub>2</sub> in the separation of charge carriers and the synergism between the two materials to optimize photocatalytic activity. Figure 5b displays the HER of the 1% Cu<sub>2</sub>O/TiO<sub>2</sub> sample measured three consecutive times during 1 h, showing the notable HER stability of the system. Besides, in contrast to some previous works, we observed no color change of our samples during photocatalytic reaction in the presence of ethanol.<sup>34,35</sup> It should be noted that beyond the convenient use of aqueous ethanol solutions as produced from biomass processing, the presence of water is beneficial to increase the catalyst activity and stability by preventing active sites to be blocked by acetaldehyde, which exhibits a strong affinity towards inorganic oxide surfaces.<sup>36</sup>



**Figure 4.** (a) Photocatalytic H<sub>2</sub> evolution on TiO<sub>2</sub>, Cu<sub>2</sub>O, 0.5%, 1%, 2%, 5% Cu<sub>2</sub>O/TiO<sub>2</sub> nanocomposites under UV light irradiation (365 ± 5 nm and 79.1 ± 0.5 mW·cm<sup>-2</sup>). (b) HER from data displayed in panel (a). (c) HER measured on TiO<sub>2</sub>, 0.5%, 1%, 2%, 5% Cu<sub>2</sub>O/TiO<sub>2</sub> nanocomposites under different conditions: (1) UV light irradiation (372 ± 5 nm and 11.2 ± 0.5 mW·cm<sup>-2</sup>), (2) UV (372 ± 5 nm and 11.2 ± 0.5 mW·cm<sup>-2</sup>) plus visible light irradiation (0.017 ± 0.005 mW·cm<sup>-2</sup>), (3) UV light irradiation, and (4) UV light irradiation and heating to compensate temperature (~36–37 °C). (d) HER obtained from data displayed in panel (c).

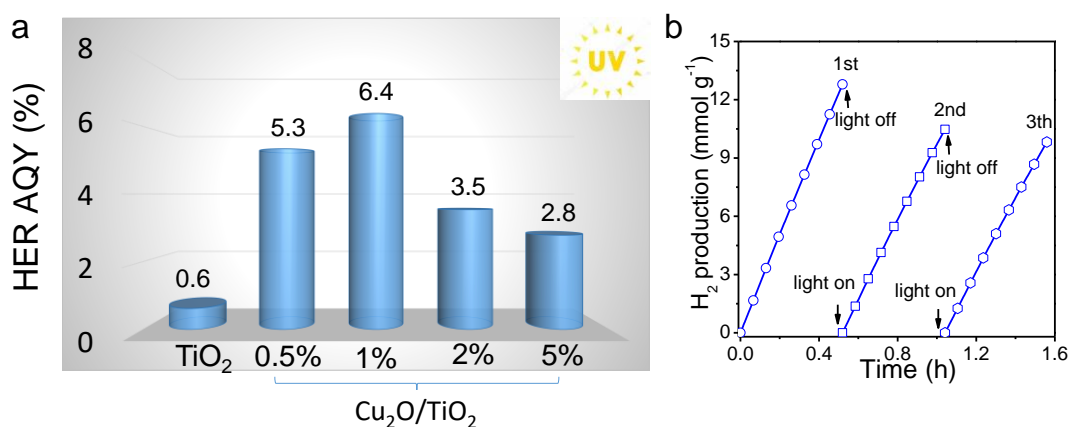


**Figure 5.** (a) AQY data of HER obtained on TiO<sub>2</sub> and (0.5, 1, 2, 5%) Cu<sub>2</sub>O/TiO<sub>2</sub> samples. (b) Three consecutive cycles of photocatalytic hydrogen production under UV light using the same 1%Cu<sub>2</sub>O/TiO<sub>2</sub> sample.

**Table 2.** Comparison of the hydrogen evolution rates and AQY reported on various Cu<sub>2</sub>O-TiO<sub>2</sub> systems.

Photocatalyst	H <sub>2</sub> Evolution Rate μmol h <sup>-1</sup> g <sup>-1</sup>	Illumination Light	AQY	Ref.
5wt%Cu/Cu <sub>2</sub> O/Cu/TiO <sub>2</sub>	3,944	520 nm; 100 mW cm <sup>-2</sup>	45.7%	S1
0.9 mol% Cu <sub>2</sub> O/TiO <sub>2</sub>	318	365 nm	28.6%	S2
Cu <sub>2</sub> O ca.1.5% (Cu <sub>2</sub> O /T1-V <sub>0</sub> )	326,000	350 nm	53.5%	S3
Ag/Cu@Cu <sub>2</sub> O	874.7	365 nm	2.3%	S4
2.5 mol% Cu <sub>2</sub> O/TiO <sub>2</sub>	2,048	365 nm; 3.6 mWcm <sup>-2</sup>	4.32%	S5
Cu/Cu <sub>2</sub> O/CuO/TiO <sub>2</sub>	2,008	100 mW cm <sup>-2</sup>	2.21%	S6
1% Cu <sub>2</sub> O/TiO <sub>2</sub>	24,500	365nm; 79.1 mW cm <sup>-2</sup>	6.4%	This work

Figure 4c shows the photocatalytic HER activities of Cu<sub>2</sub>O/TiO<sub>2</sub> under UV light (372 ± 5 nm) and when combining UV light with visible light or heat (see the experimental section for details). It should be noted that under visible light there is an increase in the temperature of the photocatalyst, thus it is necessary to separate the effect on HER of the temperature increase and the photogenerated charge carriers obtained with the visible light absorption. Thus, the photocatalytic test was divided into four consecutive steps: i) After turning on the UV light, HER began to rise until it stabilized. At this stage the sample temperature was ca. 25 °C; ii) Keeping the UV light on, the visible light was turned on, which increased the HER of all samples. The introduction of visible light also increased the sample temperature, up to ca. 36-37 °C (Table 3); iii) With the UV light on, the visible light was turned off, which resulted in a relatively slow decline of the HER and a temperature decrease down to 25 °C. The slow HER decrease already denoted a significant effect of temperature on the increase of HER observed with the visible light; iv) Finally, still maintaining the UV light on, the reactor was heated to 36-37 °C (Table 3), which also resulted in an increase of the HER for all catalysts. By comparing stages 2 and 4, the effect of temperature and photogenerated

electron-hole pairs can be differentiated.

**Table 3.** Temperature evolution in the photocatalytic reaction of the 0%, 0.5%, 1%, 2%, 5% Cu<sub>2</sub>O/TiO<sub>2</sub> nanocomposites.

Sample	UV Temperature (°C)	UV+Vis Temperature (°C)	UV+heating Temperature (°C)
TiO <sub>2</sub>	24	35	35
0.5% Cu <sub>2</sub> O/TiO <sub>2</sub>	24	37	37
1% Cu <sub>2</sub> O/TiO <sub>2</sub>	25	36	36
2% Cu <sub>2</sub> O/TiO <sub>2</sub>	24	35	35
5% Cu <sub>2</sub> O/TiO <sub>2</sub>	25	37	37

Notice that the addition of visible light increased the HER of TiO<sub>2</sub> by a factor of two, which was associated with a 10 °C increase in temperature (Figure 4c,d). This twofold HER increase points toward the combination of energy sources in thermo-photocatalytic reactors as an efficient strategy of solar energy conversion. Such a strong influence of temperature on HER is likely related to the high adsorption energy of acetaldehyde on the oxide surface, blocking the catalyst active sites and thus slowing down the reaction. A moderate increase in temperature can significantly reduce the acetaldehyde adsorption strength, thus unblocking active sites and increasing activity.<sup>37</sup>

Cu<sub>2</sub>O/TiO<sub>2</sub> catalysts displayed a much higher increase of activity with the addition of visible light (Figure 6), by close to a factor of three in 1% Cu<sub>2</sub>O/TiO<sub>2</sub>. Only a small fraction of this increase in activity can be associated with the increase of temperature, as observed in figure 4c,d. The much larger increase of HER obtained with visible light irradiation compared to the sample heating to the same temperature suggests a significant contribution of photogenerated charge carriers in Cu<sub>2</sub>O.

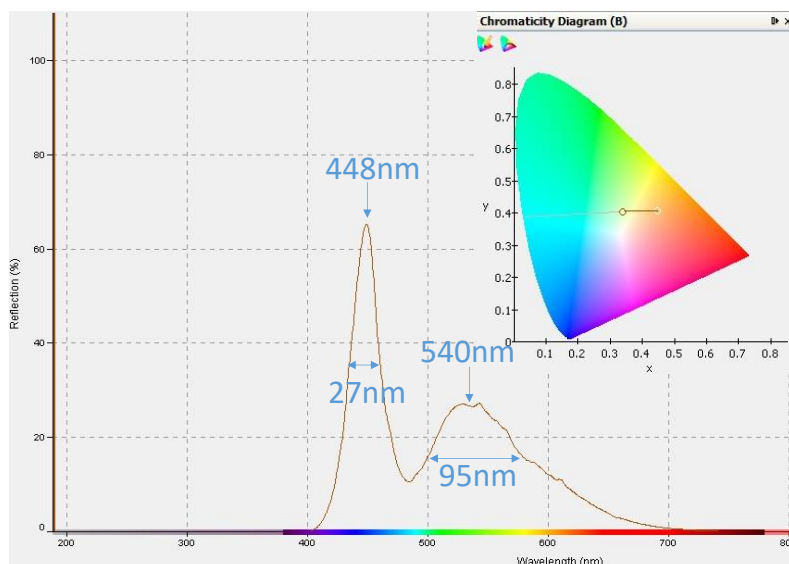


**Figure 6.** The spectra of the visible LEDs used for visible illumination is recorded by ocean optics (USB2000+XR1-ES) with distance 20cm in dark.

The photocatalytic performance of semiconductor photocatalyst is tightly related to their charge transport, separation, and transfer processes, which closely rely on their relative electronic energy level positions. To understand the photocatalytic process and to gain insights from the enhanced performance of  $\text{Cu}_2\text{O}/\text{TiO}_2$  nanocomposites, a series of spectroscopic analysis was performed. Figure 8 displays the steady-state PL spectra of  $\text{TiO}_2$  and 1%  $\text{Cu}_2\text{O}/\text{TiO}_2$ . In both spectra, a peak at around 400 nm, associated with the band-to-band radiative recombination in  $\text{TiO}_2$ , was observed.<sup>38-42</sup> The presence of  $\text{Cu}_2\text{O}$  resulted in a decrease of the peak intensity, which denoted an influence of  $\text{Cu}_2\text{O}$  on the recombination of charge carriers photogenerated in  $\text{TiO}_2$ . Figure 7a displays the TRPL spectra of  $\text{TiO}_2$  and 1%  $\text{Cu}_2\text{O}/\text{TiO}_2$  at 400 nm. The PL intensity of both samples was observed to decay at a similar rate, with an average photocarrier lifetime of 32.3 ns for 1% $\text{Cu}_2\text{O}/\text{TiO}_2$  and 34.0 ns for  $\text{TiO}_2$ . This result demonstrated a minor influence of  $\text{Cu}_2\text{O}$  on the band-to-band recombination within  $\text{TiO}_2$  thus pointing again toward a minor or null influence of Cu within the  $\text{TiO}_2$  lattice.

The photoelectrochemical behavior of  $\text{TiO}_2$  and 1%  $\text{Cu}_2\text{O}/\text{TiO}_2$  samples supported on an ITO-covered glass substrate were measured under dark and  $100 \text{ mW}\cdot\text{cm}^{-2}$  AM 1.5G irradiation. As shown in Figure 7c, the photocurrent density measured for 1%

$\text{Cu}_2\text{O}/\text{TiO}_2$  was higher than that obtained for  $\text{TiO}_2$ . Figure 7b displays the TPC data obtained from  $\text{TiO}_2$  and  $\text{Cu}_2\text{O}/\text{TiO}_2$  composites with different  $\text{Cu}_2\text{O}$  loadings. The 1%  $\text{Cu}_2\text{O}/\text{TiO}_2$  electrode showed the highest photocurrent densities, well above those obtained for bare  $\text{TiO}_2$ . The stable photocurrent of all  $\text{Cu}_2\text{O}/\text{TiO}_2$  samples pointed at a good stability of the composites under illumination in solution. The 5%  $\text{Cu}_2\text{O}/\text{TiO}_2$  sample showed the largest TPC transient spikes indicating the highest degree of surface charge recombination, which is consistent with its lower HER catalytic performance (Figure 4b) and suggests that an excessive amount of  $\text{Cu}_2\text{O}$  hampers the photocatalytic activity due to excessive charge carrier recombination.<sup>43</sup>

Figure 4d displays the Nyquist plot with the EIS data obtained from  $\text{TiO}_2$  and 1%  $\text{Cu}_2\text{O}/\text{TiO}_2$  in the dark and under illumination. EIS analysis showed the 1%  $\text{Cu}_2\text{O}/\text{TiO}_2$  sample to be much less resistive than  $\text{TiO}_2$ ,<sup>44</sup> suggesting that the formation of the heterojunction facilitates the charge transport and injection. Data were fitted with a Randles equivalent circuit consisting of a series resistor  $R_s$ , a bulk resistor  $R_{ct,bulk}$  for charge transport resistance, and a bulk capacitor  $C_{bulk}$  for space charge region capacitance (Table 4).<sup>45</sup> With the incorporation of only 1% of  $\text{Cu}_2\text{O}$ , the value of  $R_{ct,bulk}$  was reduced from  $4.18 \Omega$  to  $15.5 \Omega$  in the dark, and to even lower values under AM1.5G irradiation.

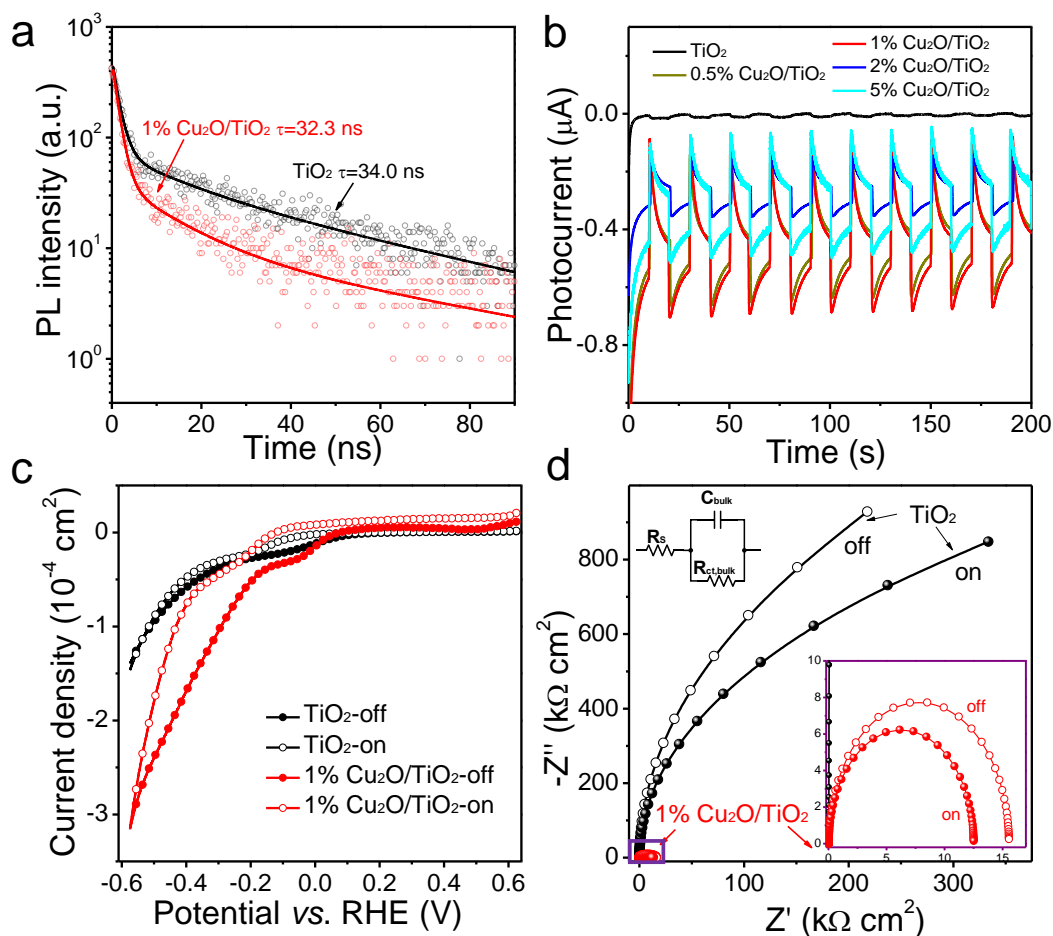


**Figure 7.** (a) TRPL decay of the TiO<sub>2</sub> and 1% Cu<sub>2</sub>O/TiO<sub>2</sub> composite. (b) Transient photocurrent response for TiO<sub>2</sub> and 0.5%, 1%, 2%, 5% Cu<sub>2</sub>O/TiO<sub>2</sub> composites. (c) Current density vs. potential (RHE) and (d) Nyquist plot with the EIS data obtained from TiO<sub>2</sub> and 1% Cu<sub>2</sub>O/TiO<sub>2</sub> composite in the dark (off) and under illumination (on) at AM1.5G solar power system 100 mW·cm<sup>-2</sup> light irradiation.

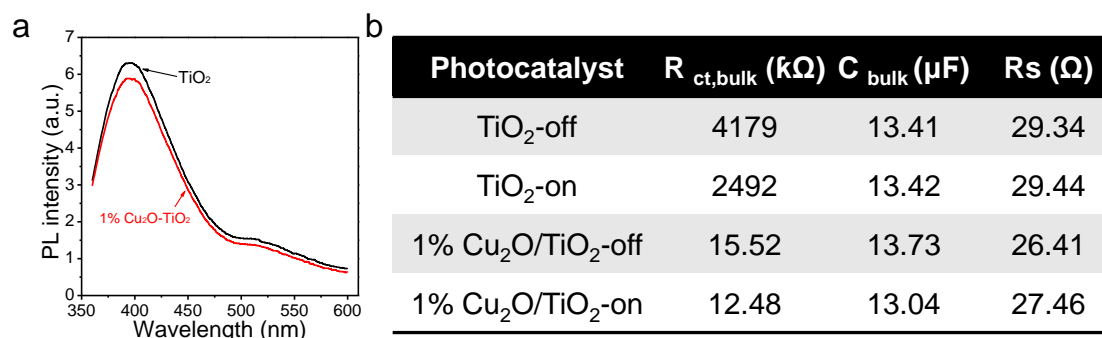


**Figure 8.** (a) Steady-state photoluminescence spectra of TiO<sub>2</sub> and 1%Cu<sub>2</sub>O/TiO<sub>2</sub>. (b) Table 4. EIS data fitting results.

### Determination of heterojunction band position

To determine the band alignment of the Cu<sub>2</sub>O/TiO<sub>2</sub> heterojunction, M–S analysis was performed on pristine TiO<sub>2</sub>, Cu<sub>2</sub>O and 1% Cu<sub>2</sub>O/TiO<sub>2</sub> considering:

$$C^{-2} = \frac{2}{N_D \epsilon \epsilon_0 e} \left( V - V_{fb} - \frac{kT}{e} \right) \quad (4)$$

where C is the space charge capacitance in the semiconductor, N<sub>D</sub> is the electron carrier density, e is the elementary charge (1.60 × 10<sup>-19</sup> C), and ε<sub>0</sub> is the vacuum permittivity (8.85 × 10<sup>-12</sup> F m<sup>-1</sup>). The considered relative permittivities were ε = 55 for TiO<sub>2</sub> and ε = 6.3 for Cu<sub>2</sub>O.<sup>46</sup>

Figure 5a shows the M–S plots of TiO<sub>2</sub>, Cu<sub>2</sub>O and 1% Cu<sub>2</sub>O/TiO<sub>2</sub>. N<sub>D</sub> is determined as:

$$N_D = \frac{2}{e \epsilon_0 \epsilon} \times \left[ \frac{d\left[\frac{1}{C^2}\right]}{dv_s} \right]^{-1} \quad (5)$$

where  $\left[ \frac{d\left[\frac{1}{C^2}\right]}{dv_s} \right]^{-1}$  is the best fit of their linear range of  $\left[ \frac{1}{C^2} \right]$  vs V (12 × 10<sup>9</sup> cm<sup>4</sup>F<sup>-2</sup> for TiO<sub>2</sub> and 9 × 10<sup>10</sup> cm<sup>4</sup>F<sup>-2</sup> for Cu<sub>2</sub>O). As expected, TiO<sub>2</sub> shows a positive value in the linear region in accordance with its n-type character, while Cu<sub>2</sub>O shows a negative value consistent with its p-type behavior.<sup>30</sup> The M–S analysis resulted in N<sub>D</sub> = 2.14 × 10<sup>20</sup> cm<sup>-3</sup> for TiO<sub>2</sub> and N<sub>D</sub> = 2.5 × 10<sup>20</sup> cm<sup>-3</sup> for Cu<sub>2</sub>O (see the support information for additional details).

The effective density of states in the CB (N<sub>C</sub>) is given by:

$$N_C \equiv 2 \left( \frac{2\pi m_{de} kT}{h^2} \right)^{\frac{3}{2}} \quad (6)$$

where m<sub>de</sub> is the density-of-state effective mass for electrons of nano-crystalline anatase TiO<sub>2</sub>, h is Planck's constant (6.62607004 × 10<sup>-34</sup> m<sup>2</sup> kg s<sup>-1</sup>), k is Boltzmann's constant (1.38064852 × 10<sup>-23</sup> m<sup>2</sup> kg s<sup>-2</sup> K<sup>-1</sup>) and T is the absolute temperature (298 K). For TiO<sub>2</sub> a m<sub>de</sub> = 10m<sub>0</sub> is used for N<sub>C</sub> calculations, where m<sub>0</sub> (9.109 × 10<sup>-31</sup>) is the mass of a free electron. For Cu<sub>2</sub>O m<sub>de</sub> = 0.58m<sub>0</sub> is taken as the effective hole mass.

Boltzmann statistics was applied to determine the position of the bottom of the CB

$E_{CB}$  for  $TiO_2$  and the maximum of the VB  $E_{VB}$  for  $Cu_2O$  (3):

$$E - E_F = kT \ln \left( \frac{N_C}{N_D} \right) \quad (7)$$

where  $E_F$  is the Fermi level position ( $E_F = V_{fb}$ ).  $E_F$  was found to be 0.033 eV below the  $E_{CB}$  for  $TiO_2$  and 0.081 eV above the  $E_{VB}$  for  $Cu_2O$ .<sup>47</sup> Based on the M–S analysis, the electronic band structure of  $Cu_2O$  and  $TiO_2$  is displayed in Figure 5c. The  $V_{fb}$  values of  $TiO_2$  and  $Cu_2O$  are -0.44 eV and 0.72 eV vs RHE, respectively. The  $E_{CB}$  for  $TiO_2$  is -0.41 eV and the  $E_{VB}$  for  $Cu_2O$  is 0.64 eV. As the two materials are brought into contact, there is a net transfer of electrons from n-type  $TiO_2$  to p-type  $Cu_2O$  that results in a bending of the band structure at the interface. Because of the small size of the crystal domains, this bending extends through all the whole  $TiO_2$  and  $Cu_2O$  crystals that are in contact with each other. (Figure 9d). In the resulting heterostructure, photogenerated electrons in the CB of  $Cu_2O$  tend to move toward  $TiO_2$ , where hydrogen generation takes place, and photogenerated holes in  $TiO_2$  tend to move toward the  $Cu_2O$ , where ethanol is oxidized to acetaldehyde (Figure 9d).<sup>48,49</sup>

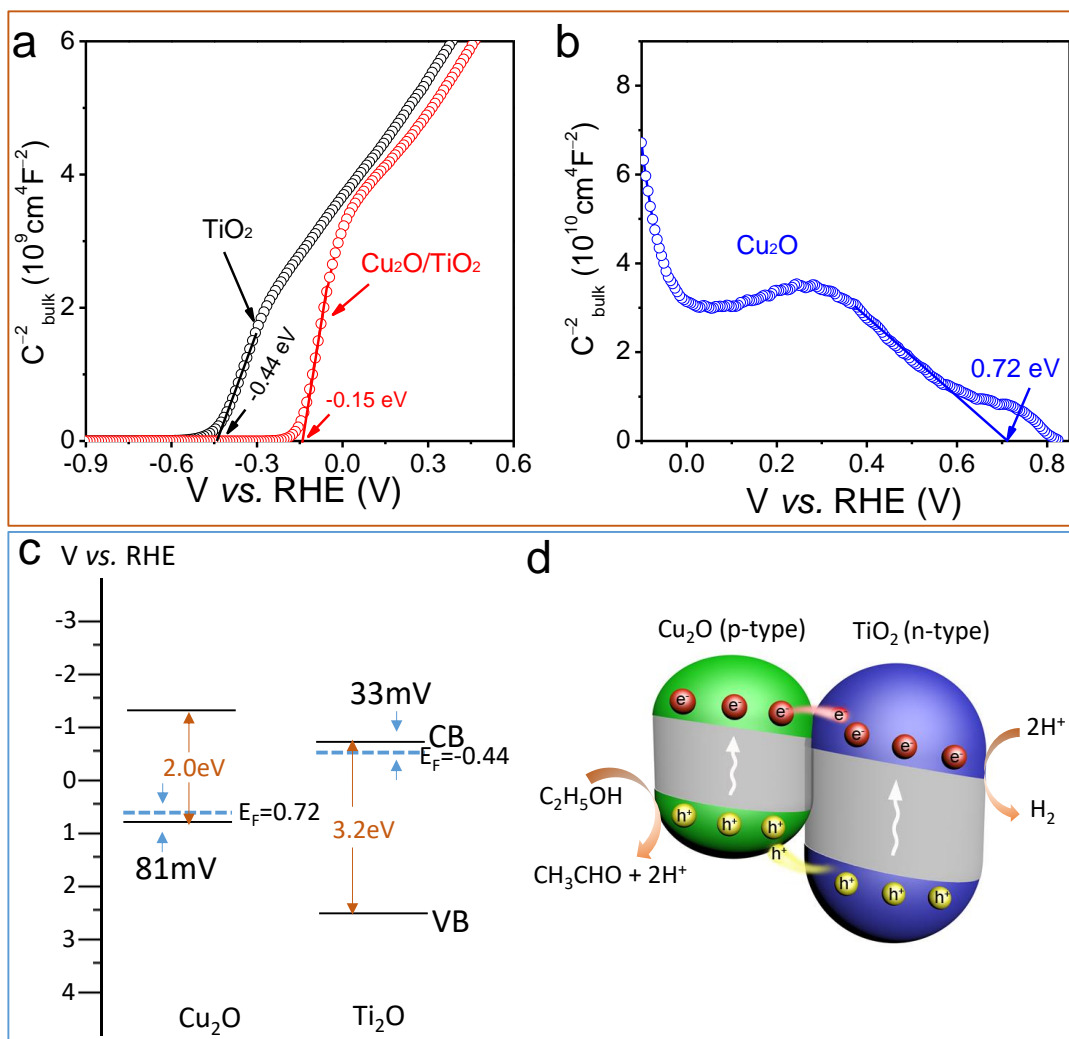


**Figure 9.** (a) M–S analysis of TiO<sub>2</sub> and 1% Cu<sub>2</sub>O/TiO<sub>2</sub>. (b) M–S analysis of Cu<sub>2</sub>O. (c) Energy band diagrams for Cu<sub>2</sub>O and TiO<sub>2</sub> before contact. (d) Scheme of the Energy band structure of a Cu<sub>2</sub>O/TiO<sub>2</sub> heterojunction and the ethanol dehydrogenation reaction.

#### 4.5 Conclusions

A simple one-pot method for the synthesis of p-n Cu<sub>2</sub>O/TiO<sub>2</sub> heterostructures was presented. Using UV-vis spectroscopy and M-S analysis, we showed the formation of a p-n heterojunction between Cu<sub>2</sub>O and TiO<sub>2</sub>, which favors the separation of electron-hole pairs. The obtained nanocomposites at 0.5%, 1%, 2%, and 5% Cu<sub>2</sub>O loading were tested for the photocatalytic dehydrogenation of ethanol in water:ethanol vapor mixture. We demonstrated the composites to be photostable catalysts capable of working in a light absorption towards the visible range, with an outstanding selectivity

to the production of acetaldehyde and hydrogen from ethanol. The optimum composition contained 1% of Cu<sub>2</sub>O and showed a yield for HER of 24.5 mmol g<sup>-1</sup> h<sup>-1</sup> and an AQY = 6.4%. The EIS analysis showed the 1% Cu<sub>2</sub>O/TiO<sub>2</sub> sample to be less resistive than TiO<sub>2</sub> sample and suggested that the heterojunction facilitated the charge transport and injection. The addition of visible light increased the HER of the samples by a factor of two, which was partially associated with an increment in the reaction temperature of around 10°C. We further discerned the influence of temperature and photogenerated electron-hole pairs in the HER increase upon visible light irradiation, demonstrating the important role of photogenerated charge carriers in the presence of Cu<sub>2</sub>O. Besides, our results open new opportunities for efficient solar energy conversion by the combination of energy sources in thermo-photocatalytic reactors.

#### 4.6 References

1. Huang, Y.; Wang, B.; Yuan, H.; Sun, Y.; Yang, D.; Cui, X.; Shi, F. The Catalytic Dehydrogenation of Ethanol by Heterogeneous Catalysts. *Catal. Sci. Technol.* 2021, 11, 1652–1664.
2. Puga, A. V Photocatalytic Production of Hydrogen from Biomass-Derived Feedstocks. *Coord. Chem. Rev.* 2016, 315, 1–66.
3. Fujishima, A.; Honda, K. Electrochemical Photolysis of Water at a Semiconductor Electrode. *Nature* 1972, 238, 37–38.
4. Sadanandam, G.; Lalitha, K.; Kumari, V.D.; Shankar, M. V.; Subrahmanyam, M. Cobalt Doped TiO<sub>2</sub>: A Stable and Efficient Photocatalyst for Continuous Hydrogen Production from Glycerol: Water Mixtures under Solar Light Irradiation. *Int. J. Hydrogen Energy* 2013, 38, 9655–9664.
5. Barakat, M.A.; Schaeffer, H.; Hayes, G.; Ismat-Shah, S. Photocatalytic Degradation of 2-Chlorophenol by Co-doped TiO<sub>2</sub> Nanoparticles. *Appl. Catal. B Environ.* 2005, 57, 23–30.
6. Nakhate, G.G.; Nikam, V.S.; Kanade, K.G.; Arbuj, S.; Kale, B.B.; Baeg, J.O. Hydrothermally Derived Nanosized Ni-doped TiO<sub>2</sub>: A Visible Light Driven Photocatalyst for Methylene Blue Degradation. *Mater. Chem. Phys.* 2010, 124, 976–981.
7. Ampelli, C.; Genovese, C.; Passalacqua, R.; Perathoner, S.; Centi, G. A gas-phase reactor powered by solar energy and ethanol for H<sub>2</sub> production. *Appl. Therm. Eng.* 2014, 70, 1270–1275.
8. Ying Toe, C.; Tsounis, C.; Zhang, J.; Masood, H.; Gunawan, D.; Scott, J.; Amal, R. Advancing Photoreforming of Organics: Highlights on Photocatalyst and System Designs for Selective Oxidation Reactions. *Energy Environ. Sci.* 2021, 14, 1140.

9. Montini, T.; Gombac, V.; Sordelli, L.; Delgado, J.J.; Chen, X.; Adami, G.; Fornasiero, P. Nanostructured Cu/TiO<sub>2</sub> Photocatalysts for H<sub>2</sub> Production from Ethanol and Glycerol Aqueous Solutions. *ChemCatChem* 2011, 3, 574–577.
10. Sangpour, P.; Hashemi, F.; Moshfegh, A.Z. Photoenhanced Degradation of Methylene Blue on Cosputtered M:TiO<sub>2</sub> (M = Au, Ag, Cu) Nanocomposite Systems: A Comparative Study. *J. Phys. Chem. C* 2010, 114, 13955–13961.
11. Dong, Z.; Ding, D.; Li, T.; Ning, C. Ni-doped TiO<sub>2</sub> Nanotubes Photoanode for Enhanced Photoelectrochemical Water Splitting. *Appl. Surf. Sci.* 2018, 443, 321–328.
12. Sarkar, N.; Ghosh, S.K.; Bannerjee, S.; Aikat, K. Bioethanol Production from Agricultural Wastes: An Overview. *Renew. Energ.* 2012, 37, 19–27.
13. Zabed, H.; Sahu, J.N.; Suely, A.; Boyce, A.N.; Faruq, G. Bioethanol Production from Renewable Sources: Current Perspectives and Technological Progress. *Renew. Sust. Energ. Rev.* 2017, 71, 475–501.
14. Rulkens, W. Sewage Sludge as a Biomass Resource for the Production of Energy: Overview and Assessment of the Various Options. *Energy Fuels* 2008, 22, 9–15.
15. Ampelli, C.; Passalacqua, R.; Genovese, C.; Perathoner, S.; Centi, G.; Montini, T.; Gombac, V.; Delgado Jaen, J.J.; Fornasiero, P. H<sub>2</sub> Production by Selective Photo-Dehydrogenation of Ethanol in Gas and Liquid Phase on CuO<sub>x</sub>/TiO<sub>2</sub> Nanocomposites. *RSC Adv.* 2013, 3, 21776–21788.
16. Muscetta, M.; Andreozzi, R.; Clarizia, L.; Di Somma, I.; Marotta, R. Hydrogen Production through Photoreforming Processes over Cu<sub>2</sub>O/TiO<sub>2</sub> Composite Materials: A Mini-Review. *Int. J. Hydrog. Energy* 2020, 45, 28531–28552.
17. Christoforidis, K.C.; Fornasiero, P. Photocatalysis for Hydrogen Production and CO<sub>2</sub> Reduction: The Case of Copper-Catalysts. *ChemCatChem* 2019, 11, 368–382.
18. Li, H.; Zhou, J.; Feng, B. Facile Synthesis of Cu<sub>x</sub>O (x = 1, 2)/TiO<sub>2</sub> Nanotube Arrays as an Efficient Visible-Light Driven Photocatalysts. *J. Porous Mater.* 2017, 24, 97–102.
19. Kubacka, A.; Muñoz, M.J.; Muñoz-Batista, M.; Fernández-García, M.; Obregón, S.; Colón, G. Evolution of H<sub>2</sub> Photoproduction with Cu Content on CuO<sub>x</sub>-TiO<sub>2</sub> Composite Catalysts Prepared by a Microemulsion Method. *Appl. Catal. B Environ.* 2015, 163, 214–222.
20. Sorcar, S.; Yoriya, S.; Lee, H.; Grimes, C.A.; Feng, S.P. A Review of Recent Progress in Gas Phase CO<sub>2</sub> Reduction and Suggestions on Future Advancement. *Mater. Today Chem.* 2020, 16, 100264.
21. Xing J.; Chen Z.P.; Xiao F.Y.; Ma X.Y.; Wen C.Z.; Li Z.; Yang H.G. Cu-Cu<sub>2</sub>O-TiO<sub>2</sub> Nanojunction Systems with an Unusual Electron-Hole Transportation Pathway and Enhanced Photocatalytic Properties. *Chem. Asian J.* 2013, 8, 1265–1270.
22. Obregón, S.; Muñoz, M.J.; Muñoz-Batista, M.; Fernández-García, M.; Kubacka, A.; Colón, G. Cu-TiO<sub>2</sub> Systems for the Photocatalytic H<sub>2</sub> Production: Influence of Structural and Surface Support Features. *Appl. Catal. B Environ.* 2015, 179, 468–478.
23. Bonmatí, E.; Casanovas, A.; Angurell, I.; Llorca, J. Hydrogen Photoproduction from Ethanol-Water Mixtures over Au-Cu Alloy Nanoparticles Supported on TiO<sub>2</sub>. *Top.*

- Catal.* 2015, 58, 77–84.
24. Sahu, M.; Biswas, P. Single-Step Processing of Copper-Doped Titania Nanomaterials in a Flame Aerosol Reactor. *Nanoscale Res. Lett.* 2011, 6, 441.
  25. Brant, A.T.; Yang, S.; Giles, N.C.; Iqbal, M.Z.; Manivannan, A.; Halliburton, L.E. Oxygen Vacancies Adjacent to Cu<sup>2+</sup> ions in TiO<sub>2</sub> (rutile) Crystals. *J. Appl. Phys.* 2011, 109, 073711.
  26. Liu, Y.; Wang, Z.; Huang, W. Influences of TiO<sub>2</sub> Phase Structures on the Structures and Photocatalytic Hydrogen Production of CuO<sub>x</sub>/TiO<sub>2</sub> Photocatalysts. *Appl. Surf. Sci.* 2016, 389, 760–767.
  27. Losito, I.; Amorisco, A.; Palmisano, F.; Zambonin, P.G. X-ray Photoelectron Spectroscopy Characterization of Composite TiO<sub>2</sub>-Poly(vinylidene fluoride) Films Synthesised for Applications in Pesticide Photocatalytic Degradation. *Appl. Surf. Sci.* 2005, 240, 180–188.
  28. Xu, Y.-H.; Chen, H.-R.; Zeng, Z.-X.; Lei, B. Investigation on Mechanism of Photocatalytic Activity Enhancement of Nanometer Cerium-doped Titania. *Appl. Surf. Sci.* 2006, 252, 8565–8570.
  29. Xu, Y.-H.; Liang, D.-H.; Liu, M.-L.; Liu, D.-Z. Preparation and Characterization of Cu<sub>2</sub>O-TiO<sub>2</sub>: Efficient Photocatalytic Degradation of Methylene Blue. *Mater. Res. Bull.* 2008, 43, 3474–3482.
  30. Aguirre, M.E.; Zhou, R.; Eugene, A.J.; Guzman, M.I.; Grela, M.A. Cu<sub>2</sub>O/TiO<sub>2</sub> Heterostructures for CO<sub>2</sub> Reduction through a Direct Z-scheme: Protecting Cu<sub>2</sub>O from Photocorrosion. *Appl. Catal. B Environ.* 2017, 217, 485–493.
  31. Poulston, S.; Parlett, P.M.; Stone, P.; Bowker, M. Surface Oxidation and Reduction of CuO and Cu<sub>2</sub>O Studied Using XPS and XAES. *Surf. Interface Anal.* 1996, 24, 811–820.
  32. Xu, X.; Gao, Z.; Cui, Z.; Liang, Y.; Li, Z.; Zhu, S.; Yang, X.; Ma, J. Synthesis of Cu<sub>2</sub>O Octadecahedron/TiO<sub>2</sub> Quantum Dot Heterojunctions with High Visible Light Photocatalytic Activity and High Stability. *ACS Appl. Mater. Interfaces* 2016, 8, 91–101.
  33. Murdoch, M.; Waterhouse, G.I.N.; Nadeem, M.A.; Metson, J.B.; Keane, M.A.; Howe, R.F.; Llorca, J.; Idriss, H. The Effect of Gold Loading and Particle Size on Photocatalytic Hydrogen Production from Ethanol over Au/TiO<sub>2</sub> Nanoparticles. *Nat. Chem.* 2011, 3, 489–492.
  34. Kong, L.; Jiang, Z.; Wang, C.; Wan, F.; Li, Y.; Wu, L.; Zhi, J.-F.; Zhang, X.; Chen, S.; Liu, Y. Simple Ethanol Impregnation Treatment Can Enhance Photocatalytic Activity of TiO<sub>2</sub> Nanoparticles under Visible-Light Irradiation. *ACS Appl. Mater. Interfaces* 2015, 7, 7752–7758.
  35. Lettieri, S.; Gargiulo, V.; Alfè, M.; Amati, M.; Zeller, P.; Maraloiu, V.-A.; Borbone, F.; Pavone, M.; Muñ Oz-García, A. B.; Maddalena, P. Simple Ethanol Refluxing Method for Production of Blue-Colored Titanium Dioxide with Oxygen Vacancies and Visible Light-Driven Photocatalytic Properties. *J. Phys. Chem. C* 2020, 124, 3564–3576.
  36. Guil, J.M.; Homs, N.; Llorca, J.; De La Piscina, P.R. Microcalorimetric and Infrared

- Studies of Ethanol and Acetaldehyde Adsorption to Investigate the Ethanol Steam Reforming on Supported Cobalt Catalysts. *J. Phys. Chem. B*, 2005, 109, 10813–10819.
37. Castedo, A.; Casanovas, A.; Angurell, I.; Soler, L.; Llorca, J. Effect of Temperature on the Gas-Phase Photocatalytic H<sub>2</sub> Generation using Microreactors under UVA and Sunlight Irradiation. *Fuel*, 2018, 222, 327–333.
  38. Yu, Y.; Wen, W.; Qian, X.-Y.; Liu, J.-B.; Wu, J.-M. UV and visible light photocatalytic activity of Au/TiO<sub>2</sub> nanoforests with Anatase/Rutile phase junctions and controlled Au locations. *Sci. Rep.* 2017, 7, 41253.
  39. Xu, J.; Li, L.; Yan, Y.; Wang, H.; Wang, X.; Fu, X.; Li, G. Synthesis and Photoluminescence of Well-Dispersible Anatase TiO<sub>2</sub> Nanoparticles. *J. Colloid Interface Sci.* 2008, 318, 29–34.
  40. Yadav, H. M.; Kim, J.-S. Solvothermal Synthesis of Anatase TiO<sub>2</sub>-Graphene Oxide Nanocomposites and Their Photocatalytic Performance. *J. Alloys Compd.* 2016, 688, 123–129.
  41. Abazović, N. D.; Čomor, M. I.; Dramićanin, M. D.; Jovanović, D. J.; Ahrenkiel, S. P.; Nedeljković, J. M. Photoluminescence of Anatase and Rutile TiO<sub>2</sub> Particles. *J. Phys. Chem. B* 2006, 110, 25366–25370.
  42. Chen, Y.; Wang, Y.; Li, W.; Yang, Q.; Hou, Q.; Wei, L.; Liu, L.; Huang, F.; Ju, M. Enhancement of Photocatalytic Performance with the use of Noble-Metal-Decorated TiO<sub>2</sub> Nanocrystals as Highly Active Catalysts for Aerobic Oxidation under Visible-Light Irradiation. *Appl. Catal. B Environ.* 2017, 210, 352–367.
  43. Xing, C.; Liu, Y.; Zhang, Y.; Wang, X.; Guardia, P.; Yao, L.; Han, X.; Zhang, T.; Arbiol, J.; Soler, L.; Chen Y.; Sivula K.; Guijarro N.; Cabot A. and Llorca J. A Direct Z-Scheme for the Photocatalytic Hydrogen Production from a Water Ethanol Mixture on CoTiO<sub>3</sub>/TiO<sub>2</sub> Heterostructures. *ACS Appl. Mater. Interfaces* 2021, 13, 449–457.
  44. Liu, Y.; Le Formal, F.; Boudoire, F.; Guijarro, N. Hematite Photoanodes for Solar Water Splitting: A Detailed Spectroelectrochemical Analysis on the pH-Dependent Performance. *ACS Appl. Energy Mater.* 2019, 2, 6825–6833.
  45. Zuo, Y.; Liu, Y.; Li, J.; Du, R.; Han, X.; Zhang, T.; Arbiol, J.; Divins, N.J.; Llorca, J.; Guijarro, N. Sivula K.; Cabot A. In Situ Electrochemical Oxidation of Cu<sub>2</sub>S into CuO Nanowires as a Durable and Efficient Electrocatalyst for Oxygen Evolution Reaction. *Chem. Mater.* 2019, 31, 7732–7743.
  46. Lahmar, H.; Setifi, F.; Azizi, A.; Schmerber, G.; Dinia, A. On the Electrochemical Synthesis and Characterization of p-Cu<sub>2</sub>O/n-ZnO heterojunction. *J. Alloys Compd.* 2017, 718, 36–45.
  47. Hsu, Y.-K.; Yu, C.-H.; Chen, Y.-C.; Lin, Y.-G. Synthesis of novel Cu<sub>2</sub>O micro/nanostructural photocathode for solar water splitting. *Electrochim. Acta* 2013, 105, 62–68.
  48. Wang, Y.; Wang, Q.; Zhan, X.; Wang, F.; Safdar, M.; He, J. Visible Light Driven Type II Heterostructures and Their Enhanced Photocatalysis Properties: A review. *Nanoscale* 2013, 5, 8326–8339.
  49. Rawool, S.A.; Pai, M.R.; Banerjee, A.M.; Arya, A.; Ningthoujam, R.S.; Tewari, R.;

- Rao, R.; Chalke, B.; Ayyub, P.; Tripathi, A.K.; Bharadwaj, S.R. pn Heterojunctions in NiO:TiO<sub>2</sub> composites with type-II band alignment assisting sunlight driven photocatalytic H<sub>2</sub> generation. *Appl. Catal. B Environ.* **2018**, *221*, 443–458.
- S1. Zhen, W.; Jiao, W.; Yuqi Wu.; Jing, H.; Lu, G. The Role of a Metallic Copper Interlayer during Visible Photocatalytic Hydrogen Generation over a Cu/Cu<sub>2</sub>O/Cu/TiO<sub>2</sub> Catalyst. *Cite this Catal. Sci. Technol* **2017**, *7*, 5028.
- S2. Li, L.; Xu, L.; Shi, W.; Guan, J. Facile Preparation and Size-Dependent Photocatalytic Activity of Cu<sub>2</sub>O Nanocrystals Modified Titania for Hydrogen Evolution. *Int. J. Hydrog. Energy* **2012**, *38*, 816–822.
- S3. Wei, T.; Zhu, Y.-N.; An, X.; Liu, L.-M.; Cao, X.; Liu, H.; Qu, J. Defect Modulation of Z-Scheme TiO<sub>2</sub>/Cu<sub>2</sub>O Photocatalysts for Durable Water Splitting. *ACS Catal.* **2019**, *9*, 8346–8354.
- S4. Fu, J.; Cao, S.; Yu, J. Dual Z-Scheme Charge Transfer in TiO<sub>2</sub>–Ag–Cu<sub>2</sub>O Composite for Enhanced Photocatalytic Hydrogen Generation. *J. Mater.* **2015**, *1* (2), 124–133.
- S5. Li, Y.; Wang, B.; Liu, S.; Duan, X.; Hu, Z. Synthesis and Characterization of Cu<sub>2</sub>O/TiO<sub>2</sub> Photocatalysts for H<sub>2</sub> Evolution from Aqueous Solution with Different Scavengers. *Appl. Surf. Sci.* **2015**, *324*, 736–744.
- S6. Zhang, Z.; Liu, K.; Bao, Y.; Dong B. Photo-assisted self-optimizing of charge-carriers transport channel in the recrystallized multi heterojunction nanofibers for highly efficient photocatalytic H<sub>2</sub> generation. *Appl. Catal. B Environ.* **2017**, *203*, 599–606.

## Result and Discussions

Energy crisis and environmental pollution are the two major problems facing the development of human society today. Solar energy is the most abundant clean and renewable energy. Therefore, photocatalytic technology has great interest owing to its potential in the utilization and even storage of solar energy. The efficient utilization of solar energy requires the design and preparation of high-efficiency photocatalysts. However, the efficiency of a single photocatalyst is very low, the strong coulomb attraction of photo-generated electrons and holes leads to their rapid recombination. In addition, it is difficult for a single photocatalyst to have both broad-spectrum absorption and sufficient redox capacity. To solve this problem, constructing a heterojunction photocatalyst has become an effective way because it can realize the effective separation of photogenerated electrons and holes in space.

TiO<sub>2</sub> is the prototype photocatalyst due to its outstanding optoelectronic properties, natural abundance, high photo-corrosion resilience, lack of toxicity, and low cost. However, TiO<sub>2</sub> practical application is hampered by its large band gap, which limits the range of solar spectra used. In order to improve the light absorption performance, the photocatalyst should have a smaller band gap, and in order to obtain a higher redox ability, it has to have a higher CB energy level and a lower VB energy level. Here, we present a simple, high throughput, and scalable hydrothermal-based strategy to produce heterostructures, such as Cu<sub>2</sub>O/TiO<sub>2</sub>, CoTiO<sub>3</sub>/TiO<sub>2</sub> and NiTiO<sub>3</sub>/TiO<sub>2</sub>.

Ti-based mixed oxides and particularly perovskite titanates MTiO<sub>3</sub> (M=Ba, Sr, Co, and Ni) are an exciting class of photoactive materials. Perovskite MTiO<sub>3</sub> semiconductor materials have a narrow band gap ( $E_g = 2.1-2.3$  eV), and they can undergo electronic transitions under visible light irradiation to generate electron-hole pairs. Subsequently, the electrons and holes are separated to form charge carriers that migrate to the surface of the material and react with the substances adsorbed on the surface. Thus, MTiO<sub>3</sub> can be combined with TiO<sub>2</sub> to build suitable photocatalysis.

In conventional Type-II heterojunctions, under light conditions, electrons can be transferred from PC 1 to PC 2 after electron-hole pairs are generated, and the photo-

generated holes move in the opposite direction. But this mechanism has some fundamental problems, which directly affect its practical application. 1) thermodynamic, the efficiency of photo-generated electron-hole separation comes at the cost of reducing the oxidation/reduction capacity of the two semiconductor photocatalysts. For certain specific reactions, a certain oxidation-reduction potential is required to drive, so this is not conducive to the occurrence of photocatalytic reactions. 2) perspective of kinetics: due to the existence of electrostatic interaction, the existence of photogenerated electron holes in the original photocatalyst will inhibit the interface transfer of electron holes in other catalysts. Here, we built p-n type-II  $\text{Cu}_2\text{O}/\text{TiO}_2$ , this heterostructure determined the direct contribution of visible light, beyond the increasing temperature, toward increasing catalytic activity. We also tested photocatalytic activity in the gas phase as it offers additional advantages, including lower light scattering, easier scale-up, higher stability, easier product recovery and even higher selectivity.

In the traditional Z-scheme mechanism, the charge transfer between the two semiconductors is achieved through redox electron mediator pairs, and these ions can only achieve a sufficient migration rate in the solution. After light excites the two semiconductors to generate electron holes, the photogenerated holes of PC 1 react with the electron donor to generate an electron acceptor, while the photogenerated electrons of PC 2 react with the electron acceptor to generate an electron donor. The electron holes in the two semiconductors are retained to participate in the redox reaction. This makes the system limited to the reaction of the solution phase. Unpredictable side reactions may occur, as shown in the figure. Due to the greater potential difference, the electrons in PC 1 may react with the electron acceptors, and the holes in PC 2 may react with the electron donors, which may interfere with the charge transfer process. Redox mediators may be colored, such as ferrous/ferric, which interferes with the light absorption of the semiconductor catalyst.

The synthesis of  $\text{NiTiO}_3$  and  $\text{CoTiO}_3$  have mainly divided into two steps: 1) synthesis needle bundles of Ni and Co-doped  $\text{TiO}_2$  ( $\text{TiO}_2:\text{Ni}$  and  $\text{Co}$ ) and 2) their posterior sintering in the air to produce highly crystalline  $\text{NiTiO}_3/\text{TiO}_2$  and  $\text{CoTiO}_3/\text{TiO}_2$

heterostructures. The benefits of this synthesis strategy include: 1) Enables the metal to be uniformly doped in the TiO<sub>2</sub> nanoparticles. 2) During the calcination process, the metal can combine with TiO<sub>2</sub> to form NiTiO<sub>3</sub> and CoTiO<sub>3</sub>. As a result, the size of NiTiO<sub>3</sub> and CoTiO<sub>3</sub> nanoparticles is small and can be evenly distributed on the surface of TiO<sub>2</sub>. Formally, because part of Ti comes from TiO<sub>2</sub>, CoTiO<sub>3</sub>/TiO<sub>2</sub> and NiTiO<sub>3</sub>/TiO<sub>2</sub> is the construction of heterojunction can be tightened.

In addition, the synthesis of mixed oxides and oxide heterostructures in the form of high surface area materials remains an extremely challenging endeavor, which has limited further advances in this direction. Here, porous NiTiO<sub>3</sub>/TiO<sub>2</sub> was generated during the sintering of the nanostructured bundles due to the presence of a large density of interfaces on the precursor material. Our work proves that this porous NiTiO<sub>3</sub>/TiO<sub>2</sub> heterostructure is excellent photocatalysts for hydrogen generation.

Table1. Summary study of Cu<sub>2</sub>O/TiO<sub>2</sub>, CoTiO<sub>3</sub>/TiO<sub>2</sub> and NiTiO<sub>3</sub>/TiO<sub>2</sub>.

Photocatalysts	Light absorption range (eV)	HER rate (mmol·h <sup>-1</sup> ·g <sup>-1</sup> )	Heterostructure HER Mechanism	Influence of visible light / temperature	Stable
TiO <sub>2</sub>	>3.0	2.0	-	✓	✓
Cu <sub>2</sub> O/TiO <sub>2</sub>	>2.0	24.5	Type-II	✓	✓
CoTiO <sub>3</sub> /TiO <sub>2</sub>	>2.6	3.7	Direct Z-Scheme	✓	✓
NiTiO <sub>3</sub> /TiO <sub>2</sub>	>2.5	11.5	Direct Z-Scheme	✓	✓
Cu <sub>2</sub> O	>2.0	0.08	-	-	✗
CoTiO <sub>3</sub>	>2.3	0.3	-	-	✓
NiTiO <sub>3</sub>	>2.3	0.2	-	-	✓

There are some shortcomings and limitations of the Z-scheme and type-II photocatalyst. 1) The scope of application is limited, currently mainly limited to the application of powder photocatalysts, not suitable for photoelectric catalysis and solar cells with external circuits. 2) The two semiconductors constituting the type-II and Z-

scheme system are mainly n-type semiconductors, which should have a suitable energy band structure and a significant fermi level difference. Meanwhile, the highest efficiency of using heterojunction is only 50%, since have of the charge carriers recombine. Thus, solving problems brings new problems at the same time. This may be the course of scientific development.

## Conclusions

In this thesis, we demonstrate that NiTiO<sub>3</sub>, CoTiO<sub>3</sub> and Cu<sub>2</sub>O cocatalysts can substantially promote local spatial charge separation and proton activation in TiO<sub>2</sub>, achieving high-efficiency for H<sub>2</sub> photoproduction. Ethanol is more easily oxidized than water by holes in the VB of photoexcited semiconductors, suppressing the recombination of electron-hole pairs and, therefore, increasing the reactivity of electrons in the CB of photoexcited semiconductors to yield hydrogen. The main conclusions can be summarized as follows:

- 1) Porous NiTiO<sub>3</sub>/TiO<sub>2</sub> heterostructures were prepared from the annealing in air of TiO<sub>2</sub>:Ni nanoneedle bundles obtained from a hydrothermal route. Pores were generated during the sintering of the nanostructured bundles due to the presence of a large density of interfaces on the precursor material.
- 2) NiTiO<sub>3</sub>/TiO<sub>2</sub> heterostructures were used for photocatalytic hydrogen generation from ethanol–water solutions at room temperature. NiTiO<sub>3</sub>/TiO<sub>2</sub> heterostructures provided unprecedented H<sub>2</sub> production rates up to 11.5 mmol h<sup>-1</sup> g<sup>-1</sup> and an AQY of 11.6%. This excellent performance was associated to the improvement of three parameters: surface area, light absorption and charge separation. We estimated a factor 3 increase of the surface area with the introduction of Ni through the formation of porous NiTiO<sub>3</sub>/TiO<sub>2</sub> heterostructures during the annealing in air.
- 3) The presence of NiTiO<sub>3</sub>, with lower band gap energy provided a higher light absorption coefficient at the excitation wavelength. Besides, TiO<sub>2</sub> and NiTiO<sub>3</sub> presented a proper band alignment that allows an efficient spatial charge separation of the photogenerated charge carriers before reaction, as confirmed by EIS analysis.
- 4) A simple method for the synthesis of CoTiO<sub>3</sub>/TiO<sub>2</sub> heterostructures with tuned CoTiO<sub>3</sub> amounts was presented. The materials showed an excellent activity in the photocatalytic hydrogen evolution from ethanol dehydrogenation, with the HER under UV light well above those of TiO<sub>2</sub>, CoTiO<sub>3</sub>, and Co-doped TiO<sub>2</sub>.
- 5) A significant influence of visible light on the HER of CoTiO<sub>3</sub>/TiO<sub>2</sub> heterostructures

was observed, well beyond the effect of temperature.

- 6) Electrochemical impedance spectroscopy and static and time-resolved PL measurements showed the formed heterostructures to promote charge separation, extending the lifetime of photogenerated charge carriers. UV-vis spectroscopy and UPS analysis showed the alignment of the energy levels of the two materials to resemble a type II heterostructure, with the CBM of CoTiO<sub>3</sub> below the H<sub>2</sub>/H<sup>+</sup> energy level. In such type II heterostructures, electron transfer from n-type TiO<sub>2</sub> to p-type CoTiO<sub>3</sub> is to be expected, generating an electric field within the material that drives photogenerated electrons within TiO<sub>2</sub> and photogenerated holes within CoTiO<sub>3</sub> away from the interphase and photogenerated holes in TiO<sub>2</sub> and electrons in CoTiO<sub>3</sub> toward the interphase where they recombine. All these evidences pointed out toward a direct Z-scheme mechanism as responsible of the enhanced photocatalytic ethanol dehydrogenation activity of CoTiO<sub>3</sub>/TiO<sub>2</sub> composites over that of TiO<sub>2</sub>.
- 7) A simple one-pot method for the synthesis of p-n Cu<sub>2</sub>O/TiO<sub>2</sub> heterostructures was presented. Using UV-vis spectroscopy and M-S analysis, we showed the formation of a p-n heterojunction between Cu<sub>2</sub>O and TiO<sub>2</sub>, which favors the separation of electron-hole pairs.
- 8) The obtained nanocomposites at 0.5%, 1%, 2%, and 5% Cu<sub>2</sub>O loading were tested for the photocatalytic dehydrogenation of ethanol in water:ethanol vapor mixture. We demonstrated the composites to be photostable catalysts capable of working in a light absorption towards the visible range, with an outstanding selectivity to the production of acetaldehyde and hydrogen from ethanol.
- 9) The optimum composition contained 1% of Cu<sub>2</sub>O and showed a yield for HER of 24.5 mmol g<sup>-1</sup> h<sup>-1</sup> and an AQY = 6.4%. The EIS analysis showed the 1% Cu<sub>2</sub>O/TiO<sub>2</sub> sample to be less resistive than TiO<sub>2</sub> sample and suggested that the heterojunction facilitated the charge transport and injection.
- 10) The addition of visible light increased the HER of the samples by a factor of two, which was partially associated with an increment in the reaction temperature of around 10 °C. We further discerned the influence of temperature and photogenerated electron-hole pairs in the HER increase upon visible light

irradiation, demonstrating the important role of photogenerated charge carriers in the presence of  $\text{Cu}_2\text{O}$ .

11) Our results open new opportunities for efficient solar energy conversion by the combination of energy sources in thermo-photocatalytic reactors.